Interpretation of x-ray absorption spectra using molecular dynamics simulations

Aleksandrs Kalinko
Institute of Solid State Physics
University of Latvia

Supervisor: Dr. phys. Aleksejs Kuzmins

A thesis submitted for the degree of
Doctor of Physics

October 2011

ESF
EIROPAS SOCIĀLAIS FONDS
EIROPAS SAVIENĪBA
LATVIJAS UNIVERSITĀTE
ANNO 1919
IEGULDĪJUMS TAVĀ NĀKOTNĒ

This work has been supported by the European Social Fund within the project Support for Doctoral Studies at University of Latvia

---

1. Reviewer:

2. Reviewer:

3. Reviewer:

Date of the defense: ______________________

Signature from the Head of PhD Committee: ___________________________________

To my parents

Acknowledgements

I am grateful to my supervisor Dr. Alexei Kuzmin who guided me during the whole period of my PhD studies and provided great atmosphere for our scientific research. I would like to thank Prof. Robert A. Evarestov for invaluable help in understanding the art of the quantum chemistry calculations. I would also thank Dr. Juris Purans for his helpful discussions and advices throughout the research.

I would also like to extend my thanks to Dr. Larisa Grigorjeva for providing all the facilities needed for the photoluminescence and infra-red spectra measurements.

I would to express gratitude to my parents for their encouragement and support over the many years of my studies.

Abstract

The x-ray absorption spectroscopy is a direct structure determination technique highly sensitive to the local structure. However, the nowadays extended x-ray absorption fine structure (EXAFS) spectra analysis meets complications due to the presence of multiple scattering effects and thermal disorder. In this work we have developed the method of the EXAFS spectra analysis based on the quantum mechanics-classical molecular dynamics approach coupled with ab-initio EXAFS spectra calculations. The method allows one to obtain unique information on the local atomic static and dynamic structure in crystalline materials, through the analysis of the many-atom distribution functions at required temperature and pressure. The method was applied to the modelling of the EXAFS spectra from crystalline ReO_3, $CaWO_4$ and $ZnWO_4$. The investigation of nanocrystalline $ZnWO_4$ is also reported.

Contents

List of Figures xv

List of Tables xxi

Glossary xxiii

1 Introduction 1

1.1 Motivation 1
1.2 Aim and objectives of the work 3
1.3 Scientific novelty of the work 4
1.4 Author's contribution 5
1.5 Contents of the thesis 5

2 X-ray absorption spectroscopy: State of the art 7

2.1 Basics of X-ray absorption 7
2.2 Theory of EXAFS modelling 12
  2.2.1 Gaussian model 12
    2.2.1.1 Cumulant model 13
    2.2.1.2 Arbitrary radial distribution function 13
  2.2.2 Advanced methods 14

3 EXAFS interpretation using molecular dynamics methods 17

3.1 General simulation scheme 17
3.2 Force-field model 21
3.3 Application of quantum mechanical methods for material properties calculations 23
3.4 Classical molecular dynamics simulations 27

3.5 Ab initio calculation of configuration averaged EXAFS 31

4 **Experimental** **33**

4.1 Sample preparation 33

4.1.1 Rhenium trioxide ReO_3 33

4.1.2 Calcium tungstate $CaWO_4$ 33

4.1.3 Zinc tungstate $ZnWO_4$ 33

4.2 X-ray powder diffraction 34

4.3 Infra-red spectroscopy 34

4.4 Raman spectroscopy 36

4.5 Photoluminescence spectroscopy 36

4.6 X-ray absorption spectroscopy 37

5 **Results** **41**

5.1 Local structure in $ZnWO_4$ nanoparticles 41

5.1.1 X-ray diffraction 41

5.1.2 Raman and optical spectroscopy 41

5.1.3 EXAFS spectroscopy 48

5.1.4 Conclusions 52

5.2 MD-EXAFS data analysis 53

5.2.1 Application to ReO_3 crystal 53

5.2.1.1 Ab initio LCAO modelling 55

5.2.1.2 Force-field model 59

5.2.1.3 MD-EXAFS modelling 59

5.2.1.4 Conclusions 62

5.2.2 Application to $CaWO_4$ crystal 63

5.2.2.1 Ab initio LCAO modelling 65

5.2.2.2 Force-field model 67

5.2.2.3 MD-EXAFS modelling 68

5.2.2.4 Conclusions 73

5.2.3 Application to $ZnWO_4$ crystal 73

5.2.3.1 Ab initio LCAO modelling 74

5.2.3.2 Force-field model 78

5.2.3.3 MD-EXAFS modelling 81

5.2.3.4 Conclusions 84

6 Conclusions **87**

Thesis **91**

References **93**

Author's publication list **105**

Participation in conferences **107**

Participation in schools with posters **109**

List of Figures

2.1 Photon cross-section components and total attenuation for tungsten atom. K, L and M are the absorption edges due to the electron transitions from the core levels. 8

2.2 (left panel) The experimental x-ray absorption spectrum (μ) of the W L_3-edge in $ZnWO_4$. μ_b is the background contribution, μ_0 is the atomic-like contrbution. (right panel) EXAFS oscillations $\chi(k)k^2$ extracted from the experimental absorption coefficient shown in left panel. 9

2.3 The mean free path $\lambda(E)$ of photoelectron depending on the energy for W L_3-edge including the core-hole effect. 12

3.1 The dependence of the number of scattering paths on the cluster size for ReO_3. 18

3.2 General MD-EXAFS simulation scheme. 19

3.3 Atomic displacements $\Delta\vec{u}$ for two atoms i and j, located at the average distance $|\vec{R}_{ij}|$. $|\vec{r}|$ is the instantaneous interatomic distance. Thermal ellipsoids are also shown for both atoms. 30

4.1 Schematic view of Bragg-Brentano powder diffractometer with a monochromator [2] 34

4.2 Schematic view of FTIR spectrometer 35

4.3 Schematic view of the scanning confocal microscope with spectrometer "Nanofinder-S" [1] 36

4.4 Schematic view of the photoluminescence experimental setup:
a. YAG:Nd solid state laser with 266 nm wavelength (4.66 eV) and 8 ns pulse length;
b. Feed and control module for laser;
c. Optical table;
d. Sample holder;
e. Vacuum system;
f. Carl Zeiss Jena SPM-1 prism monochromator;
g. Monochromator entrance and exit slits;
h. Quartz lenses;
i. Quartz window;
j. Adjustable mirror;
k. 266 nm interference filter;
l. Photomultiplier tube HAMAMATSU H8259;
m. Photomultiplier tube feeding module;
n. Pulse selector;
o. Ultrafast multiscaler P8777-1E photon counting board;
p. Control computer 38

4.5 Schematic view of the EXAFS experiment at C beamline DORIS III storage ring. The setup consists of the x-ray source (the storage ring), variable entrance and exit slits, double-crystal monochromator, three ionization chambers (I1, I2, and I3), beam stopper. The position of the unknown and reference samples and the optional fluorescence detector (not used in the present work) are also shown [3] 39

5.1 X-ray powder diffraction patterns of as-prepared (20°C) and annealed at 800°C $ZnWO_4$ powders. 42

5.2 Raman scattering spectra of $ZnWO_4$ powders annealed at different temperatures. Measurements were performed at 20°C. 42

5.3 (upper panel) Photoluminescence of $ZnWO_4$ powders annealed at different temperatures. The spectra intensities are normalized at the band maximum. (lower panel) Photoluminescence kinetics, measured at the intrinsic band maximum (∼2.5 eV), in $ZnWO_4$ powders annealed at different temperatures. Measurements were performed using pulsed YAG:Nd laser excitation (4.66 eV, 8 ns) at 20°C. 45
5.4 Photoluminescence band maximum position (top plot) and the bandwidth (bottom plot) in $ZnWO_4$ powders annealed at different temperatures. The point $T=$ 1000°C corresponds to the single crystal. The dashed lines are guides for eye. 46
5.5 The Zn K and W L_3 edges x-ray absorption spectra of nanoparticles (dashed line) and microcrystalline (solid line) $ZnWO_4$ measured at 10 K. The two edges are separated by ∼550 eV. 48
5.6 (a) Experimental W L_3-edge and Zn K-edge EXAFS spectra $\chi(k)k^2$ of nanoparticles and microcrystalline $ZnWO_4$. Only representative signals are shown for clarity. (b) Fourier transforms of the experimental W L_3-edge and Zn K-edge EXAFS spectra $\chi(k)k^2$ of nanoparticles and microcrystalline $ZnWO_4$. Both modulus and imaginary parts are shown. Only representative signals are shown for clarity. 50
5.7 (a) Best fits (solid lines) of the first coordination shell experimental (open circles) W L_3-edge and Zn K-edge EXAFS signals $\chi(k)k^2$ of nanoparticles and microcrystalline $ZnWO_4$ at different temperatures. (b) The reconstructed RDFs $G(R)$ for the first coordination shell of tungsten and zinc in nanoparticles and microcrystalline $ZnWO_4$ at representative temperatures. See text for details. 51
5.8 Crystal structure (left panel) and the first Brillouin zone (right panel) of ReO_3. $[ReO_6]$ octahedra are shown in the left panel. Blue spheres – rhenium atoms, red spheres – oxygen atoms. 54
5.9 X-ray powder diffraction pattern of ReO_3 powder. The *hkl* Miller indices are shown for the first seven Bragg peaks. 55
5.10 Phonon dispersion curves calculated by LCAO (upper panel) and force-field (lower panel) methods. 56

5.11 Calculated electronic band structure (left panel) and the projected density of electronic states (right panel) for ReO_3. 57

5.12 A comparison of experimental Raman spectrum for ReO_3 taken from [106] and calculated total phonon density of states. 58

5.13 (left panel) Representation of MD trajectories at 573 K for Re (black) and O (blue) atoms located in a plane $Z = a_0$ (a_0 is the lattice parameter). (right panel) Distribution of the Re–O–Re angles at 300 K, 423 K and 573 K, calculated from MD simulations. 60

5.14 Results of EXAFS modelling using MD-EXAFS method. (a) Re L_3-edge EXAFS signal in ReO_3, (b) FT of the Re L_3-edge EXAFS signal in ReO_3. 61

5.15 Results of the Re L_3-edge EXAFS modelling in ReO_3 using MD-EXAFS method within the SS and MS approximation: (left panel) EXAFS signals and (right panel) corresponding Fourier transforms. 62

5.16 Crystal structure (left panel) and the first Brillouin zone (right panel) of $CaWO_4$. [WO_4] tetrahedra and Ca atoms are shown in the left panel: red spheres – oxygen atoms, blue spheres – calcium atoms, gray spheres – tungsten atoms. 64

5.17 X-ray powder diffraction pattern of $CaWO_4$ powder. The *hkl* Miller indices are shown for the first five Bragg peaks. 64

5.18 Calculated band structure (left panel) and the density of electronic states (DOS) for $CaWO_4$ (right panel). 66

5.19 (left panel) Infra-red (IR) spectrum of $CaWO_4$ and calculated IR-active vibrational modes (blue vertical lines). The height of the lines indicates the calculated IR mode intensity. (right panel) Raman spectrum of $CaWO_4$ and calculated Raman-active vibrational modes (vertical lines). 67

5.20 Radial distribution functions (RDFs) W–O, W–Ca and W–W for $CaWO_4$ obtained from the MD simulations using the Senyshyn (left panel) [116] and Cooper (right panel) [21] force-field models. 70

5.21 Results of EXAFS modelling using MD-EXAFS method for Senyshyn (left column) and re-optimized Cooper (right column) force-field potential models. (a) W L_3-edge EXAFS signal in $CaWO_4$, (b) FT of the W L_3-edge EXAFS signal in $CaWO_4$. The configuration averaged EXAFS signals containing only SS (MD-FEFF SS) or all MS (MD-FEFF MS) contributions are shown. 71

5.22 The W L_3-edge EXAFS $\chi(k)k^2$ components for $CaWO_4$ in the single-scattering approximation and their Fourier transforms (FTs) corresponding to the atomic groups at different distances from the absorbing tungsten atom. 72

5.23 Crystal structure (left panel) and the first Brillouin zone (right panel) of $ZnWO_4$. $[WO_6]$ and $[ZnO_6]$ octahedra are shown in the left panel. Red spheres – zinc atoms, blue spheres – tungsten atoms, green spheres – oxygen atoms. 74

5.24 Calculated band structure (left panel) and projected density of electronic states (right panel) for $ZnWO_4$. 77

5.25 Comparison of XPS spectrum from [57] and projected DOS curves for wolframite-type $ZnWO_4$. Curves are vertically shifted for clarity. 77

5.26 Experimental infrared (left panel) and Raman (right panel) spectra in polycrystalline $ZnWO_4$. The positions of the LCAO calculated bands are shown by vertical lines. 78

5.27 Radial distribution functions (RDF) for W (a) and Zn (b) atoms obtained from the MD simulation results for Model1 – upper row, Model2 – middle row, Model3 – lower row. 82

5.28 Results of EXAFS modelling using MD-EXAFS method for three models of different complexity (Model1 - left column, Model2 - middle column, Model3 - right column). (a) W L_3-edge EXAFS signal in $ZnWO_4$, (b) FT of the W L_3-edge EXAFS signal in $ZnWO_4$, (c) Zn K-edge EXAFS signal in $ZnWO_4$, (d) FT of the Zn K-edge EXAFS signal in $ZnWO_4$. . 83

List of Tables

5.1 The parameters of the force-field model for cubic ReO_3. 59

5.2 Experimental and calculated structural properties of $CaWO_4$. 65

5.3 Parameters of the Senyshyn [116] and Cooper [21] force-field models for $CaWO_4$. The Cooper model has re-optimized W–O and Ca–O Buckingham pair potentials. 69

5.4 Experimental and calculated structural properties of $ZnWO_4$. 76

5.5 The parameters of the first (Model1) force-field model. 79

5.6 The parameters of the second (Model2) and third (Model3) force-field models. 80

Glossary

AO	Atomic orbital
BFT	Back-Fourier transformation
DCF	Displacement correlation function
DFT	Density functional theory
DOS	Density of states
DS	Double scattering
ECP	Effective core potential
EXAFS	Extended x-ray absorption fine structure
FF	Force-field
FT	Fourier transformation
FTIR	Fourier transform infra-red
FWHM	Full width half maximum
GGA	Generalized gradient approximation
HF	Hartree-Fock
KS	Kohn-Sham
LCAO	Linear combination of atomic orbitals
LDA	Local density approximation
LMTO	Linearized muffin-tin orbital
MC	Monte Carlo
MD	Molecular dynamics
MFP	Mean free path
MS	Multiple scattering
MSD	Mean square displacement

GLOSSARY

MSRD	Mean square relative displacement
ND	Neutron diffraction
PDF	Pair distribution function
PDOS	Partial density of states
PRDF	Partial radial distribution function
QM	Quantum mechanics
QMMD	Quantum mechanics-molecular dynamics
RDF	Radial distribution function
RMC	Reverse Monte Carlo
SCF	Self consistent field
SS	Single scattering
TS	Triple scattering
VAF	Velocity autocorrelation function
VDOS	Vibrational density of states
XANES	X-ray absorption near edge structure
XAS	X-ray absorption spectroscopy
XPS	X-ray photoemission spectroscopy
XRD	X-ray diffraction

1

Introduction

1.1 Motivation

The knowledge of the atomic structure is crucial to understand physical and chemical properties of any material. It provides a starting point for computer simulation studies in condensed matter physics, which play nowadays a fundamental role in many areas of investigation. Among different simulation techniques, quantum mechanical calculations, Monte Carlo and molecular dynamics simulations are today the most popular methods allowing one a detailed access to the static and dynamic properties of the material in a phase space [8].

While a number of experimental techniques probing structure related properties is rather large, there are only two *direct* structural tools, namely *x-ray (neutron/electron) diffraction* and *x-ray absorption spectroscopy*, which provide complementary information on the static and dynamic structure of a material.

In the diffraction experiment for polycrystalline solid, the Bragg reflections are measured, and then the atomic structure is solved using the Rietveld method [109]. The structure of polycrystalline solid is described by a symmetry group and a small number of structural parameters, known as the lattice parameters. Note that the diffraction experiments include also information on the thermal atomic motion allowing one to estimate the mean amplitude of atom vibrations, described by the *mean-square displacement* (MSD) parameter.

Since the Bragg peaks appear only in the case of periodic structures, another approach is used for the disordered solids, such as glasses and amorphous materials. In this case, the experimental scattering signal due to the elastic interaction between radiation and the solid includes only diffuse scattering. An intermediated situation can occur in nano-materials, where both diffuse and Bragg scattering can be present simultaneously. Therefore, the short and intermediate range order structure in such materials is determined from the analysis of the total scattering data using the Fourier transformation (FT) technique [101]. As a result, the atomic pair distribution function (PDF) is obtained, which shows the probability to find a pair of atoms separated by some distance. Opposite to diffraction, the contribution of the thermal atomic motion to PDF is described by the *mean-square relative displacement* (MSRD) parameter, which shows a variation of the interatomic distance.

The synchrotron-based x-ray absorption spectroscopy (XAS) is a powerful and versatile experimental technique to probe the local electronic and atomic structure of the materials [108]. The method is element specific, being well adapted for complex compounds, and is not limited by the state of the sample, so gases, liquids and solids can be studied equally well [33, 45]. Using focused x-rays, XAS allows one to study the local atomic structure around the absorbing atom at macro, micro- and nano-scale [45]. Time-resolved *in situ* XAS studies are also routinely possible in the range from minutes down to milliseconds, also under extreme conditions, such as high pressure and/or high temperature [18, 96]. X-ray absorption spectrum contains information on the many-atom distribution functions and, thus, is sensitive to the 3D structure of the material. However, due to a complexity of the problem, until now its practical application was mainly limited to the determination of near-neighbor distances, coordination numbers, static and thermal MSRDs, bonds anharmonicity, and ion oxidation states.

Some examples of XAS applications include the following. Being structurally local technique, the XAS is widely used for investigation of hydration structure of different ions in solutions [32]. The structural aspects of glasses are also studied by elucidating the structural role of the selected ions [71]. One can also probe the homogeneity of dopants in a glass and to check clustering effect depending on dopant concentration [7, 24]. Note that no other direct structural methods can provide such information. XAS is also suitable for the investigation of phase transitions induced by pressure or temperature [76, 132] and watching in-situ chemical reactions [44]. So, the application of XAS in different areas of physics and chemistry can be undoubtedly helpful to solve many practical tasks.

The experimental x-ray absorption spectra are conventionally divided into two parts: the x-ray absorption near edge structure (XANES), which is located up to about 50 eV above the Fermi level and includes electronic effects, and the extended x-ray absorption fine structure (EXAFS), which extends up to about 2000 eV above the Fermi level and includes local structural information around the absorbing atom. In this thesis only the EXAFS part is considered.

While general theory of the EXAFS has been developed in the past [108], the conventional analysis procedure of the EXAFS spectra is reliably defined only for the first coordination shell of the absorbing atom. It accounts only for the contributions from the pair atom distributions, known as the *single-scattering* (SS) effects. The same analysis of the further coordination shells is also possible, but only when the contribution from the many-atom distributions, known as the *multiple-scattering* (MS) effects, are negligible. While such requirement is strictly speaking never fulfilled, however the neglect of the MS contributions can be still a good approximation in some cases [107].

In general case, more advanced analysis of the full EXAFS spectrum, accounting for the multiple-scattering effects, should be used. Such computer codes are available today [34, 35, 108], however they are able to perform simulations either for a static atomic configuration or to account for the thermal atomic motion through simple analytical approximations such as the Einstein or Debye models. One should point out that thermal disorder significantly affects the EXAFS spectrum, being usually responsible for up to 20-80% of the total amplitude. Therefore, the accurate accounting of the thermal atomic motion in the EXAFS spectra is crucial for the analysis but still remains an unresolved issue.

The possible solution of this problem is to use the molecular dynamics (MD) or Monte Carlo (MC) simulations in a combination with ab initio EXAFS calculations. Both methods allow starting from an interaction potential model to obtain a set of atomic configurations, which can be used further to calculate the configuration-averaged EXAFS signal at required experimental conditions (temperature, pressure).

1.2 Aim and objectives of the work

The research activities underlying the thesis include both experimental (sample synthesis and studies by several experimental method including experiments at synchrotron facility) and theoretical (software development and computer simulations) work.

The main goal of the present work is to further develop the method for the EXAFS spectra modelling based on the quantum mechanics-classical molecular dynamics (QMMD) approach coupled with ab initio EXAFS spectra calculations. The method allows one to obtain unique information on the local atomic static and dynamic structure in crystalline materials, through the analysis of the many-atom distribution functions at required temperature and pressure.

The advantage of the method is its ability to accurately account for thermal disorder within the multiple scattering (many-atom) effects that allows one to perform direct simulation of the total EXAFS signal. Note that the use of classical molecular dynamics limits our analysis to the high-temperature region, however such limitation is not inherent for the method itself and can be overcome by using the quantum MD.

The objectives of the present work are to demonstrate

- the potentiality of the method for the analysis of experimental EXAFS spectra on an example of crystalline systems with the different local coordinations. The three studied compounds ReO_3, $CaWO_4$ and $ZnWO_4$ cover different types of $5d$-element (W, Re) local coordination, starting from regular tetrahedral in tetragonal $CaWO_4$ to distorted octahedral in monoclinic $ZnWO_4$, and, finally, regular octahedral in cubic perovskite-type ReO_3.
- the ability of the EXAFS technique to deal with highly distorted local atomic structure on an example of nano-crystalline $ZnWO_4$, having large surface to bulk ratio.

1.3 Scientific novelty of the work

The study of the local atomic structure (up to ~6 Å around the absorbing atom) in ReO_3, $CaWO_4$ and $ZnWO_4$ crystals has been performed by x-ray absorption spectroscopy (EXAFS) simultaneously taking into account thermal disorder and multiple-scattering (many-atom) effects within the QMMD-EXAFS approach.

Significant deformation of the local atomic structure around W and Zn atoms in nano-crystalline $ZnWO_4$ has been determined by the EXAFS technique in comparison with the micro-crystalline zinc tungstate. The complementary studies by EXAFS and

Raman spectroscopy allowed us to conclude that the [WO_6] octahedra deformation in nano-crystalline $ZnWO_4$ results in the formation of short double tungsten-oxygen bonds.

1.4 Author's contribution

The major part of the work has been done at the Institute of Solid State Physics, University of Latvia. The XAS measurements were performed at HASYLAB (Hamburg, Germany) using synchrotron radiation produced by the DORIS III storage ring. The author has been participating in the nano-samples synthesis, their characterization by the IR and Raman spectroscopy, temperature dependent EXAFS measurements of nano and microcrystalline $ZnWO_4$ and $CaWO_4$. The quantum mechanical calculations, analysis of the experimental EXAFS data and the advanced modelling of EXAFS spectra have been performed by the author at the Latvian SuperCluster facility [75]. The computer code for the force-field potential parameters optimization has been also developed by the author based on the simulated annealing method.

The results of this work have been presented at 9 international conferences and 4 international schools during 2008-2011 and discussed at the scientific seminar at the Institute of Solid State Physics, University of Latvia on May 09, 2011. Main results have been published in 7 SCI papers.

1.5 Contents of the thesis

The thesis is comprised of the four chapters.

In Chapter 2 a review of the x-ray absorption spectroscopy technique is given. The basic theoretical description of EXAFS phenomena is provided. The conventional EXAFS spectra analysis for the first coordination shell is shown, and possible advanced analysis methods are discussed.

Chapter 3 is devoted to the description of the advanced EXAFS spectra modelling scheme using quantum mechanical-molecular dynamics simulations in a combination with ab initio EXAFS calculations. The modelling algorithm is discussed, and its each step is described in details including a derivation of the force-field model using the experimental data and the results of the quantum mechanical calculations as well as classical molecular dynamics method.

In Chapter 4 the samples used in the experiments and the experimental methods employed in this work are described.

Chapter 5 presents experimental and modelling results. It consists of the two parts. The first part is devoted to the conventional EXAFS data analysis of the first coordination shell in $ZnWO_4$ nano-particles. The second part contains main results of the present work on the MD-EXAFS modelling for ReO_3, $CaWO_4$ and $ZnWO_4$ crystals.

Finally, the main conclusions and suggestions for the future studies are given in Chapter 5.

2

X-ray absorption spectroscopy: State of the art

2.1 Basics of X-ray absorption

The x-ray interaction with matter occurs elastically (coherent), when the kinetic energy of the incident photon is conserved, and inelastically (incoherent), when the kinetic energy of the incident photon is not conserved. In an inelastic scattering process, some of the energy of the incident photon is lost or gained. There are three types of the inelastic x-ray interactions with matter: the photoexcitation of electrons, the Compton effect and the electron-positron pair production.

In Fig. 2.1 photon cross-section dependance on the excitation energy for W atom is shown. In the hard x-ray range (~10 keV) photoexcitation process dominates, therefore the assumption that x-ray absorption coefficient is proportional to the photoexcitation transition rate can be made.

In x-ray absorption spectroscopy experiments, the absorption of x-rays by the sample with thickness (d) is measured as a function of x-ray energy. The x-ray absorption coefficient $\mu(E)$ is determined by measuring the incident (I_0) and transmitted (I) x-ray beams intensities as

$$\mu(E) = \frac{1}{d} \ln(\frac{I_0}{I}). \tag{2.1}$$

The energy dependence of the x-ray absorption coefficient (Fig. 2.2) shows three main features: when photon energy increases, the absorption coefficient decreases before an absorption edge, at certain energy the sharp change of the absorption coefficient

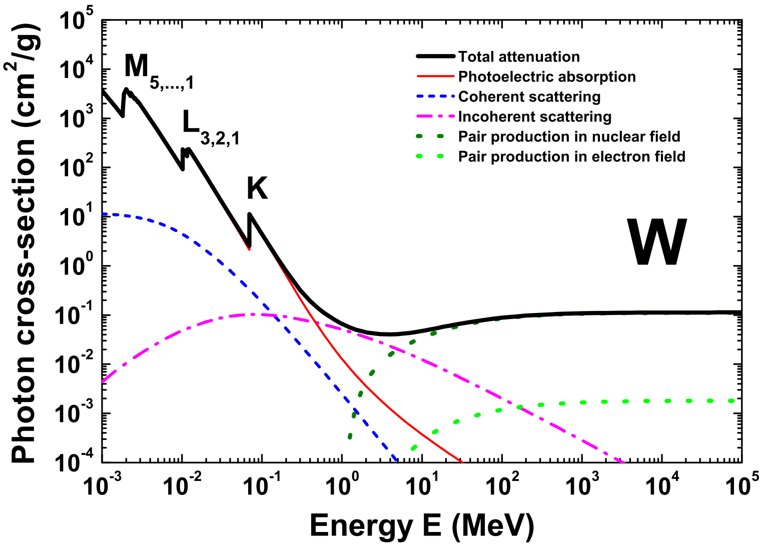

Figure 2.1: Photon cross-section components and total attenuation for tungsten atom. K, L and M are the absorption edges due to the electron transitions from the core levels.

occurs and is called the edge, and, finally, the oscillating variation of the absorption coefficient occurs above the edge. These oscillations are called the extended x-ray absorption fine structure (EXAFS). The EXAFS signal $\chi(E)$ is defined as the normalized, oscillatory part of the x-ray absorption coefficient (μ) above a given absorption edge

$$\chi(E) = \frac{\mu(E) - \mu_0(E) - \mu_b(E)}{\mu_0(E)} \tag{2.2}$$

where $\mu_b(E)$ is the background absorption coming from electrons of the outer shells, and $\mu_0(E)$ is the atomic-like contribution. The fine structure, i.e. EXAFS, arises due to the scattering of the excited photoelectron by a potential from all neighbouring atoms surrounding the absorbing atom. The photoelectron is excited into empty states above the Fermi level, and its lifetime is limited by the lifetime of the core-hole and by an interaction with other electrons. The photoelectron lifetime restricts its mean free path and, thus, is responsible for the local sensitivity of the method. Therefore, the EXAFS signal probes the local structural and electronic information around the absorber.

Quantum mechanical description of the photoexcitation transition rate is given by the Fermi's Golden Rule, which in the one-electron and dipole approximations is given as

$$\mu \propto \sum_f |\langle \psi_f | \vec{p} \cdot \vec{A}(r) | \psi_i \rangle|^2 \delta(E_f - E_i - \hbar\omega) \tag{2.3}$$

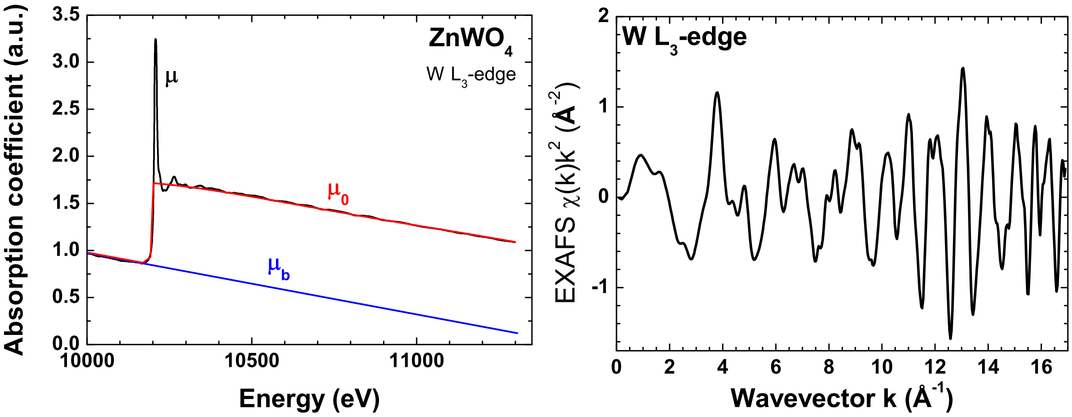

Figure 2.2: (left panel) The experimental x-ray absorption spectrum (μ) of the W L$_3$-edge in ZnWO$_4$. μ_b is the background contribution, μ_0 is the atomic-like contrbution. (right panel) EXAFS oscillations $\chi(k)k^2$ extracted from the experimental absorption coefficient shown in left panel.

where ψ_i is the initial state wave function, ψ_f is the final state wave function, $E_f = E_i + \hbar\omega$ is the energy conservation condition, $\vec{p} \cdot \vec{A}(r)$ is the x-ray absorption transition operator. The quantity $\vec{p}$ is the momentum operator, and $\vec{A}(r)$ is the vector potential of the incident electromagnetic field. The initial state wave function ψ_i is strongly localized at the absorbing atom. That is why photoabsorption process probes the value of the final state wave function also at the absorbing atom.

To solve this equation, the multiple-scattering (MS) theory [108] was developed in the past. Eq. 2.3 can be rewritten using the Green functions formalism as

$$\mu \propto \frac{1}{\pi} Im\langle\psi_i|\vec{p} \cdot \vec{A}(r')G(r, r', E)\vec{p} \cdot \vec{A}(r)|\psi_i\rangle\theta(E - E_F) \tag{2.4}$$

where $G(r, r', E)$ is the full one electron propagator, describing the propagation of the excited photoelectron from point r to point r', and $\theta(E - E_F)$ is a broadened step function at the Fermi energy E_F. The Green function can be determined from the solution of an effective one-particle Schrödinger equation, known as the Dyson equation

$$(\nabla^2 + E - U_c(\vec{r}) - \Sigma_{XC}(E; \rho(\vec{r})))G(\vec{r}, \vec{r}', E) = \delta(\vec{r} - \vec{r}') \tag{2.5}$$

where $U_c(\vec{r})$ is the final state Coulomb potential, $\Sigma_{XC}(E; \rho(\vec{r}))$ is local energy-dependent exchange potential.

The full Green function $G(r, r', E)$ of an excited photoelectron with the energy E can be separated into a sum of $G^C(\vec{r}, \vec{r}', E)$ and $G^{SC}(\vec{r}, \vec{r}', E)$, where $G^C(\vec{r}, \vec{r}', E)$ describes the atomic-like absorption at the absorbing atom, and $G^{SC}(\vec{r},\vec{r}',E)$ is the multiple-scattering contribution, which describes all possible ways that the photoelectron can scatter from one or more of the surrounding atoms before the core-hole is re-filled

$$G^{C} = G^0 + G^0 t_c G^0, \tag{2.6}$$

$$G^{SC} = G^0 t G^0 + G^0 t G^0 t G^0 + G^0 t G^0 t G^0 t G^0 + \ldots . \tag{2.7}$$

Here G^0 is the free particle Green function, which describes how the photoelectron propagates between two points in space, t is the scattering matrix describing how the photoelectron scatters from a single atom. G^0 function has the spherical wave form

$$G^0(\vec{r},\vec{r}',E) = -\frac{1}{4\pi}\frac{e^{ik|\vec{r}-\vec{r}'|}}{|\vec{r}-\vec{r}'|}. \tag{2.8}$$

where k is the photoelectron wave number ($k = \sqrt{(2m_e/\hbar^2)(E-E_F)}$, m_e is the electron mass, $\hbar$ is the Plank's constant).

Each term of Eq. 2.7 describes an order of scattering. The first term describes all ways how photoelectron can be scattered by only one neighbouring atom, and it corresponds to the single scattering (SS) processes. The second term describes all ways how photoelectron can scatter by exactly two atoms, and it corresponds to the double scattering (DS) processes. The next term describes the triple scattering (TS) processes, where the photoelectron is scattered by three atoms, and so on. The series, given by Eq. 2.7, is called the multiple-scattering series and, while it is infinite, on practice, one limits it at some high-order scattering process.

Further, each term in Eq. 2.7 can be written as a sum over every path of the respective order

$$G^{SC} = \sum_{i\neq 0} G_c t_i G_c + \sum_{i,j\neq 0; i\neq j} G_c t_i G^0_{i,j} t_j G_c + \ldots, \tag{2.9}$$

where G_c is the propagator between the absorbing and some neighbouring atom, and $G^0_{i,j}$ is the propagator between atoms i and j.

The expansion (Eq. 2.7) into scattering paths is used for the EXAFS calculation and is implemented in the FEFF [9] code. Another known approach to take into account the MS effects is based on the n-body decomposition of the cross section [35]. In this approach, the overall cross section is defined as a sum of the n-atom cross sections

$$\mu = \mu(0) + \mu(0,i) + \mu(0,i,j) + \mu(0,i,j,k) + \ldots, \tag{2.10}$$

where $\mu(0)$ is the atomic cross section, $\mu(0, i)$ is the cross section for the group of two atoms 0 and i only, $\mu(0, i, j)$ is the cross section for the group including atoms 0, i and j.

One should point out that the high-order scattering terms in Eq. 2.7 or 2.10 represent the contributions from many-atom distribution functions of the respective order. This fact significantly complicates the EXAFS data analysis, but allows one to determine unique information on the high-order atomic correlation functions, which is not accessible by diffraction methods.

In the simplest case, if one considers only the scattering by the nearest atoms located in the first coordination shell of the absorber, the interpretation of the EXAFS signal can be done in the single-scattering approximation and, thus, becomes rather simple. As a result, it provides with the structural information on the number of neighbours, interatomic distances to neihbouring atoms, and thermal or static disorder factors.

Conventional EXAFS data analysis is based on the separation of the EXAFS signals for different coordination shells and their independent analysis. The Fourier transform (FT) and back-Fourier transform (BFT) are used for this operation. The FT converts EXAFS signal from k-space to R-space, where one can see the regions, which correspond to the different coordination shells. Next, one chooses the region corresponding to the single coordination shell in R-space and, by performing BFT, obtains the isolated EXAFS signal in k-space. This signal is further used for the modelling. The most common technique is a parametrization of the signal within the so-called Gaussian or cumulant model [37]. Another possibility is to reconstruct the radial distribution function (RDF) using, for example, regularization technique [78]. In most cases, the accurate analysis can be performed only for the region of the first coordination shell of the absorber, where the multiple-scattering effects do not exist. In some special cases, when the multiple-scattering contributions into the EXAFS signal can be neglected, it is also possible to extend the analysis to the further (outer) coordination shells.

In the next sections, several parameterizations of the EXAFS equation will be given for some common cases and discussed in details.

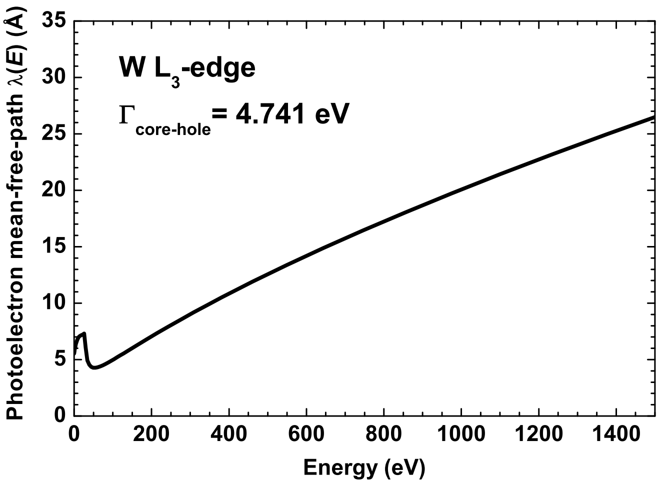

Figure 2.3: The mean free path $\lambda(E)$ of photoelectron depending on the energy for W L$_3$-edge including the core-hole effect.

2.2 Theory of EXAFS modelling

2.2.1 Gaussian model

In the single-scattering spherical wave and harmonic approximations, the conventional EXAFS equation for the absorbing atom with N neighbouring atoms can be written as [33]

$$\begin{aligned}\chi(k) \quad &= \quad S_0^2 \sum_j \frac{N_j f_j(k,R_j) e^{-2k^2\sigma_j^2}}{kR_j^2} e^{-2R_j/\lambda(k)} \\ &\quad \times \sin[2kR_j + \delta_j(k,R_j) + 2\delta_l(k) - l\pi] \qquad (2.11)\end{aligned}$$

where S_0^2 is the scale factor taking into account amplitude damping effect due to the multielectron effects, $f_j(k,R_j)$ is backscattering amplitude and $\delta_j(k,R_j)$ is the phase-shift of backscattered wave with contribution from the absorber $2\delta_l(k)$ and the backscatterer, l is the angular momentum of the photoelectron (l=1 for K and L$_1$ edges, l=2 for L$_2$-edge, l=0 for L$_3$-edge), N_j is coordination number of the j-th shell, R_j is the radius of the j-th shell, σ_j is mean square radial displacement (MSRD) or EXAFS Debye-Waller factor, $\lambda(k)$ is the mean free path of the photoelectron.

In Fig. 2.3 the mean free path of the photoelectron is shown for W L$_3$-edge, including the core-hole effect.

There are two possibilities how to obtain scattering amplitudes and phases. The first one is to perform theoretical calculation, e.g. using the FEFF code [9], whereas another way is to extract them from experimental spectrum of the reference compound.

2.2.1.1 Cumulant model

The formula 2.11 doesn't take into account any anharmonic effect. To deal with this effects additional parameters - cumulant expansion were introduced [14, 37] and conventional EXAFS formula can be rewritten

$$\begin{aligned}\chi_{model}(k) &= \sum_{j}^{shells} \frac{N_j f_j(k) e^{-2k^2\sigma_j^2+\frac{2}{3}C_{4j}k^4-\frac{4}{45}C_{6j}k^6}}{kR_j^2} e^{-2R_i/\lambda(k)} \\ &\quad \times \sin[2kR_j - \frac{4}{3}C_{3j}k^3 - \frac{4}{15}C_{5j}k^5 + \delta_j(k,R_j) + 2\delta_l(k) - l\pi] \end{aligned} \tag{2.12}$$

where C_{3i}, C_{4i}, C_{5i} and C_{6i} are cumulants of the distribution taking into account anharmonic effects and/or non-Gaussian disorder.

2.2.1.2 Arbitrary radial distribution function

In some cases previously described parametrization of the EXAFS signal does not give good results. This is, for example, the case of highly locally disordered material, where even the first coordination shell can have very large distortion. Examples of such materials are amorphous compounds, glasses, low-symmetry systems, nanomaterials with strong relaxation. In this cae, the use of the parameter free model helps to solve the structure using the experimental EXAFS signal. The method is based on the calculation of the EXAFS signal from the radial distribution function (RDF). The single shell EXAFS for the arbitrary RDF $G(R)$ within spherical wave approximation is given by

$$\chi(k, G(R)) = \int_{R_{\min}}^{R_{\max}} \frac{G(R)}{kR^2} f(k,R) \sin[2kR + \delta_j(k,R_j) + 2\delta_l(k) - l\pi] dR \tag{2.13}$$

where $[R_{min};R_{max}]$ is the interval of the RDF $G(R)$.

So, the task becomes to find such RDF, which gives the best match to the experimental EXAFS signal and, at the same time, is a smooth positive function. The limitation of this method is only the first coordination shell analysis with only one type of atoms in the shell. This method will be used further for interpretation of the EXAFS spectra for $ZnWO_4$ nanoparticles.

2.2.2 Advanced methods

Previously described methods are valid for the first coordination shell and the outer coordination shells, when they do not overlap with the multiple-scattering contributions. However, in most practical cases the multiple-scattering effects give strong influence on the EXAFS signal after the first coordination shell. Another important point is to account for static and thermal disorder in a material. Even in the case of crystalline material, where atomic positions are strictly defined, the conventional analysis of the full EXAFS spectrum including thermal disorder is complicated and often impossible. This is due to a number of fitting parameters required to describe correlated motion of atoms for each scattering paths. For highly disordered materials as glasses or liquids, the problem becomes even more complicated.

To overcome these problems, the advanced technique exists which combines molecular dynamics or Monte-Carlo simulations with either conventional EXAFS spectra analysis or ab initio EXAFS spectra calculations.

In the literature many different combinations of advanced EXAFS spectra analysis can be found. The big part of the works is dedicated to the analysis of the local structure in glasses [15, 64, 92, 111, 129, 130]. Another part of works considers local structure of metal ions in solutions [59, 87, 118, 119] or liquid materials [86, 97, 131]. In recent years, works dedicated to the local structure investigation by EXAFS and MD in monoatomic and more complex solids become popular [11, 20, 72, 73, 74, 83, 88, 97, 110, 112, 120].

The analysis scheme is based on molecular dynamics or reverse Monte-Carlo simulations. As a result, the set of static atomic configurations is obtained. The difference between two types of simulations is that MD gives system development in time. This means that the next configuration is dependent on the previous. In contrast, no time evolution of the system is present in the RMC simulations. In the RMC calculations there is no need for potential model, and it can be considered as an advantage. Further, the set of atomic configurations is used to compute radial distribution functions (RDF). The theoretically obtained RDF can be compared with the RDF reconstructed from experimental EXAFS signal using Eq. 2.13. Another possibility is to construct the EXAFS signal from calculated RDF and next to compare it with the experimental EXAFS signal. Both approaches were used for highly distorted materials analysis.

Another usage of the MD atomic configurations is to calculate configuration averaged EXAFS using ab initio code like FEFF [9] or GNXAS [34, 35]. Thus obtained theoretical spectrum can be directly compared with the experimental one. Such comparison gives clear idea whether the potential model used in the MD calculation is good or not. Such approach can be applied to any material either highly distorted or highly symmetrical. The combination of the molecular dynamics simulations with ab initio EXAFS spectra calculations is discussed in details further in this work with analysis examples.

3

EXAFS interpretation using molecular dynamics methods

3.1 General simulation scheme

In this section the calculations of the EXAFS spectra based on the results of the molecular dynamics simulations will be discussed in details.

The today difficulties of the EXAFS analysis are mainly connected to the two problems. The first one is an account for the photoelectron multiple-scattering (MS) effects, which contribute into the EXAFS spectra analysis beyond the first coordination shell in R-space. The second problem is related to an account for thermal and static disorder, especially, within the MS contribution.

One should note that when the size of the system grows up, the use of simple Gaussian/cumulant models becomes unpractical, due to a huge number of fitting parameters is required. Considering all MS contributions independently, each scattering path is described by at least three parameters, i.e. path degeneracy, length and MSRD. Therefore, an increase of the EXAFS spectrum analysis interval in R-space leads to the exponential growth of the number of scattering paths as well as of the fitting parameters. At the same time, the maximum number of fitting parameters is limited, according to the Nyquist theorem

$$N_{exp} = \frac{2\Delta k \Delta R}{\pi} + 2, \tag{3.1}$$

by the number of independent points (N_{exp}) in the experimental signal.

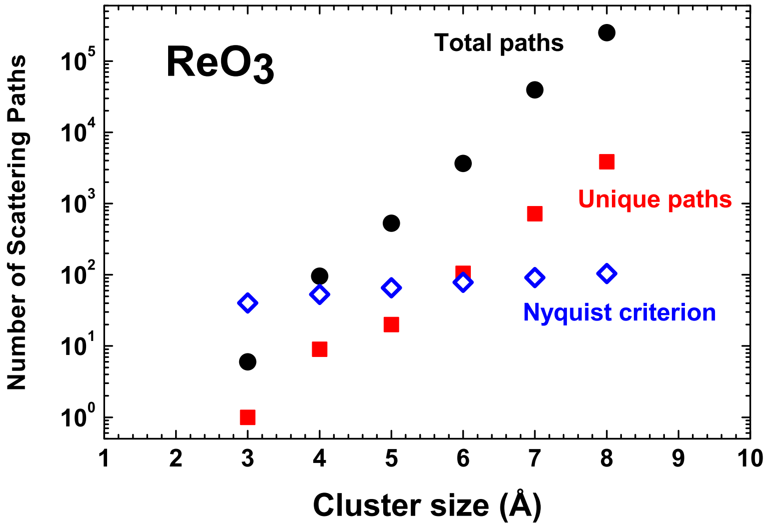

Figure 3.1: The dependence of the number of scattering paths on the cluster size for ReO_3.

The dependence of the number of scattering paths on the cluster size is shown in Fig. 3.1 for ReO_3 as an example. Here the circles and squares represent the total number and the unique number of scattering paths, respectively. The number of the unique paths is much smaller than their total number due to the crystal symmetry. However, the crystal symmetry becomes broken when thermal or static disorder is introduced, i.e. when atoms are randomly displaced from their equilibrium positions. In this case, all scattering paths must be considered. The diamonds in Fig. 3.1 indicate the number of independent experimental data points according to the Nyquist theorem. Δk was chosen equal to 20 Å^{-1}, that corresponds to the high-quality data obtained at modern experimental setups. According to the results reported in Fig. 3.1, the analysis of the EXAFS signal in ReO_3 becomes impractical beyond 6 Å even when some analytical model for the thermal vibrations, which reduces the total number of fitting parameters, is used. In many closed packed structure with low crystal symmetry this range will be much smaller.

Another problem related to the thermal disorder is its impact on the EXAFS signal amplitude through the variation of the path geometry. This influence is twofold. First, the thermal vibrations will lead to the EXAFS signal damping at high k-values. Second, they will modify the scattering path geometry and, thus, directly influence the scattering amplitude and phase of the multiple-scattering signals. Note that even if the

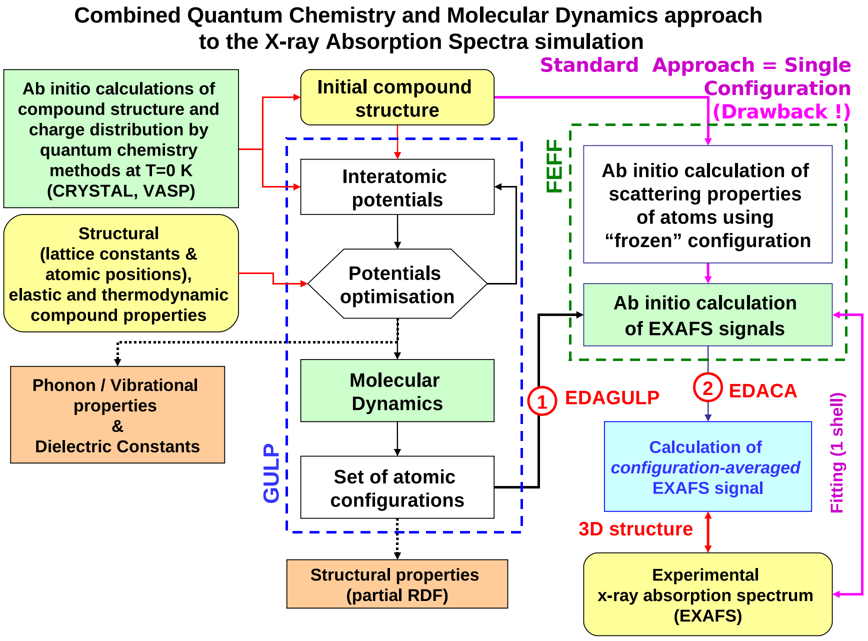
Combined Quantum Chemistry and Molecular Dynamics approach
to the X-ray Absorption Spectra simulation
Standard Approach = Single Configuration (Drawback !)
Ab initio calculations of compound structure and charge distribution by quantum chemistry methods at T=0 K (CRYSTAL, VASP)
Initial compound structure
Interatomic potentials
Potentials optimisation
Structural (lattice constants & atomic positions), elastic and thermodynamic compound properties
Phonon / Vibrational properties & Dielectric Constants
Molecular Dynamics
Set of atomic configurations
GULP
Structural properties (partial RDF)
FEFF
Ab initio calculation of scattering properties of atoms using "frozen" configuration
Ab initio calculation of EXAFS signals
1 EDAGULP
2 EDACA
Calculation of configuration-averaged EXAFS signal
Fitting (1 shell)
3D structure
Experimental x-ray absorption spectrum (EXAFS)

Figure 3.2: General MD-EXAFS simulation scheme.

thermal displacements of atoms are rather small, the non-linear angular dependence of the multiple-scattering signals can result in an appreciable change of the EXAFS signal [77].

To overcome the above mentioned problems, the following approach can be adapted. The time-dependent dynamics of the system can be approximated by a set of atomic configurations (snapshots), taken at short periods of time. The sampling time is strictly connected to the highest characteristic frequency of the compound and is usually located in the femtoseconds range (0.5 fs in the present work). Since each snapshot represents the static atomic configuration, its EXAFS signal can be easily calculated including rigorously all multiple-scattering contributions. Next, the configuration-averaged EXAFS signal is determined by averaging over all snapshots, thus accounting for the dynamic disorder.

For practical realization of the method, a combination of molecular dynamics simulation and ab initio EXAFS calculations can be used. Molecular dynamics simulation produces a set of atomic configurations at required temperature and pressure, thus introducing the disorder. The ab initio EXAFS calculations allow one to accurately evaluate the EXAFS signal for static configuration, thus accounting for the multiple-scattering effects.

In the Fig. 3.2 the general MD-EXAFS simulation scheme [73, 74] is shown. It combines three calculation methods, quantum chemistry, classical molecular dynamics (MD) and ab initio EXAFS calculations.

One should point out that a number of important approximations are employed when doing the MD simulations. First, the use of the Born-Oppenheimer or adiabatic approximation allows one to separate treatment of electrons and nuclei. As a result, for each set of nuclear positions, one can get the energy contributed by the electrons. This energy together with the nuclear-nuclear repulsions determines the total potential energy and can be used to find the forces acting on the atoms. One can introduce the potential energy surface by requiring that the total potential energy is a function of atomic positions only, thus eliminating the electrons from the consideration. Next, the nuclei are treated as classical particles moving on the potential energy surface, thus replacing the Schrödinger's equation with the Newton's one. Finally, the potential energy surface is approximated by an analytical function (force-field) that gives the potential energy and interatomic forces as a function of atoms coordinates.

The starting point of the analysis is the compound structure, which can be determined for crystalline compounds from diffraction experiments. The structural information and other physical properties give an idea for choosing the type of the force-field model, i.e. the interaction potentials between atoms. Once interatomic potentials are defined, the optimization procedure can be performed to obtain potential parameters, which reproduce best structure and given properties. Further, the MD simulations are performed using the obtained force-field model to get a set of atomic configurations.

The results of the MD simulations allow one to make some conclusions about correctness of interatomic potentials. The total and partial RDF functions can be calculated and compared with the first coordination shell RDFs obtained from the conventional EXAFS data analysis. Additionally the average atomic positions can be compared with initial structure to check whether there is strong atoms displacements or not. The strong displacements of atoms from the equilibrium positions indicate the problem with the FF model.

After performing the MD simulations, every single atomic configuration is used to calculate the EXAFS signal. Finally, the configuration averaged EXAFS signal is calculated and directly compared with the experimentally measured EXAFS spectrum.

At the potential parameters optimization step, the experimentally measured properties can be complemented with that calculated by quantum chemistry methods. The best example is the phonon dispersion relations through the first Brillouin zone. For the most materials, it is relatively easy to measure vibrational frequencies at the Γ point of the Brillouin zone using Raman and/or infra-red spectroscopy. However, the measurement of the phonon dispersion relations is a complicated experimental task, which can be performed only at large scale facilities exploiting neutrons or x-ray synchrotron radiation and requires the availability of monocrystalline sample [39]. At the same time, the knowledge of phonon dispersion relations helps to make the force-field optimization procedure more reliable and stabilizes the solution.

In the next sections the force-field model development, molecular dynamics simulations and quantum chemistry calculations will be discussed in details.

3.2 Force-field model

Before the MD simulations can be performed, the force-field model must be developed. The total potential energy for a system is equal to the sum over all interactions

$$E = \sum_i U_i(\vec{r}_i) + \frac{1}{2!}\sum_{i<j} U_{ij}(\vec{r}_i, \vec{r}_j) + \frac{1}{3!}\sum_{i<j<k} U_{ijk}(\vec{r}_i, \vec{r}_j, \vec{r}_k) + ... \tag{3.2}$$

It consists from self energy terms $U_i(\vec{r}_i)$ which describe hybridization and ion compression. Pair potential terms $U_{ij}(\vec{r}_i, \vec{r}_j)$ describe interactions between two atoms like Pauli repulsion, Coulomb and Van der Walls forces. Three body terms $U_{ijk}(\vec{r}_i, \vec{r}_j, \vec{r}_k)$ are responsible for the angle-dependent forces. The next many-body terms can be used to describe torsional effects, metallic cohesion, directional (covalent) bonding, but often are neglected in the expansion.

In this work only pair and three body potentials were used to construct the force-field model. In the crystal modelling the main contribution to the potential energy comes from the Coulomb interaction

$$U_{ij}^{Coulomb}(r_{ij}) = \frac{Z_i Z_j e^2}{r_{ij}}. \tag{3.3}$$

Therefore, the choice of the ions charge Z_i is very important. One possibility is to take ions charges equivalent to the chemical valence state. Another choice is to take them equal to the Mulliken charges, obtained from the quantum chemistry calculations [74]. It is also possible to fit the charge to improve the accuracy of the force-field model. However, the drawback of the charge fitting is the transferability of the potential.

Developed FF model allows one to perform structure optimization, after that a wide range of physical properties can be evaluated. The main properties considered in this work are the elastic constants, the vibrational frequencies and the phonon dispersion curves.

The elastic constants C_{ij} are calculated as the second derivatives of the energy density with respect to the strain

$$C_{ij} = \frac{1}{V}\left(\frac{\partial^2 E}{\partial u_i \partial u_j}\right) \tag{3.4}$$

where u_i is a displacement of an atom along ith cartesian coordinate from equilibrium position. The details of the vibrational frequencies and the phonon dispersion curves evaluation will be discussed below in Section 3.3.

In the present work we are using two- and three-body terms with defined functional forms. Higher order interactions weren't used in this work. The two-body terms were chosen in the Buckingham (Eq. 3.5), Morse (Eq. 3.6) and covalent exponential (Eq. 3.7) forms

$$U_{ij}^{Buck}(r_{ij}) = Ae^{-\frac{r_{ij}}{\rho}} - \frac{C}{r_{ij}^6}, \tag{3.5}$$

$$U_{ij}^{Morse}(r_{ij}) = D_e(1 - e^{-a(r_{ij}-r_0)})^2 - D, \tag{3.6}$$

$$U_{ij}^{CovExp}(r_{ij}) = -De^{\frac{-n(r_{ij}-r_0)^2}{2r_{ij}}}. \tag{3.7}$$

Here the values A, ρ, C, D_e, a, D, n and r_0 are the parameters of the potentials.

The three body interaction was described within the harmonic form

$$U_{ijk}^{Three}(\theta_{ijk}) = \frac{1}{2}k_{three}(\theta_{ijk} - \theta_0)^2 \tag{3.8}$$

and allows one to set an equilibrium angle θ_0 between two bonds. Here k_{three} is the force constant.

The construction of the force-field model is crucial for the further modelling. Possibly it should describe all interactions between atoms present in the system. However, not all effects can be accounted for within such simple model. For example, an account of electronic effects is strongly limited and can be included only indirectly, thus, complicating the model.

After the force-field model construction, the potential parameters should be determined. The important task is to choose charge of the ions. Since it cannot be directly measured experimentally, there is possibility to take either formal charges according to the chemical formula or the ones calculated by quantum chemistry methods. Sometimes atomic charge can be one of the variable parameters, but in most cases they are fixed. Other potential parameters are fitted to give the best matching between calculated and experimental properties. In this work, the GULP3.1 code [41] was used for this purpose. Besides, the simulated annealing algorithm was also implemented for potential parameters fitting allowing one to fit also the atomic charges (the option being not available in the GULP3.1 code [41]).

3.3 Application of quantum mechanical methods for material properties calculations

Quantum mechanics (QM) allows one to describe electronic and atomic structure, chemical bonding and different physical properties of a materia. The theoretical description of material helps to verify experimentally measured properties. Besides, some properties can't be measured or difficult to obtain experimentally, but can be evaluated theoretically. Thus, the QM calculations complement information about material under investigation. In this work we have used both experimental and theoretically calculated properties for the potential parameters determination.

The time independent Schrödinger equation

$$\hat{H}\Phi = E\Phi. \tag{3.9}$$

is used in QM to find eigenfunctions (Φ) and eigenvalues (E) of Hamiltonian $\hat{H}$.

Many-body system Hamiltonian

$$\hat{H} = -\frac{1}{2}\sum_{i=1}^{2N_e} \nabla^2_{\vec{r}_i} - \frac{1}{2}\sum_{j=1}^{2N_a} \frac{1}{M_j}\nabla^2_{\vec{R}_j} + U(r,R) \tag{3.10}$$

consists of the electrons (the first term) and nuclei (the second term, M_j is the nucleus mass) kinetic energy and the potential energy ($U(r,R)$) ($r = |\vec{r}|$ and $R = |\vec{R}|$ are the lengths of the position vectors). Here ∇^2 is the Laplace operator or Laplacian. The potential energy $U(r,R)$ term describes electron-electron, electrons-nuclei and nuclei-nuclei Coulomb interactions.

To solve this equation number of approximations should be applied. The first is Born-Oppenheimer or adiabatic approximation. Due to large mass difference between electrons and nuclei, the motion of electrons can be considered separately from nuclei motion. The second approximation is one electron approximation. The N-electron wave function (Φ) is approximated by a Slater determinant constructed from the one-electron wave functions (ϕ_i)

$$\Phi = \frac{1}{\sqrt{N!}} det[\phi_1 \phi_2 \phi_3 ... \phi_N]. \tag{3.11}$$

It satisfies anti-symmetry requirements for the wave function and ensures conformity to the Pauli principle.

To find one-electron functions (ϕ_i), the self-consistent field (SCF) or Hatree-Fock method is used. The one-electron wave functions are determined from variational principle by minimizing the functional

$$E = \int \phi_i^* \hat{H} \phi_i d\tau. \tag{3.12}$$

The lowest energy eigenvalue, E_0, is the ground state energy, and the probability density of finding an electron with any particular set of coordinates r_i is $|\phi_0|^2$.

The one-electron wave functions should satisfy the system of equations

$$\hat{F}\phi_i = \epsilon_i \phi_i \tag{3.13}$$

where $\hat{F}$ is the Hartree-Fock operator

$$F_{HF} = T + U_c + J + X, \tag{3.14}$$

which includes kinetic energy contribution (T), electron-nuclei Coulomb interaction (U_c), electron-electron Coulomb interaction (J) and HF exchange operator (X).

Another approach to the solution of the Schrödinger equation also exists and is called the density functional theory (DFT). It deals with electron densities and is based on the Hohenberg-Kohn (HK) theorems [52, 65] and Kohn-Sham equations [66]. The first HK theorem states that the one-to-one mapping between the ground state electron density, and the ground state wave function of a many particle system exist. The second HK theorem proves that the ground state density minimizes the total electronic energy of the system.

The difference between HF and DFT approaches is that in DFT electronic exchange ($X(\rho)$) and correlation ($C(\rho)$) interactions are additionally taken into account. Therefore, the Fockian operator in the KS theory is

$$F_{KS} = T + U_c + J + X(\rho) + C(\rho). \tag{3.15}$$

However, the calculation of these interactions is not a trivial task, because the exact functional forms are not known within the KS DFT. This leads to the different parametrization approximations for the KS exchange-correlation functional. The important formulations involve the local density approximation (LDA) and the generalized gradient approximation (GGA) [30].

The hybrid HF-DFT functionals, which include a part of the HF exchange (E_{HF}),

$$E_{XC} \approx aE_{HF} + bE_{XC}^{DFT} \tag{3.16}$$

were introduced and successfully applied in quantum mechanical calculations of solids [30]. The use of these functionals in the calculations allows one to increase accuracy for the obtained parameters such as optical band gap, atomic structure and vibrational frequencies [30].

In this work the CRYSTAL06 code [29] was used to calculate electronic, structural and phonon properties of several crystals. It implements ab initio Hartree-Fock linear combination of atomic orbitals (LCAO) method for the periodic systems [30]. In the LCAO approximation, the single electron wave functions are expanded over atomic-like basis functions χ_a (a = 1,...,M)

$$\phi_k(i) = \sum_{a=1}^{M} c_{ak}\chi_a(i), \tag{3.17}$$

and each atomic orbital (AO) is expressed as a linear combination of normalized Gaussian-type functions with constant coefficients and exponents [30].

For the heavy elements the number of basis functions necessary for their description is large due to large number of electrons. This leads to the high computational cost. The fact that the core electrons do not participate significantly in the chemical bonding allows one to separate description of core and valence electrons. The core electrons are described by one-particle potential (pseudopotential), and the valence electrons are described by effective core potential (ECP) [30]. The division to the core and valence electrons should be chosen depending on concrete system and type of calculations. Large and small core approximations are available [4]. Usually, the small core approximation is better used for compounds with d- and f-elements [30].

The CRYSTAL06 code [29] allows one to obtain many useful properties of the material such as the electronic band structure and the band gap value, the density of electronic states (DOS), charges on atoms and orbital occupancy, electronic density maps and atomization energy. The relaxation of atomic structure following to the minimum energy criterion is also possible. Bulk modulus, phonon frequencies and phonon dispersion curves can be calculated as well.

The charges on atoms were evaluated using the Mulliken population analysis [93]. The Mulliken charge on atom Q_A is defined as the difference between the number of electrons on the isolated free atom and the gross atom population GAP_A. The GAP_A is the sum over all orbitals belonging to the atom A and over all terms of the population matrix.

The bulk modules were calculated using the Murnaghan equation of state [94]

$$E(V) = E_0 + B_0 V_0 \left(\frac{1}{B'(B'-1)} \left(\frac{V_0}{V} \right)^{B'-1} + \frac{V}{B'V_0} - \frac{1}{B'-1} \right), \tag{3.18}$$

where V_0 is the equilibrium volume, B_0 is the zero-pressure bulk modulus, B' is the pressure derivative of the bulk modulus B at pressure $P = 0$), and E_0 is the equilibrium energy. The $E(V)$ dependence is calculated by varying unit cell parameters for few percents close to the equilibrium structure, thus simulating the effect of hydrostatic pressure. Next, the $E(V)$ dependence is fitted by Eq. 3.18, having four adjustable parameters (E_0, V_0, B_0, B').

The vibrational frequencies were calculated in the the harmonic approximation using the "frozen-phonon" approach [100]. In the "frozen-phonon" approach [69] the phonon energy is determined as the difference in the energies of the distorted and equilibrium crystalline lattices for a particular atom displacement. At Γ point of the Brillouin zone (BZ), the vibrational (phonon) frequencies are calculated by diagonalizing the dynamic matrix W

$$\begin{gathered} det|W(0)| = 0, \\ W_{ij}(0) = \sum_g \frac{H_{ij}^{0g}}{\sqrt{M_i M_j}} \end{gathered} \tag{3.19}$$

where H_{ij}^{0g} is the second derivative of the potential energy at equilibrium with respect to atom i in the reference cell 0 and atom j in cell g, M_i is the mass of the atom associated with the ith coordinate. H_{ij} are the Hessian matrix elements

$$H_{ij} = \frac{1}{2} \left[\frac{\partial^2 E}{\partial u_i \partial u_j} \right]_0 , \tag{3.20}$$

where u_i (i=1,2,...,3N) is a small displacement (±0.001 Å in the present work) of an atom along ith cartesian coordinate from equilibrium position, N is the number of atoms in primitive unit cell. The values of vibrational frequencies at the edge of the BZ were calculated using supercell method [100]. Calculation of the phonons for unit cell enlarged in the appropriate directions allows one to project defined BZ points onto the BZ center. Thus projecting one by one points from the BZ edge to the BZ center and calculating vibrational frequencies at the Γ point, the values of all required frequencies across the BZ can be evaluated.

3.4 Classical molecular dynamics simulations

When the force-field model is known, one can perform the classical molecular dynamics (MD) simulations. In the MD method, the time evolution of the system is described using the equation of motion or the second Newton's law [5]

$$\vec{F}_i = m_i \vec{a}_i . \tag{3.21}$$

This approach allows one to calculate static and dynamical properties of the system. However, since we apply the MD method to the many-atoms system, a general analytical solution is not possible and, therefore, the numerical simulations should be performed.

The total internal energy of the system, corresponding to the defined force-field model, is given by

$$U(r_{ij}) = \sum_i^N \sum_j^N u(r_{ij}). \tag{3.22}$$

The forces acting on the atoms can be expressed as a gradient of the potential energy

$$\vec{F}_i = - \bigtriangledown_i U. \tag{3.23}$$

Combining this equation and the Newton's second law, one obtains the equation relating the derivative of the potential energy to the changes of the particle position as a function of time

$$-\frac{dU}{d\vec{r}_i} = m_i \frac{d^2\vec{r}_i}{dt^2}. \tag{3.24}$$

Integration of the equations of motion then yields trajectories of all atoms.

During the MD simulation the state of each atom is characterized by its position (coordinates) and velocity. Starting MD simulation for crystalline material, one can conveniently place all atoms at their equilibrium positions, which are defined by the potential model. Thus, the starting positions correspond to the energy minimum of the potential model. However, the velocities of atoms at the beginning of the simulation are not defined. The initial distribution of velocities is usually determined from a random distribution with the probabilities conforming to the required temperature and corrected so that there is no overall momentum

$$\vec{p} = \sum_{i=1}^{N} m_i \vec{v}_i = 0. \tag{3.25}$$

The velocities can be chosen randomly from a Maxwell-Boltzmann or Gaussian distribution at a given temperature, which gives the probability that at the temperature T an atom i has a velocity v_x in the x direction. During the simulation the temperature T is re-calculated from the velocities as

$$T = \frac{2}{3Nk_B} \left\langle \frac{1}{2} \sum_{i}^{N} m_i \vec{v}_i^2 \right\rangle . \tag{3.26}$$

where N is the atoms number, and k_B is the Boltzmann constant.

As was mentioned before there is no analytical solution to the equations of motion, therefore they must be solved numerically. A number of integration algorithms exists, and in this work the so-called "leap-frog" integration algorithm was used [41].

The thermodynamic properties of the system can be calculated from the MD simulation results using the ergodic hypothesis assuming that the statistical ensemble averages are equal to the time averages of the system. The ensembles are defined by fixing macroscopic properties. The most popular ensembles for the MD simulations are the microcanonical ensemble (NVE), having fixed number of atoms (N), volume (V) and energy (E), the canonical ensemble (NVT), having fixed number of atoms (N), volume (V) and temperature (T), and the isothermal-isobaric ensemble (NPT), that maintains constant number of atoms (N), pressure (P) and temperature (T). The NVE ensemble corresponds to an adiabatic process with no heat exchange. In the NVT ensemble, the energy of endothermic and exothermic processes is exchanged with a thermostat. In addition to a thermostat, a barostat is needed for the NPT ensemble. It corresponds most closely to laboratory conditions with a flask open to ambient temperature and pressure.

In this work the MD simulations are performed for crystalline systems, having the unit cells *a priori* known with good accuracy, with the main goal to do next simulations of the EXAFS spectra at required temperature. Therefore, the NVT ensemble has been used as the most suitable for our needs. The NPT ensemble can be also used, however, the variation of the cell parameters caused by the maintenance of the constant pressure can possibly introduce undesired artifacts during EXAFS simulations, since the change of the unit cell strongly effects the EXAFS signal.

In simulations of crystalline materials, which have translational symmetry, the periodic boundary conditions are employed. As a result, the correlations in space beyond half cell width are artificial. For this reason the interaction potentials cut-off distance (r_{cut}) should be no larger than the half cell width. One should not also calculate structural properties like the radial distribution functions for distances larger than the half cell width.

The main result of the MD simulations is atoms movement trajectory. Because the time is discrete, the results can be represented as a set of snapshots of the system. The single snapshot is called atomic configuration. So, a set of atomic configurations is used to calculate structural and dynamical properties.

The structural properties include the pair correlation or radial distribution functions $G(r)$

$$G(r) = \frac{V}{N^2}\langle\sum_i\sum_{j\neq i}\delta(r - r_{ij})\rangle. \tag{3.27}$$

Note that $G_{EXAFS}(r)$ function obtained from EXAFS analysis for the first coordination shell can be directly compared with $G_{MD}(r)$ from the MD simulations. Such comparison with the experimental data can help to evaluate the results of the MD simulations before doing time consuming EXAFS calculations.

The mean-square displacements (MSD) (Eq. 3.28) and mean-square relative displacements (MSRD) (Eq. 3.29 and Fig. 3.3) can be evaluated from a set of atomic

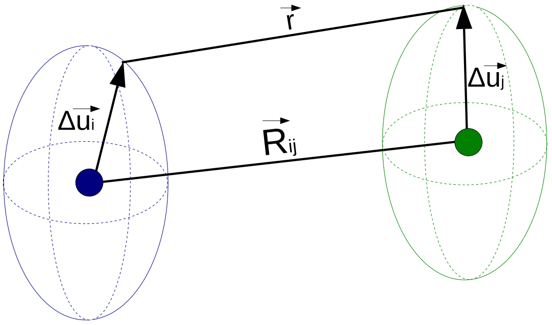

Figure 3.3: Atomic displacements $\Delta\vec{u}$ for two atoms i and j, located at the average distance $|\vec{R}_{ij}|$. $|\vec{r}|$ is the instantaneous interatomic distance. Thermal ellipsoids are also shown for both atoms.

configurations.

The MSD function is defined as [36, 124]

$$MSD = \langle(\hat{R}\cdot\Delta\vec{u}_i)^2\rangle. \tag{3.28}$$

The MSRD function parallel to the chemical bond is defined as [36, 124]

$$MSRD_{\|ij} = \langle(\hat{R}\cdot\Delta\vec{u}_i)^2\rangle + \langle(\hat{R}\cdot\Delta\vec{u}_j)^2\rangle - 2\langle(\hat{R}\cdot\Delta\vec{u}_i)(\hat{R}\cdot\Delta\vec{u}_j)\rangle. \tag{3.29}$$

where angular brackets denote a thermal average, $\hat{R}$ is a unit vector pointing from atom i to atom j, $\Delta\vec{u}_i = \vec{u}_i - \vec{u}_0$ is the instantaneous displacement of atom i. The MSRD function reflects the correlation in the motion of two atoms. The first two terms in Eq. 3.29 correspond to the MSD functions for atoms i and j, the last term is the displacement correlation function (DCF)

$$MSRD_{\|ij} = MSD_i + MSD_j - DCF_{ij}. \tag{3.30}$$

The MSD can be obtained from diffraction measurements, whereas the MSRD is probed by EXAFS spectroscopy. In the harmonic approximation, the MSRD coincides with σ^2 in the Debye-Waller-type term of the conventional EXAFS formula 2.11.

An additional property, which can be used to test the accuracy of the MD simulation, is the EXAFS signal. In the next section, the ab initio calculations of the configuration averaged EXAFS signals based on the atomic configurations from the MD simulation will be discussed.

3.5 Ab initio calculation of configuration averaged EXAFS

The MD simulation provides with a set of atomic configurations. Each single configuration describes a static state of the system at some moment of time. The set of such configurations can be used to calculate properties depending on the atomic coordinates. In the case of EXAFS, each static atomic configuration is used to calculate single EXAFS spectrum taking into account all multiple-scattering contributions. Since each atomic configuration is static, there is no need to introduce the disorder effects in the multiple-scattering formalism. Finally, the configuration averaged EXAFS signal, inherently including thermal and static disorder, is calculated as

$$\chi(k) = \frac{1}{N_t} \sum_{t=1}^{N_t} \left(\sum_n \sum_j \frac{N_j f_j^n(k,t)}{k R_j^2(t)} \sin[2kR_j(t) + \delta_j^n(k,t)] \right) \tag{3.31}$$

where n is the multiple-scattering order (single-scattering, double-scattering, triple-scattering, etc.), j is the atomic group number, N_j is the degeneracy of the scattering path involving atom(s) of the j-group, $2R_j(t)$ is the scattering path length, $f_j^n(k,t)$ and $\delta_j^n(k,t)$ are the scattering amplitude and total phase shift functions. The "time" variable t indicates the number of the atomic configuration in the MD simulation. N_t is the total number of atomic configurations.

For the accurate simulation of the EXAFS spectra, the set of atomic configurations should fulfill some conditions.

The first is the number of configurations, which is proportional to the time of the MD simulation. The characteristic time of the photoabsorption process is in the range of 10^{-15}-10^{-16} seconds. The characteristic time of the atomic vibrations is much longer being in the range of 10^{-13}-10^{-14} seconds. This means that a single photoabsorption process sees "frozen" atomic structure. However, the time of the EXAFS experiment is in the range of minutes, and, thus, the resulting EXAFS signal equals to a superposition of EXAFS signals from many static configurations. Therefore, for a solid, where atoms move close to their equilibrium positions, the simulation time should be larger than the characteristic time of the atomic vibrations. Ideally, one should choose the number of atomic configurations enough large to have the average over the statistical ensemble in the MD simulation close to the average over time in the experiment. In this work, the number of atomic configurations used in the calculation of the averages was at least 4000. Moreover, the convergence of both the average atomic structure and the average EXAFS signal were controlled.

The second condition is that the time step in the MD simulation should be enough small to sample correctly the highest characteristic frequency of the material and to guarantee accurate integration of the equations of motion, thus resulting in a smooth trajectory for all atoms. The highest characteristic frequency of the material can be estimated either experimentally from the Raman or IR spectra as well as from inelastic scattering experiments or theoretically from lattice dynamics calculations. In this work, the estimated time step of 0.5 fs was used.

The third condition is the size of the MD simulation box. In the simulations of solid materials the periodic boundary conditions are used. This leads to the correlations between atomic movements at distances larger than the size of the box. Therefore, the calculation of EXAFS signal without artificial correlations is possible only at distances smaller than half of the box dimensions. For example, to analyse structural contributions in the EXAFS signal till 6 Å the size of the MD simulation box should be at least 12 Å in all dimensions.

Another important note should be made regarding the computer code, which is used to calculate EXAFS signal for the static configuration. In this work we use the ab initio real-space multiple-scattering FEFF8.x code [10, 108], thus the EXAFS signals are calculated taking into account all multiple scattering contributions to the eighth order. The number of the multiple-scattering paths increases roughly exponentially with the box size, thus arriving rapidly to the maximum number of paths, which can be treated by the FEFF code due to the computer memory limitations. Of course, the MS paths number varies depending on the material. In this work, for all crystals we were able to calculate the configuration averaged EXAFS signals for the cluster sizes of at least 6 Å.

4

Experimental

4.1 Sample preparation

4.1.1 Rhenium trioxide ReO_3

Rhenium trioxide (cubic, space group $Pm\bar{3}m$) ReO_3 sample, studied in the present work, was commercial polycrystalline powder (99.9% purity, Metalli Preziosi S.p.A.), having a red colour.

4.1.2 Calcium tungstate $CaWO_4$

Polycrystalline (tetragonal, space group $I4_1/c$) $CaWO_4$ was commercial powder (99.9% purity), having a white colour.

4.1.3 Zinc tungstate $ZnWO_4$

$ZnWO_4$ nanoparticles were synthesized using co-precipitation technique [54, 62] by the reaction of $ZnSO_4 \cdot 7H_2O$ and $Na_2WO_4 \cdot H_2O$ at room temperature (20°C), pH=8, and reaction time 1-2 hours. All chemicals were used analytic grade reagents (purity 99%, "Reahim") without further purification. The water solutions of the two salts were prepared by dissolving 10 mmol of the salt in 100 ml of double-distilled water with vigorous stirring. Next they were mixed in 1:1 molar ratio, and white precipitates appeared immediately. After completion of the reaction, the precipitate was filtered off, washed several times with double-distilled water, and dried in air for 12 hours at 80°C thus resulting in the white-colored nanocrystalline $ZnWO_4$ powder. The obtained

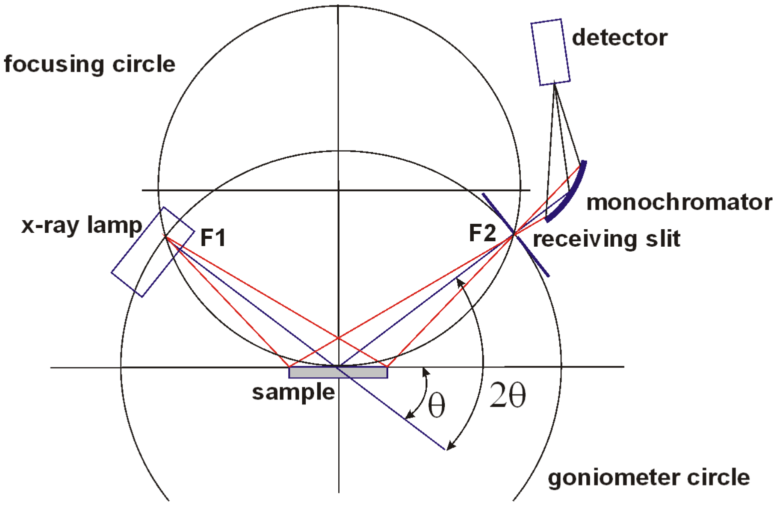

Figure 4.1: Schematic view of Bragg-Brentano powder diffractometer with a monochromator [2]

powder were annealed in air for 4 hours at different temperatures up to 800°C. Thus obtained powder have white colour.

4.2 X-ray powder diffraction

X-ray powder diffraction (XRD) patterns were recorded at room temperature (20°C) using a θ-θ Bragg-Brentano powder diffractometer (Fig. 4.1) with a graphite monochromator in the diffracted beam and a Na(Tl)I detector. Conventional tube with copper anode (Cu Kα radiation, U=40 KV, I=35 mA), cooled by water, was used as X-ray source. The scans were performed in the 2θ-space with the step $\Delta(2\theta) = 0.05°$.

4.3 Infra-red spectroscopy

Infra-red (IR) absorption spectra were collected at room temperature (20°C) using a Brucker Equinox 55 Fourier transform infra-red (FTIR) spectrometer (Fig. 4.2). The experiments were performed in transmission mode using Globar IR source which cover 350-7000 cm^{-1} range, KBr beamsplitter and KBr/DLaTGSD301 detector. The samples were mixed and pressed with optical grade KBr powder, thus obtaining IR transparent tablets. The sample chamber was blown out with dry nitrogen gas to reduce absorption by air.

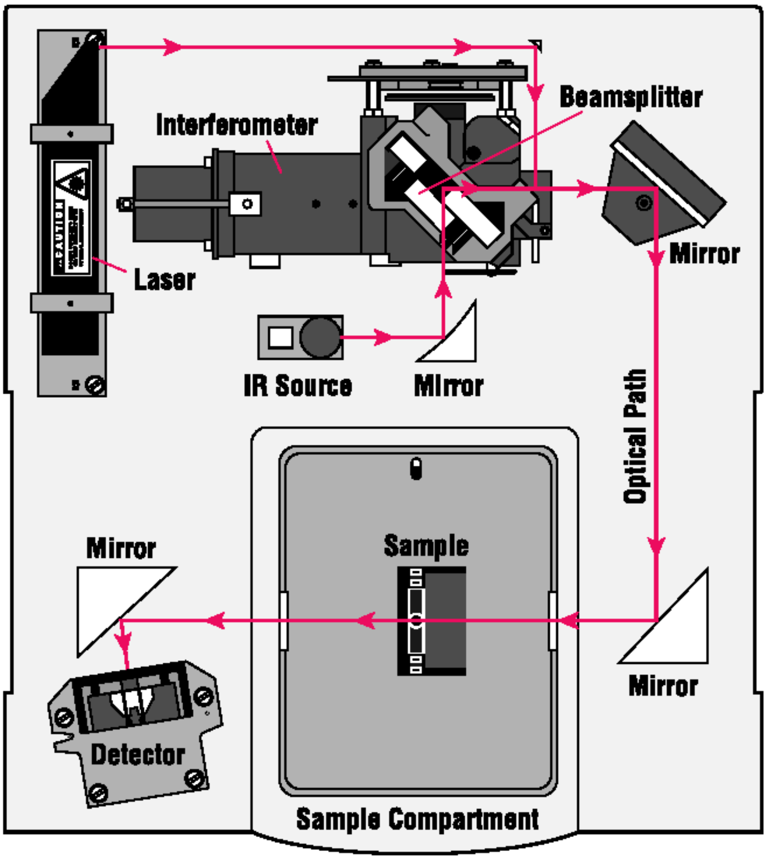
Interferometer
Beamsplitter
Mirror
Laser
IR Source
Mirror
Optical Path
Sample
Mirror
Mirror
Detector
Sample Compartment
CAUTION

Figure 4.2: Schematic view of FTIR spectrometer

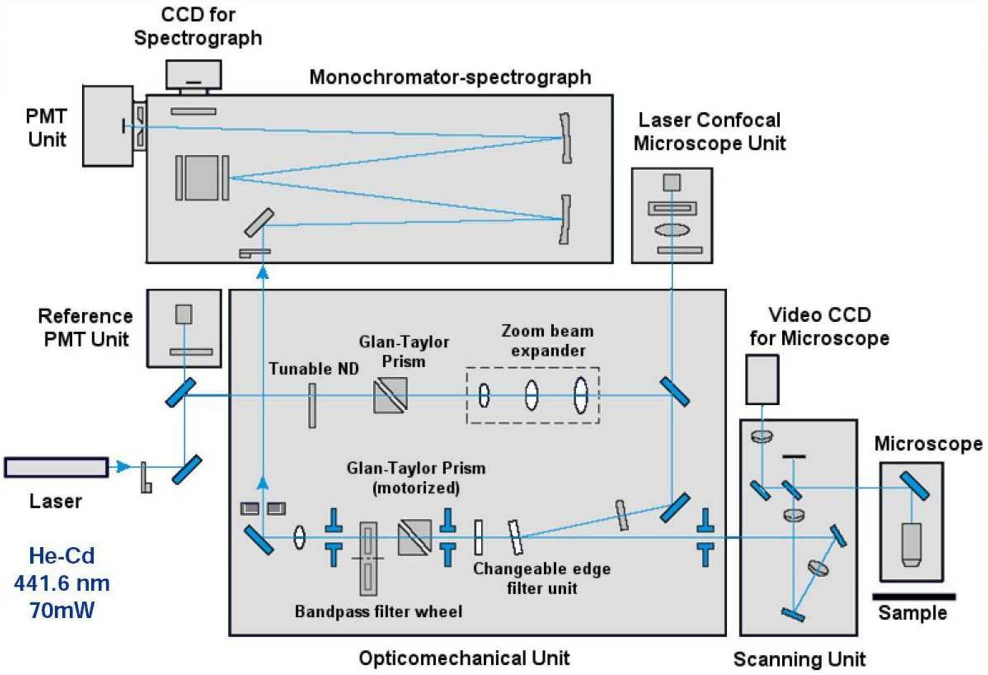
CCD for Spectrograph
Monochromator-spectrograph
PMT Unit
Laser Confocal Microscope Unit
Reference PMT Unit
Tunable ND
Glan-Taylor Prism
Zoom beam expander
Video CCD for Microscope
Microscope
Laser
He-Cd
441.6 nm
70mW
Glan-Taylor Prism (motorized)
Changeable edge filter unit
Bandpass filter wheel
Sample
Opticomechanical Unit
Scanning Unit

Figure 4.3: Schematic view of the scanning confocal microscope with spectrometer "Nanofinder-S" [1]

4.4 Raman spectroscopy

Raman spectra were collected at room temperature (20°C) using a confocal microscope with spectrometer "Nanofinder-S" (Fig. 4.3) (SOLAR TII, Ltd.) [75]. The measurements were performed through Nikon Plan Fluor 40× (NA=0.75) optical objective. The Raman spectra were excited by a He-Cd laser (441.6 nm, 50 mW cw power) and dispersed by 1800 grooves/mm diffraction grating, having a resolution of about 2.5 cm^{-1} and mounted in the 520 mm focal length monochromator. The Peltier-cooled back-thinned CCD camera (ProScan HS-101H, 1024×58 pixels) was used as a detector. The elastic laser light component was eliminated by the edge filter (Omega, 441.6AELP-GP).

4.5 Photoluminescence spectroscopy

Photoluminescence experimental set-up is shown on Fig. 4.4. The photoluminescence spectra and decay kinetics were measured using pulsed YAG:Nd laser excitation (4.66 eV, 8 ns) at room temperature (20°C). Luminescence registration carried out by photomultiplier tube HAMAMATSU H8259 and photon counting board (fastComTec Communication Technology module P7888-1E) with the time resolution 2 ns. The photoluminescence kinetics for each sample were collected at three energies, corresponding to the intrinsic luminescence band maximum and two band edges. The three kinetics were close, therefore only data, taken at the band maximum, will be presented due to their better statistics.

4.6 X-ray absorption spectroscopy

X-ray absorption measurements were performed in transmission mode at the HASYLAB DESY C1 bending-magnet beamline (Fig. 4.5) in the temperature range of 10-300 K at Zn K (9659 eV) and W L_3 (10207 eV) edges. The storage ring DORIS III was used as an x-ray source. It operated at E=4.44 GeV and I_{max}=140 mA in a 5 bunches mode with a lifetime of 4 h. The higher-order harmonics were effectively eliminated by detuning of the monochromator Si(111) crystals to 60% of the rocking curve maximum, using the beam-stabilization feedback control. The x-ray beam intensity was measured by three ionization chambers filled with argon and krypton gases.

The Oxford Instruments liquid helium flow cryostat was used to maintain the required sample temperature. The temperature was stabilized to within ±0.5 degrees during each experiment. Several samples of $ZnWO_4$ and $CaWO_4$ were prepared by depositing an appropriate amount of the powder on Millipore filters and fixing by a Scotch tape. The deposited powder weight was chosen to give the absorption edge jump value $\triangle\mu x \simeq 1.0$ at the Zn K or W L_3 edges. The tungsten foil was used as the reference sample to control monochromator stability.

Experimental temperature-dependent EXAFS spectra for the Re L_3-edge in polycrystalline ReO_3 were taken from [105].

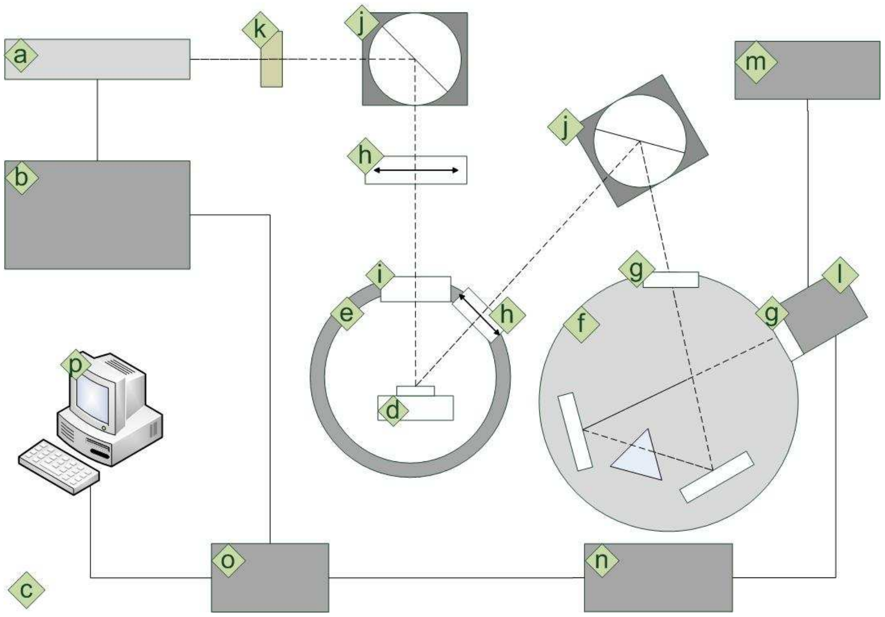

Figure 4.4: Schematic view of the photoluminescence experimental setup:

a. YAG:Nd solid state laser with 266 nm wavelength (4.66 eV) and 8 ns pulse length;

b. Feed and control module for laser;

c. Optical table;

d. Sample holder;

e. Vacuum system;

f. Carl Zeiss Jena SPM-1 prism monochromator;

g. Monochromator entrance and exit slits;

h. Quartz lenses;

i. Quartz window;

j. Adjustable mirror;

k. 266 nm interference filter;

l. Photomultiplier tube HAMAMATSU H8259;

m. Photomultiplier tube feeding module;

n. Pulse selector;

o. Ultrafast multiscaler P8777-1E photon counting board;

p. Control computer

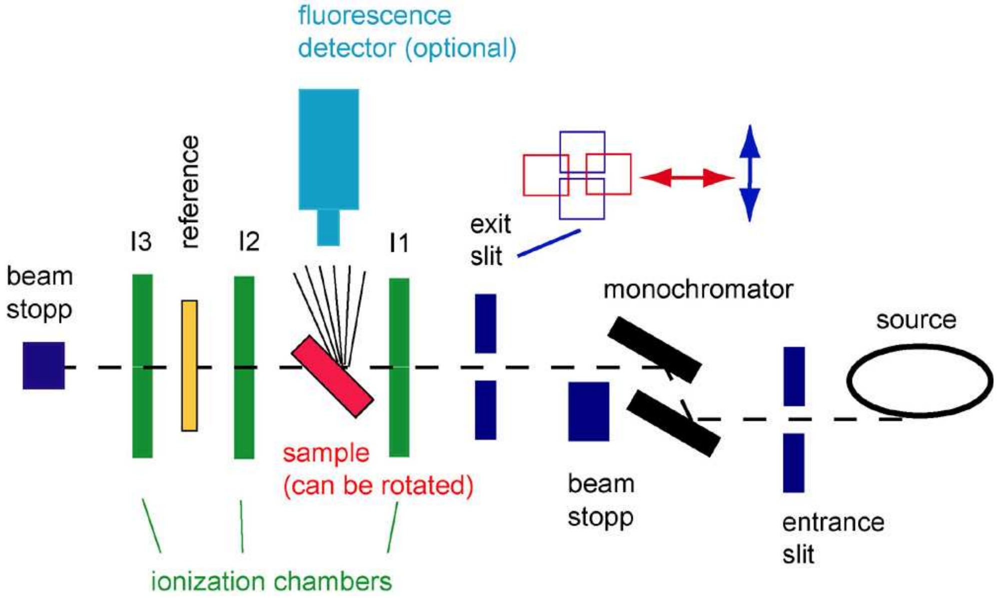
fluorescence
detector (optional)
reference
I3
I2
I1
exit
slit
monochromator
beam
stopp
source
sample
(can be rotated)
beam
stopp
entrance
slit
ionization chambers

Figure 4.5: Schematic view of the EXAFS experiment at C beamline DORIS III storage ring. The setup consists of the x-ray source (the storage ring), variable entrance and exit slits, double-crystal monochromator, three ionization chambers (I1, I2, and I3), beam stopper. The position of the unknown and reference samples and the optional fluorescence detector (not used in the present work) are also shown [3]

5

Results

5.1 Local structure in $ZnWO_4$ nanoparticles

5.1.1 X-ray diffraction

Polycrystalline $ZnWO_4$ powder has monoclinic (space group $P2/c$) wolframite-type structure built up of distorted [WO_6] and [ZnO_6] octahedra joined by edges into infinite zigzag chains, consisting of octahedral units of the same type and running parallel to c-axis [68, 114, 122]. The octahedra distortion results in the splitting of the W–O and Zn–O distances into three groups with the bond lengths of 1.790 Å, 1.905 Å and 2.130 Å for tungsten atoms and 2.023 Å, 2.086 Å and 2.217 Å for zinc atoms [68, 114, 122]. Our XRD measurements [62] confirm the wolframite-type of microcrystalline $ZnWO_4$, whereas no Bragg peaks appear in the XRD pattern for nanoparticles (Fig. 5.1), indicating that the nanoparticles size is below 2 nm.

5.1.2 Raman and optical spectroscopy

The vibrational properties of nanoparticles and reference microcrystalline $ZnWO_4$ were studied by Raman spectroscopy, which is sensitive to local vibrations and, thus, is perfectly suitable for nanoparticles studies [42].

The Raman spectra of $ZnWO_4$ powders change significantly depending on the annealing temperature (Fig. 5.2). According to their overall shape, one can distinguish three annealing ranges: below 400°C, at 400–450°C and above 450°C. It is convenient to start a discussion from the results for high-temperature annealing region.

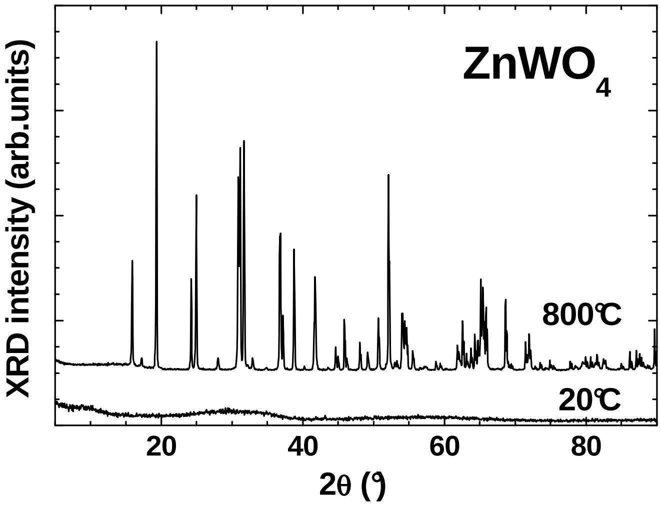

Figure 5.1: X-ray powder diffraction patterns of as-prepared (20°C) and annealed at 800°C $ZnWO_4$ powders.

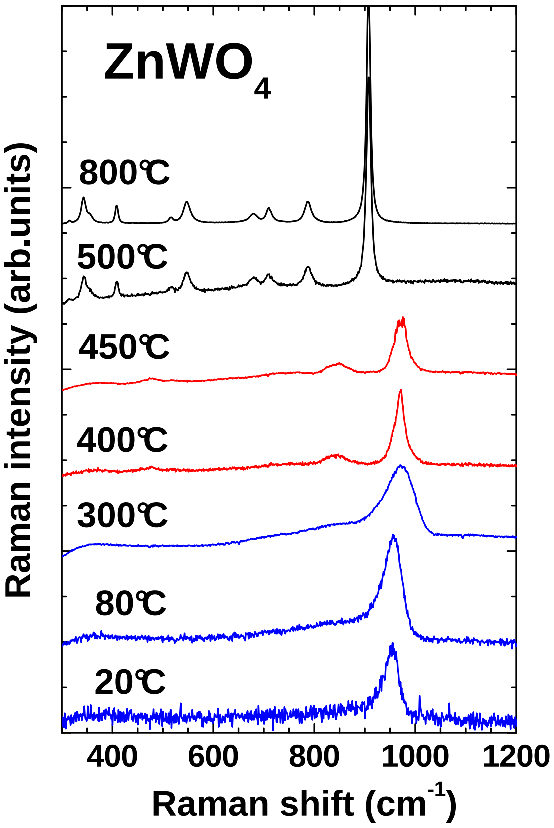

Figure 5.2: Raman scattering spectra of $ZnWO_4$ powders annealed at different temperatures. Measurements were performed at 20°C.

Group theory analysis for wolframite-type $ZnWO_4$ predicts 36 lattice modes, of which 18 even vibrations ($8A_g + 10B_g$) are Raman active. Eleven of them are expected [84, 127] in the frequency range accessible in our experiment due to the cut-off at $\sim$270 cm^{-1} by the edge filter of the spectrometer. In fact, all expected lines (907, 787, 709, 679, 547, 516, 409, 355, 343, 315 and 276 cm^{-1}) are observed in the Raman signal for powder annealed at 800°C. Note that the highest frequency line at 907 cm^{-1}, corresponding to the stretching W–O mode, has a linewidth about 9 cm^{-1}. At low annealing temperature (500°C), the Raman lines of wolframite-type $ZnWO_4$ are broadened due to a reduction and a dispersion of the crystallites size but still can be detected.

For the annealing in the range of 400–450°C, the Raman spectrum changes dramatically and is composed of five broad lines: 320–420 cm^{-1}, 430–560 cm^{-1}, 670–800 cm^{-1}, 800–900 cm^{-1} and the intense line at 971 cm^{-1} with the linewidth 20–30 cm^{-1}. This result cannot be due to homogeneous or inhomogeneous broadening, but should be caused by some relaxation of $ZnWO_4$ particles structure upon their size reduction. Note that heating of polycrystalline $ZnWO_4$ up to 1227°C (below melting temperature) leads to homogeneous Raman line broadening and only slightly affects the lines position [13, 126].

The Raman spectra of samples, annealed at temperatures below 400°C, are close enough to that from previous group, but further significant lines broadening occurs. The signals consist of one main line at 950-960 cm^{-1} with a linewidth equal to 50-70 cm^{-1} and a broad line with low intensity at 700-900 cm^{-1}. There is also some evidence of a weak broad line spreading from 300 to 500 cm^{-1}. It is interesting that these Raman signals are close to that observed for $ZnWO_4$ melt in Refs. [13, 126], where the origin of lines has been attributed to the internal vibrational modes of isolated $[WO_4]^{2-}$ complexes.

Our interpretation of the observed Raman signals shape does not support the appearance of tetrahedral $[WO_4]$ groups in as-prepared or annealed at low-temperature $ZnWO_4$ powders. We believe that due to a small particle size, being in the nanoscale range, the large surface-to-bulk ratio leads to the strong relaxation of the particle structure. Additionally, the surface tungsten–oxygen bonds could play an important role. It is known that the sharp Raman line around 950 cm^{-1} is observed in crystalline tungsten hydrates and is attributed to the short double terminal W=O bonds [27]. Besides, similar but broad line is observed in ground pure WO_3 powder and has been attributed to the W^{6+}–O^{-} or W^{6+}–OH surface terminating bonds in Ref. [81]. Further support for the octahedral coordination of tungsten is provided by photoluminescence results given below.

The photoluminescence spectra of $ZnWO_4$ powders (Fig. 5.3) consist of a broad band, peaked at about 2.5 eV. The band position and the bandwidth dependence on the annealing temperature are shown in Fig. 5.4. The band has a complex shape, which envelops three emission bands, namely yellow at 2.28 eV, green at 2.51 eV, and blue at 2.80 eV. The green-blue luminescence is believed to be due to radiation transitions of the charge transfer type between oxygen and tungsten states in regular octahedral [WO_6] groups [19, 67, 95, 99], while yellow luminescence was tentatively attribute to defective tungsten groups lacking one oxygen atom [85]. The photoluminescence kinetics, measured at the band maximum, in the time interval up to 25 μsec, are shown in Fig. 5.3. As in the case of the Raman spectra, one can distinguish three temperature ranges: below 400°C, at 400–450°C and above 450°C.

When annealing above 450°C, the photoluminescence spectra of $ZnWO_4$ powders are close to that of single crystal with a maximum at about 2.51 eV at room temperature [58] and a bandwidth of about 0.52 eV. The kinetics can be fitted as a sum of three exponents, and decay time values are in good agreement with that in Ref. [58], where high laser power was used.

For $ZnWO_4$ powders annealed in the intermediate temperature range (400–450°C), the photoluminescence band maximum shifts to the lower energy, and the bandwidth is larger (∼0.55 eV) than that for the powders annealed above 450°C, and for single crystal. The photoluminescence kinetics are faster and more complex, so that they cannot be fitted with three exponents.

In the temperature range below 400°C, the photoluminescence spectra maximum shifts further to lower energies, but some spread in the band maximum position is observed. The bandwidth is larger (∼0.60 eV), and kinetics becomes even faster. In nanoparticles (below 80°C), the photoluminescence band experiences a red shift by ∼0.15 eV, and the complex shape of the band becomes evident: it can be decomposed into three sub-bands peaked at 2.14 eV, 2.40 eV, and 2.69 eV. The red shift of the band allows one to exclude the presence of the quantum size effect, which should cause, on the contrary, a blue shift. The photoluminescence decay kinetics in nanoparticles is faster than in microcrystalline $ZnWO_4$ (Fig. 5.4) and cannot be described by three

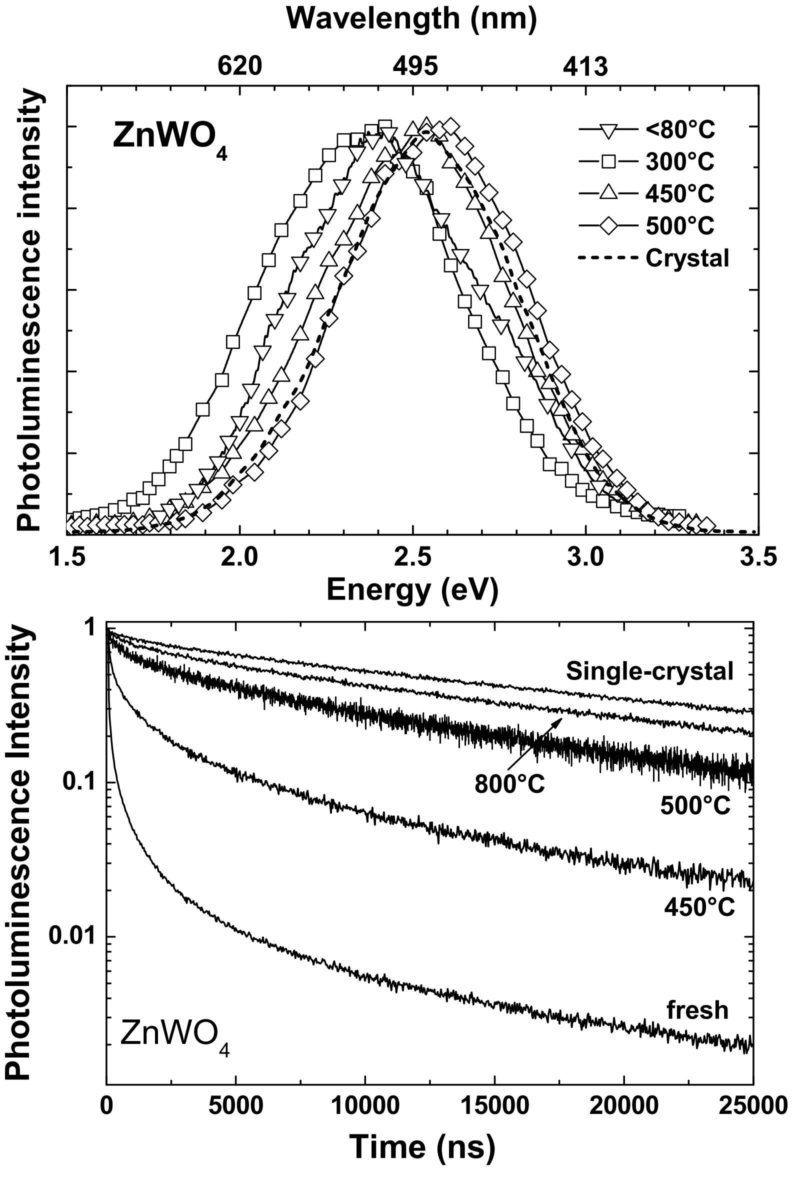

Figure 5.3: (upper panel) Photoluminescence of $ZnWO_4$ powders annealed at different temperatures. The spectra intensities are normalized at the band maximum. (lower panel) Photoluminescence kinetics, measured at the intrinsic band maximum (~2.5 eV), in $ZnWO_4$ powders annealed at different temperatures. Measurements were performed using pulsed YAG:Nd laser excitation (4.66 eV, 8 ns) at 20°C.

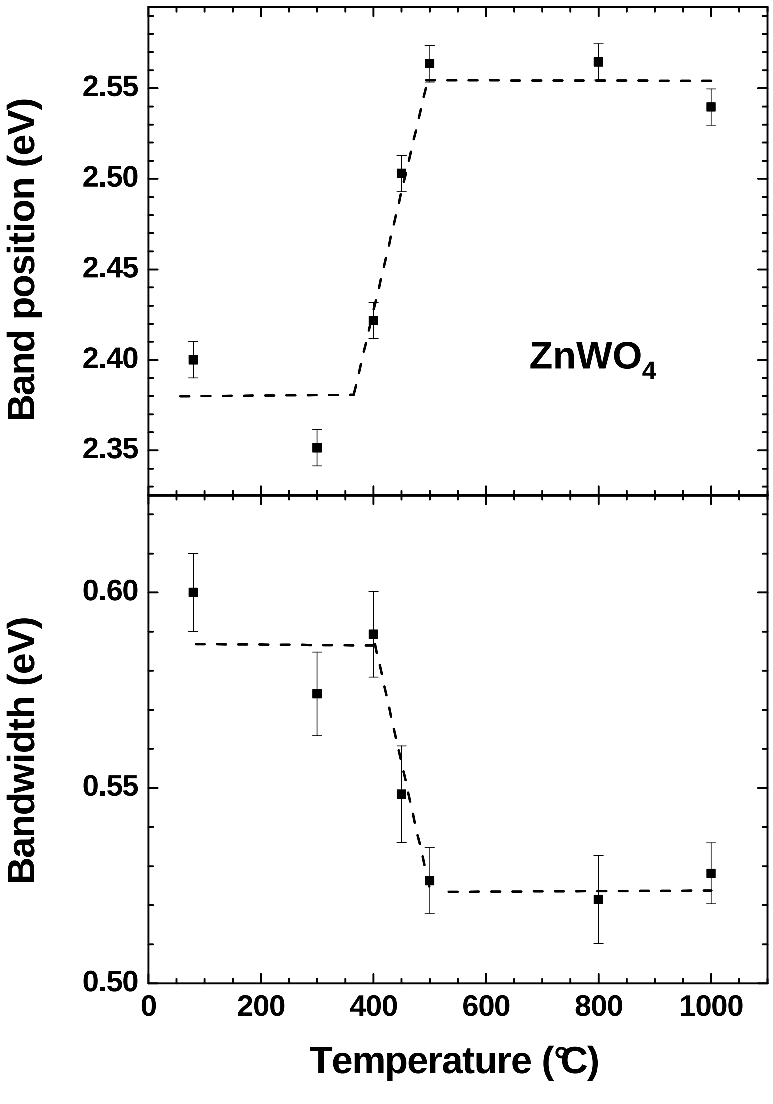

Figure 5.4: Photoluminescence band maximum position (top plot) and the bandwidth (bottom plot) in $ZnWO_4$ powders annealed at different temperatures. The point T= 1000°C corresponds to the single crystal. The dashed lines are guides for eye.

component exponential decay, associated with the three types of self-trapped excitons [19], opposite to the case of microcrystalline [62, 68] or single-crystal [58] $ZnWO_4$.

The behavior of photoluminescence spectra from $ZnWO_4$ powders allows us to draw several conclusions. First, we did not observe in our powders the quantum size effect, leading to a blue shift of the luminescence band, which one may expect for a nanosized material [60]. Our result agrees well with that for $ZnWO_4$ thin films [85] and nanoparticles [128], having a size of 28–56 nm. The absence of the quantum size effect can be explained by the origin of the luminescence. It is due to electronic transitions of the charge transfer type between oxygen and tungsten states in the $[WO_6]^{6-}$ molecular complexes [67, 95, 99], which exist in $ZnWO_4$ powders independently from the particle size.

The position of the photoluminescence band allows us also to exclude another scenario, in which the relaxation leads to a transformation of octahedral $[WO_6]$ groups into tetrahedra $[WO_4]$. However, in this case, one expects a blue shift of the luminescence band maximum to $\sim$2.95 eV, which is typically observed in scheelites, for example, $CaWO_4$ [89].

Some variation in the photoluminescence band position, observed in Fig. 5.3, can be related to a change in the distortion of the $[WO_6]^{6-}$ complexes, caused by a change of the particle size and an influence of surface defects. At low annealing temperatures (below 400°C), the average size of $ZnWO_4$ particles is small (below $\sim$20 nm), as follows from diffraction experiments [51, 91], and, thus, the number of $[WO_6]$ groups located at the particle surface, whose atoms relax more than of those located in the bulk, increases. For $ZnWO_4$ nanoparticles, a simple estimate suggests that by taking the approximate size of the $[WO_6]$ or $[ZnO_6]$ octahedra being about twice the metal-oxygen bond – 4 Å, the nanoparticle with a size of 2 nm will consists of less than 125 octahedral units, most (80%) of which will be located at the surface. As a result, the relaxation of the structure is inevitable leading to the decrease of the band gap and to appearance of defect centers able to trap excitons with different lifetimes. Such picture agrees well with the Raman results, discussed above, and with the results of our recent studies of the excitation spectrum in nano-sized $ZnWO_4$ [61], which indicate a decrease of the optical band gap.

Significant changes of the luminescence kinetics may be also related to the deformation of $[WO_6]^{6-}$ complexes. It has been shown in [19, 26, 68] that the luminescence

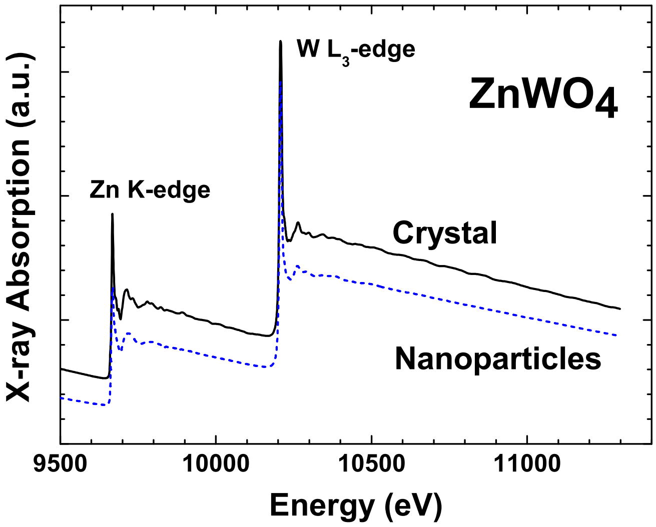

Figure 5.5: The Zn K and W L_3 edges x-ray absorption spectra of nanoparticles (dashed line) and microcrystalline (solid line) $ZnWO_4$ measured at 10 K. The two edges are separated by ~550 eV.

kinetics in single crystal and polycrystalline $ZnWO_4$ can be approximated by three exponents. Corresponding decay times can be associated with three types of self-trapped excitons (STE) [19]. In our samples produced at low annealing temperatures, kinetics are faster and cannot be adequately described by three exponential decay functions. This fact can be explained by the presence of a large number of defects, appearing in small $ZnWO_4$ particles of different size and able to trap excitons with different lifetimes. For high annealing temperatures, the larger particles with less amount of defects are responsible for that the distribution of lifetimes becomes narrower.

Thus, the direct proof of the metal-oxygen octahedra distortion in nanoparticles is required to provide a solid basis for above mentioned explanations. This information has been obtained by x-ray absorption spectroscopy independently for W and Zn environments. Moreover, the temperature dependent EXAFS study allowed us to separate the static and thermal disorder contributions.

5.1.3 EXAFS spectroscopy

X-ray absorption spectra (Fig. 5.5) were analyzed using the EDA software package [70]. The photoelectron energy origin E_0, used in the definition of the photoelectron wavenumber $k = [(2m_e/\hbar^2)(E - E_0)]^{1/2}$ was set at 10210 eV for W L_3-edge and at

9664 eV for Zn K-edge to have the best match between k-space scales of the experimental and theoretical, calculated by the FEFF8.2 code [108], EXAFS signals.

The experimental temperature dependent W L_3-edge and Zn K-edge EXAFS spectra in nanoparticles and microcrystalline $ZnWO_4$ are shown in Fig. 5.6. The EXAFS signals for nanoparticles show weak temperature dependence and do not contain high-frequency contributions that indicates on the absence of long-range order. In fact, the Fourier transforms of the EXAFS spectra, shown in Fig. 5.6 and calculated with the 10% Gaussian window-function, support this conclusion. While in microcrystalline $ZnWO_4$ the structural peaks are well visible up to 8 Å, the ordered region in nanoparticles is limited by about 4 Å. Note that the positions of the FT peaks are shifted in Fig. 5.6 from their true crystallographic values because the FTs were calculated without phase-shift corrections. In this work only the first coordination shell contributions, singled out by the back-FT procedure in the range of ≃0.8-2.4 Å, are considered.

The first coordination shell contribution from nearest oxygen atoms gives a strong peak at 0.8-2.4 Å and is comparable in both nanoparticles and microcrystalline $ZnWO_4$. However, already the second peak at ≃3 Å, being due to contributions from outer shells and multiple-scattering effects generated within the first shell, is strongly damped in nanoparticles. Further we analyze and discuss only the first coordination shell contribution.

First, we have tried to analyze the first shell EXAFS signals using the conventional method, based on the multi-component fitting procedure within the Gaussian/cumulant approximations. However, the fitting procedure did not gave good results, especially, in the case of nanoparticles. This indicates on the complex shape of the atomic distributions, in particular, strong distortion of the first shell octahedra. Therefore, a model-independent approach [78] allowing the reconstruction of the true RDF $G(R)$ was used. The required in simulation scattering amplitude and phase shift functions for W–O and Zn–O atom pairs were calculated by ab initio multiple-scattering code FEFF8.2 [108] using the complex exchange-correlation Hedin-Lundqvist potential. The calculations were performed based on the crystallographic structure of $ZnWO_4$ [68, 114, 122], considering a cluster of 8 Å size around the absorbing atom (W or Zn). Calculations of the cluster potentials were done in the muffin-tin (MT) self-consistent-field approximation using default values of MT radii as provided within the FEFF8.2 code [108].

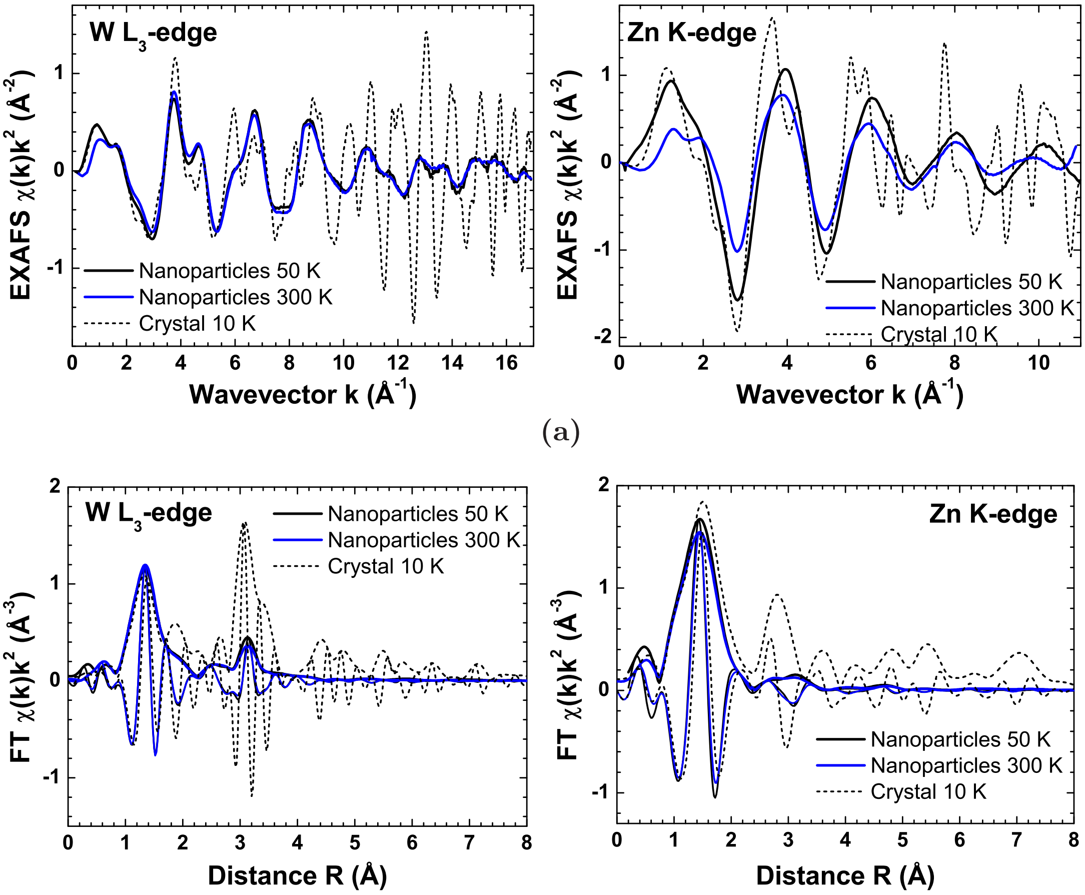

(a)

(b)

Figure 5.6: (a) Experimental W L$_3$-edge and Zn K-edge EXAFS spectra $\chi(k)k^2$ of nanoparticles and microcrystalline ZnWO$_4$. Only representative signals are shown for clarity. (b) Fourier transforms of the experimental W L$_3$-edge and Zn K-edge EXAFS spectra $\chi(k)k^2$ of nanoparticles and microcrystalline ZnWO$_4$. Both modulus and imaginary parts are shown. Only representative signals are shown for clarity.

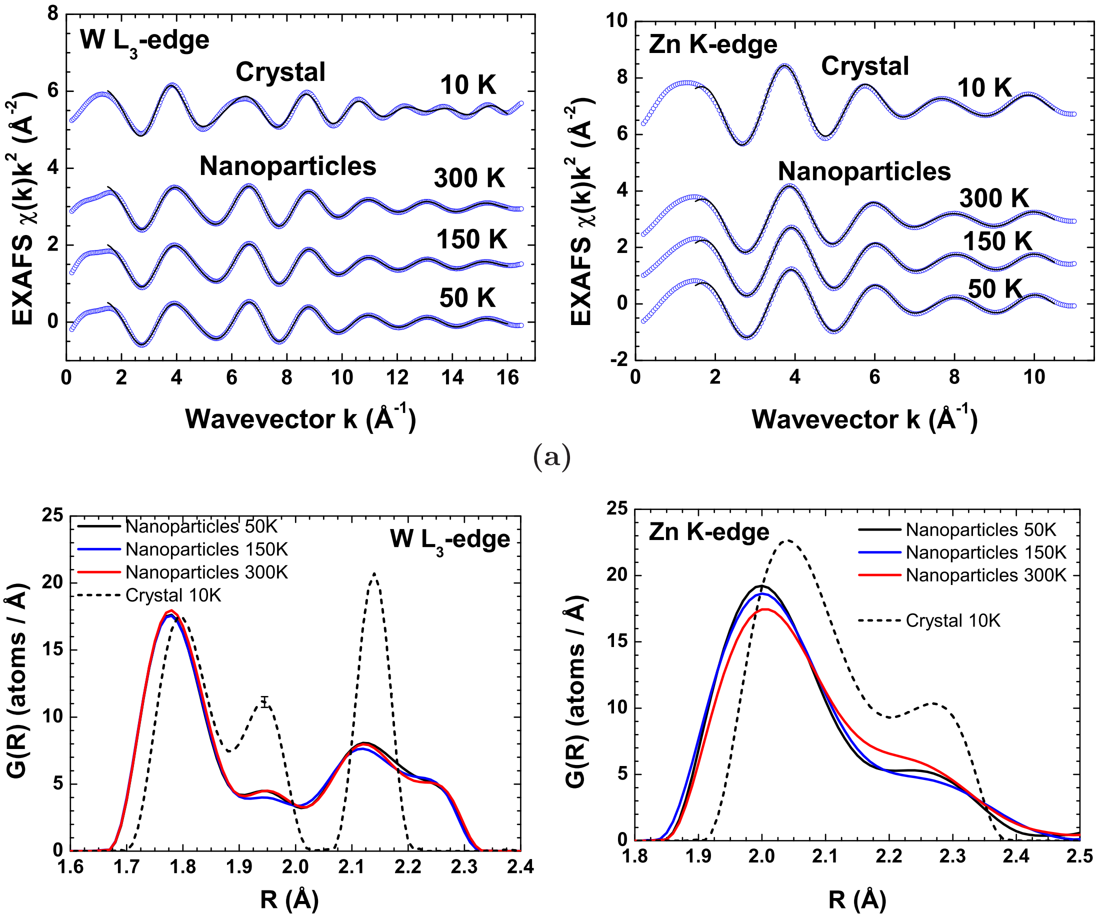

(a)

(b)

Figure 5.7: (a) Best fits (solid lines) of the first coordination shell experimental (open circles) W L_3-edge and Zn K-edge EXAFS signals $\chi(k)k^2$ of nanoparticles and microcrystalline $ZnWO_4$ at different temperatures. (b) The reconstructed RDFs $G(R)$ for the first coordination shell of tungsten and zinc in nanoparticles and microcrystalline $ZnWO_4$ at representative temperatures. See text for details.

The best-fits were performed in the k-space ranges of 1.5-16 Å^{-1} at the W L$_3$-edge and 1.5-10.5 Å^{-1} at the Zn K-edge. The k-space range at the Zn K-edge is shorter due to the close presence of the W L$_3$-edge (Fig. 5.5). The results of the best-fits and corresponding RDFs are shown in Fig. 5.7.

Note very good agreement between the experimental and theoretical first-shell EXAFS signals in Fig. 5.7, and significant difference between distortions of the [WO$_6$] and [ZnO$_6$] octahedra in nanoparticles and microcrystalline ZnWO$_4$ (Fig. 5.7). The RDF for microcrystalline ZnWO$_4$ corresponds well to the crystallographic structure [68, 114, 122], which assumes the existence of three groups of W–O bonds (2×1.79 Å, 2×1.91 Å, and 2×2.13 Å) and Zn–O bonds (at 2×2.03 Å, 2×2.09 Å, and 2×2.23 Å).

The RDFs in nanoparticles show only minor temperature changes, especially around tungsten: this indicates that static disorder dominates the thermal one. Compared to microcrystalline ZnWO$_4$, the RDFs in nanoparticles are broadened, especially at large distances, whereas the first peak is well defined and shifts to shorter distances. This means that both tungsten and zinc atoms make stronger bonds with nearest 2-4 oxygen atoms, whereas remaining oxygen atoms become weakly bound. The total coordination of both tungsten and zinc atoms remains always octahedral. Such behavior of the RDFs confirms strong distortion of the [WO$_6$] and [ZnO$_6$] octahedra in nanoparticles and is also favorable to the formation of the short W=O bonds, observed in the Raman spectrum (Fig. 5.2).

5.1.4 Conclusions

Nanoparticles and microcrystalline ZnWO$_4$ were studied by temperature dependent x-ray absorption spectroscopy at the Zn K and W L$_3$-edges. The obtained results were compared with that determined by complementary experimental techniques as x-ray powder diffraction, Raman and photoluminescence spectroscopies allowing us to probe different aspects of the local atomic and electronic structure.

It was found that the observed changes in the optical properties and lattice dynamics of ZnWO$_4$ nanoparticles cannot be attributed only to the size reduction, but are related to the relaxation of their atomic structure, including formation of surface defects.

The presence of strong structural relaxation in ZnWO$_4$ nanoparticles was confirmed by x-ray absorption spectroscopy study. The independent analysis of the EXAFS signals at the W L$_3$ and Zn K edges by the model-independent approach allowed us to reconstruct the first coordination shell RDFs and to follow their temperature variation. The significant distortions of the [WO_6] and [ZnO_6] octahedra, directly observed in $ZnWO_4$ nanoparticles by EXAFS, show only minor temperature dependence. The distortion results in the shortening of the metal-oxygen (W–O and Zn–O) bonds to the nearest oxygen atoms and the formation of the W=O bonds, whereas the longest bonds are elongated and becomes weaker.

5.2 MD-EXAFS data analysis

5.2.1 Application to ReO_3 crystal

Crystalline ReO_3 has cubic (space group $Pm\bar{3}m$) perovskite-type structure built up of regular [ReO_6] octahedra joined by corners. The structural model and corresponding Brillouin zone are shown in Fig. 5.8. ReO_3 is known as a "covalent metal", having unusually high electrical conductivity, which is close to that of copper or silver. The metallic conductivity is caused by the $Re^{6+}(5d^1)$ delocalized $5d$-electron. Due to the strong covalent bonding between rhenium and oxygen atoms the [ReO_6] octahedra are rather rigid that makes ReO_3 a good candidate to be a negative thermal expansion compound [17].

The ReO_3 powder used in the EXAFS measurements [105] was checked by x-ray diffraction shown in Fig. 5.9. All observable diffraction peaks correspond to the ReO_3 $Pm\bar{3}m$ cubic phase.

The Re L_3-edge EXAFS spectrum of ReO_3 has very strong MS contributions due to the presence in the structure of linear Re–O–Re atomic chains [25, 38, 53, 80, 82, 125]. The origin of the strong MS effects in ReO_3 comes from the role of oxygen atoms increasing the amplitude of the photoelectron wave on the way from and back to the absorbing rhenium atom – the so-called "focusing" effect [38, 80, 125]. However, up to now an account for the MS effects was at best limited to the modelling of the total EXAFS signal by a restricted number of the MS contributions and by treating thermal disorder, given by the EXAFS Debye-Waller factors or MSRD σ^2, as the free model parameters within the harmonic approximation.

In this work the Re L_3-edge EXAFS spectra of ReO_3 were analyzed by the method, based on a combination of molecular dynamics simulation and ab initio EXAFS calculations, that allowed us to accurately account for both the MS contributions and

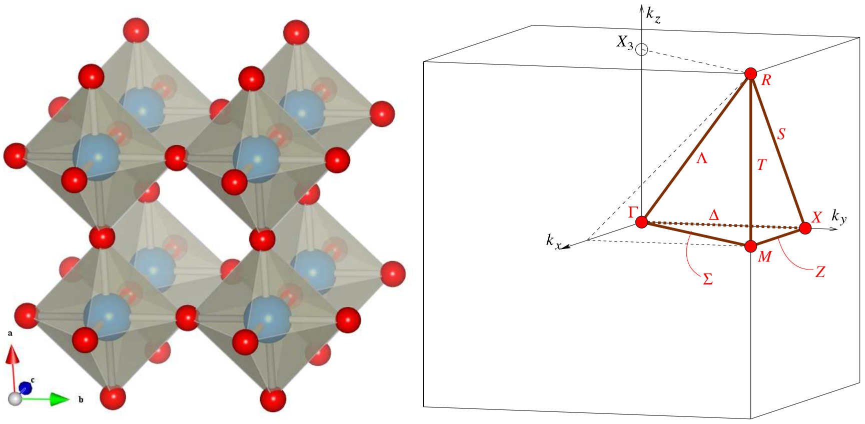

©bilbao crystallographic server
http://www.cryst.ehu.es

Figure 5.8: Crystal structure (left panel) and the first Brillouin zone (right panel) of ReO_3. $[ReO_6]$ octahedra are shown in the left panel. Blue spheres – rhenium atoms, red spheres – oxygen atoms.

thermal disorder. To perform the MD simulations, one needs first to construct the FF model using as much information on the ReO_3 properties as possible.

The structure of ReO_3 is known with high precision from temperature-dependent neutron and x-ray diffraction studies [16, 17, 28]. The values of elastic constants (C_{11}=572 GPa, C_{12}=7 GPa, C_{44}=68 GPa) were also determined by Tsuda et al. [123]. Additionally vibrational frequencies can be used as observables in the FF model construction. The experimental determination of the vibrational frequencies for ReO_3 is a complicated task. The frequencies at the BZ Γ point can be measured by Raman or IR spectroscopies. However, the first-order Raman scattering is forbidden in ReO_3 by cubic symmetry. The IR spectra of metallic ReO_3 were measured by Ishii et al. [56], and two absorption bands were found at 315 cm^{-1} and 905 cm^{-1}. The dispersion of the low-energy phonon modes at room temperature was obtained by the inelastic neutron scattering in [12], but till now the measurement of the high-energy phonon modes remains a challenging task. Therefore, quantum mechanics calculations were used in the present work to determine additional properties of ReO_3 such as the ions charges and the vibrational frequencies at the BZ high symmetry points: they are not know experimentally but are required for the construction of the reliable FF model.

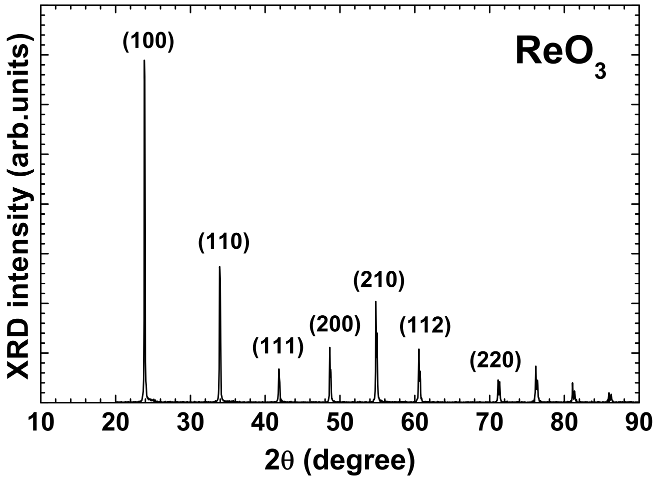

Figure 5.9: X-ray powder diffraction pattern of ReO$_3$ powder. The *hkl* Miller indices are shown for the first seven Bragg peaks.

5.2.1.1 Ab initio LCAO modelling

First-principles periodic LCAO calculations were performed using the CRYSTAL06 code [29]. We used the Hay-Wadt (HW) effective small core potentials (ECP) and the corresponding atomic basis sets for Re atom, excluding diffuse Gaussian type orbitals. The all-electron basis set was used for oxygen atom. Hybrid Hartree-Fock-DFT Hamiltonian B3PW was used in the self-consistent field (SCF) calculations. The details of the geometry optimization and electronic structure calculations can be found in [63]. The ab initio calculations of phonon frequencies were performed by the direct (frozen phonon) method [100] as described in Section 3.3. The values of the phonon frequencies were calculated for several high-symmetry Brillouin zone points in ReO$_3$, performing calculations for the supercells consisting of 8 and 16 primitive cells. In ReO$_3$ the calculated for the symmetry points of BZ frequencies were interpolated over the symmetry directions using FROPHO code by Togo et al. [121]. Fig. 5.10 (upper panel) demonstrates the convergence of the calculated phonon dispersion curves with the supercell size increasing. It was found that 8 and 16 supercell sizes show only minor changes in phonon dispersion curves.

In the simple cubic ReO$_3$ only one lattice parameter (a) is required to describe the structure, and the agreement between its theoretical (3.7424 Å) and experimental (3.7477 Å at T= 2 K [17]) values is better than 0.01 Å.

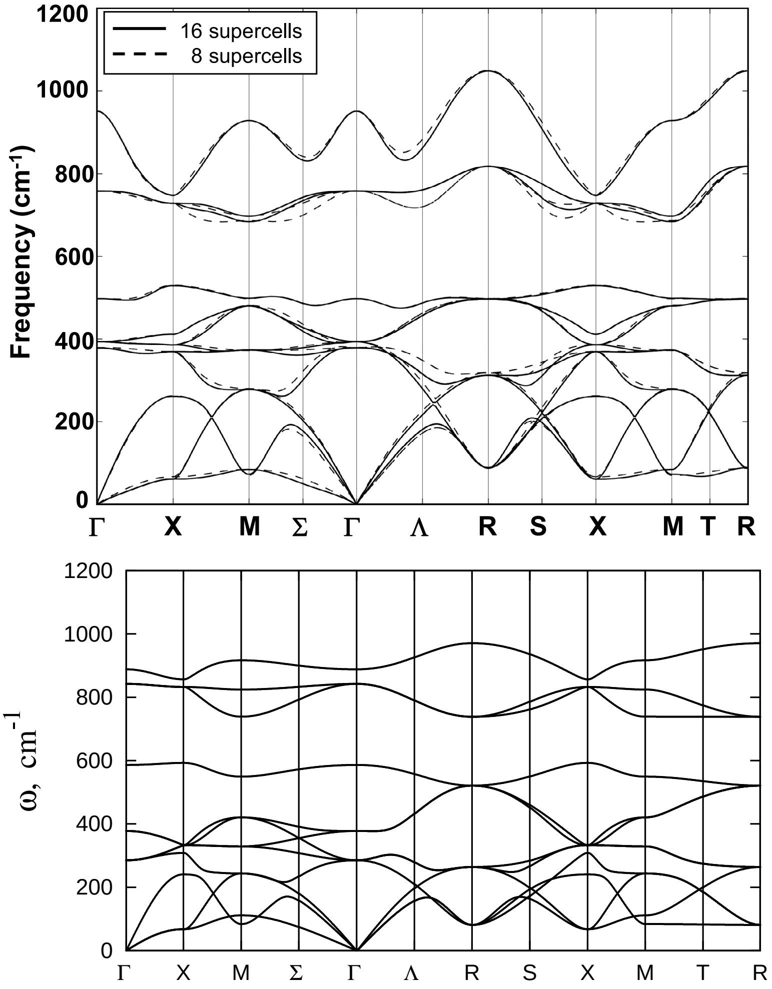

Figure 5.10: Phonon dispersion curves calculated by LCAO (upper panel) and force-field (lower panel) methods.

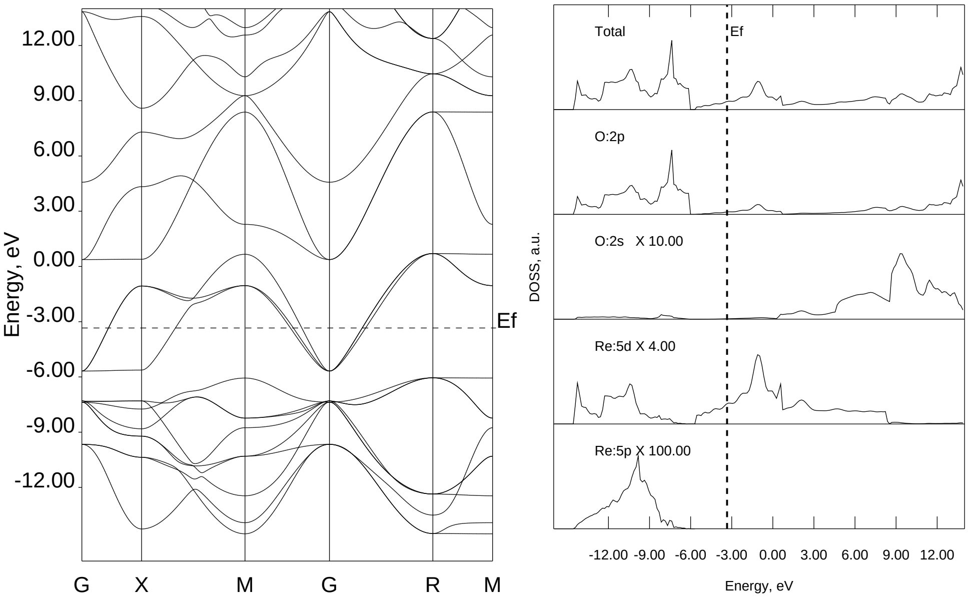

Figure 5.11: Calculated electronic band structure (left panel) and the projected density of electronic states (right panel) for ReO_3.

The electronic band structure and projected density of electronic states for rhenium trioxide are reported in Fig. 5.11. Our calculation correctly predicts that ReO_3 is metallic: the Fermi level is located about 2.3 eV above the bottom of the conduction band, composed mostly of the Re 5d states. The upper part of the valence band in ReO_3 is mainly due to the O 2p states, mixed with the Re 5d states. The partially covalent character of the Re–O bonds is supported by atomic charges Z(Re)=+2.70e and Z(O)=-0.90e, obtained from the Mulliken population analysis.

The isotropic bulk modules B_0 were calculated by varying the lattice constant and fitting the dependence $E(V)$ of a crystal total energy on its volume by a third-order Birch-Murnaghan equation of state. The obtained value for ReO_3 B_0=278 GPa is in agreement with the experimental one B_0=210.8 GPa [123] and other theoretical values from [23] evaluated using the full-potential linear muffin-tin orbital (FP-LMTO) B_0=304 GPa, Hartree-Fock (HF) B_0=282 GPa and HF+correlation B_0=320 GPa methods.

Next the results of phonon calculations, shown in Fig. 5.10, will be discussed. The phonon dispersion curves for ReO_3 were calculated using hybrid Hartree-Fock-DFT Hamiltonian (B3PW) within the frozen-phonon scheme for 8 and 16 supercells to check

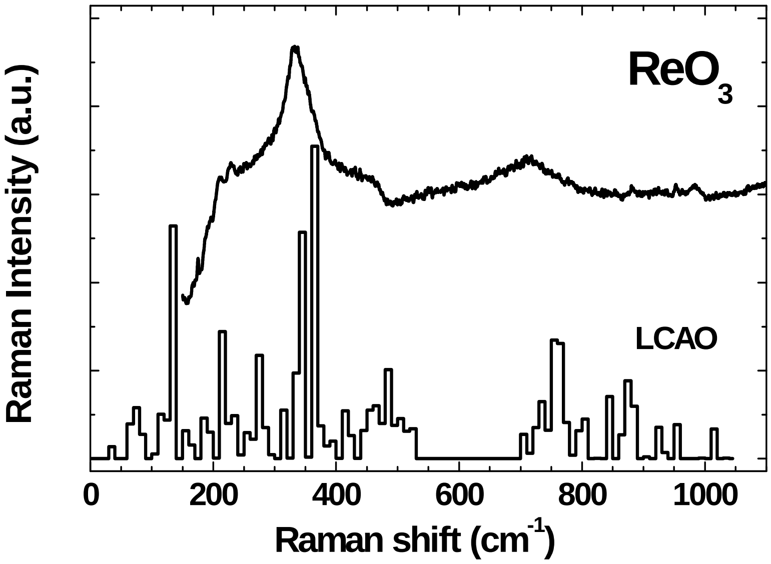

Figure 5.12: A comparison of experimental Raman spectrum for ReO$_3$ taken from [106] and calculated total phonon density of states.

the convergence. Here one expects 12 phonon modes. According to factor group analysis at the BZC (Γ-point), one T$_{1u}$ mode is an acoustic mode, two T$_{1u}$ modes are infrared (IR) active odd (u) optic modes, and one T$_{2u}$ mode is a silent mode. These modes are shown in Fig. 5.10, including the LO-TO splitting. One should note that there is a gap of about 200 cm^{-1} in the phonon density of states (PDOS) separating the upper three optical modes from the other ones.

The absence of even (g) modes Γ-point suggests that no Raman active modes are expected in perfect cubic ReO$_3$. However, the experimental Raman signal was observed in [106] from a single-crystal, polycrystalline powder and thin film ReO$_3$ and associated with the defect-induced Raman scattering. Due to the metallic conductivity of ReO$_3$ the thickness of the sub-surface region probed by the laser is limited. In [106] it was estimated that the scattering occurs within the confined skin layer of 10-20 nm. According to the theory of Raman scattering in nanosystems [42], the phonon confinement should induce the Raman selection rule breaking causing the modes from the whole Brillouin zone contribute into the Raman signal. In 5.12 we compare calculated total PDOS and the Raman spectrum from [106]. The similarity between the shape of the PDOS and the experimental signal supports our interpretation within the framework of the phonon confinement model.

Table 5.1: The parameters of the force-field model for cubic ReO_3.

Coulomb potential			
Atom	Z, e		
Re	3.36		
O	-1.12		

Buckingham potential, cutoff 20 Å			
Pair of atoms	A, eV	ρ, Å	C, eVÅ^2
Re–O	1194.24	0.3426	98.10
O–O	3224.54	0.2652	47.40

Covalent exponential potential, cutoff 2 Å			
Pair of atoms	D	n	r_0, Å
Re–O	4.8283	6.2107	1.875

5.2.1.2 Force-field model

The force-field model was chosen in the form of the Buckingham and covalent exponential interatomic potentials to describe Re–O and O–O bonding (Table 5.1). The model parameters, including atom charges, were optimized using simulated annealing method to reproduce a set of experimental data (lattice parameter [17], elastic constants and bulk modulus [123]) and theoretically calculated phonon frequencies (Fig. 5.10). Thus determined force-field model was further used in the MD simulations.

5.2.1.3 MD-EXAFS modelling

The NVT MD simulations were performed using the GULP3.1 code [40, 41] for a supercell 5×5×5, containing 500 atoms, at temperatures 300 K, 423 K and 573 K. For each temperature, a set of 4000 static atomic configurations was obtained during a simulation run of 20 ps with a time step interval of 0.5 fs. These configurations were further used to calculate the Re L_3- edge EXAFS signals by the ab initio FEFF8 code [10]. The complex exchange-correlation Hedin-Lundqvist potential and default values of muffin-tin radii, as provided within the FEFF8 code [10], were used. Finally, the

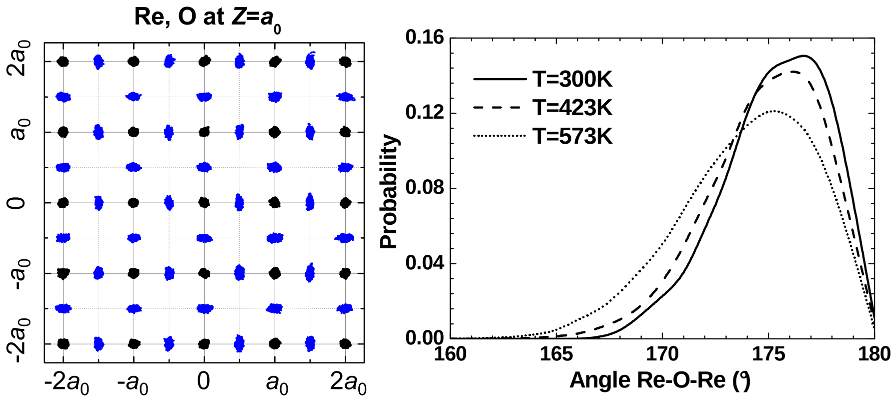

Figure 5.13: (left panel) Representation of MD trajectories at 573 K for Re (black) and O (blue) atoms located in a plane $Z = a_0$ (a_0 is the lattice parameter). (right panel) Distribution of the Re–O–Re angles at 300 K, 423 K and 573 K, calculated from MD simulations.

configuration-averaged EXAFS signals were calculated using (i) single-scattering (SS) and (ii) multiple-scattering (MS) (with paths up to the 8th order) approximations by averaging over all 4000 configurations and compared with the experimental data from [105]. All calculations were performed at the Latvian SuperCluster facility [75].

The perovskite-type ReO_3 structure consists of corner-linked [ReO_6] regular octahedra with Re atoms at the centers and linear Re–O–Re chains. The space between eight octahedra forming the cube is fully vacant that allows for a significant rotation of the [ReO_6] units [17] and results in the anisotropy of oxygen atoms thermal vibration. The obtained MD trajectories in the (100) plane, visualized in Fig. 5.13 for 573 K, confirm that the amplitude of oxygen thermal vibrations is larger in the direction perpendicular to the Re–O–Re chains, but the vibrations of Re atoms are isotropic.

Recent pressure-dependent EXAFS study [53] suggests that even at normal conditions the Re–O–Re bond angle deviates from the linear one, observed by diffraction, and is equal to about 172°. Our temperature dependent MD simulations allowed us to estimate the mean value of the Re–O–Re angle from the angles distributions (Fig. 5.13) to be 174.5° at 300 K, 173.0° at 423 K and 172.2° at 573 K. A decrease of the mean angle value indicates larger amplitude of oxygen vibrations at higher temperatures.

The reliability of our MD simulations is well supported by a good agreement between experimental and theoretical Re L_3-edge EXAFS signals observed in the simulation range up to about 6 Å that includes the first five coordination shells around

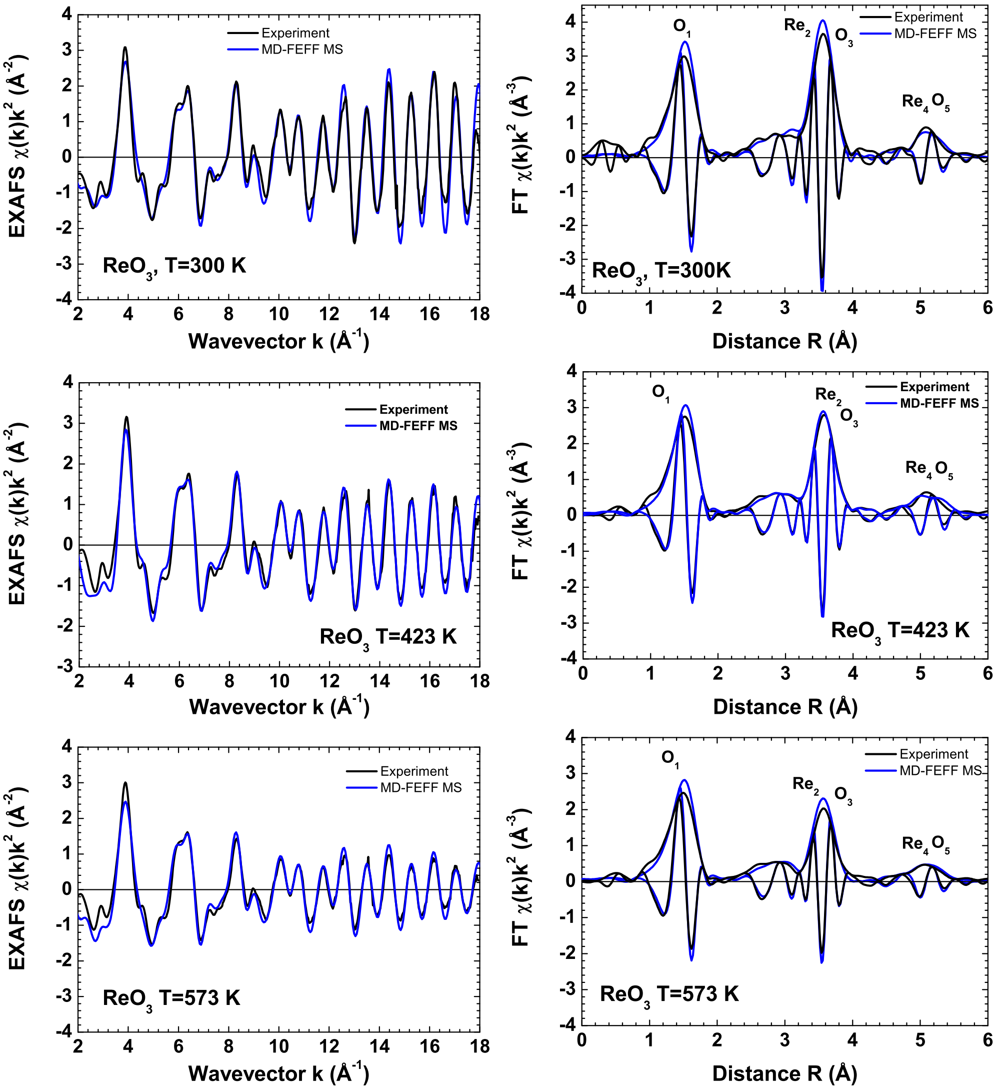

(a) (b)

Figure 5.14: Results of EXAFS modelling using MD-EXAFS method. (a) Re L_3-edge EXAFS signal in ReO_3, (b) FT of the Re L_3-edge EXAFS signal in ReO_3.

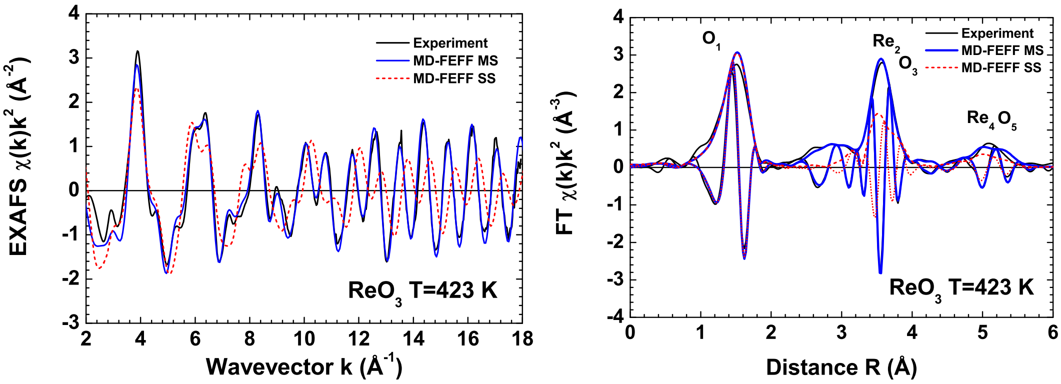

Figure 5.15: Results of the Re L_3-edge EXAFS modelling in ReO_3 using MD-EXAFS method within the SS and MS approximation: (left panel) EXAFS signals and (right panel) corresponding Fourier transforms.

absorbing Re atom. In Fig. 5.14 first row we compare the two EXAFS $\chi(k)k^2$ signals and corresponding Fourier transformations (FTs) at 300 K, 423 K, 573 K. It is clearly seen that EXAFS signal amplitude strongly decreases with temperature increasing. The calculated and experimental signals at all temperatures have excellent matching by phase what indicate on good description of the atomic positions. However amplitude have little mismatch between theory and experiment. This fact indicate on potential model problem in atomic vibrations amplitude description. In the Fig. 5.14 second row FT comparison in shown. The peaks in FT correspond to the coordination shells with admixture of multiple scattering contribution. Again intensity of FT peaks differs, while phase is in good agreement. Note that the amplitude of the last peak at around 5 Å is described well for all temperatures. To confirm the importance of the MS effects in ReO_3 signals within SS and MS approaches were calculated. The SS and MS contributions are shown in Fig. 5.15 and allow us to conclude unambiguously on the origin of the peaks in FTs. As it was suggested before [80], the peak at 2.2-3.0 Å is due to pure MS effects from the first shell, and the MS contributions within the next two main peaks at 3.6 Å and 5.0 Å are about 30-40%.

5.2.1.4 Conclusions

ReO_3 was chosen as an example for the MD-EXAFS method application due to its relatively simple highly-symmetric atomic structure, which is described by only one structural parameter. This allowed us to develop simple force-field model and to use classical molecular dynamics method. Quantum mechanical LCAO calculations were additionally used to determine physical properties of ReO_3, being not available from experiments.

Using the developed force-field model, the MD simulations were performed at three different temperatures. The MD simulation results were used to calculate dynamical properties of ReO_3. In particular, the anisotropy of the oxygen atoms thermal vibrations was confirmed, and the temperature dependence of the ReORe bond angle distribution was determined.

It was shown that the calculated configuration averaged EXAFS signals agree well with the experimental ones at all temperatures. It was also shown that the analysis of the EXAFS signals from the outer coordination shells located at distances larger than 2 Å requires consideration of the MS effects, which overlap strongly with the pair-wise EXAFS contributions.

5.2.2 Application to $CaWO_4$ crystal

Crystalline $CaWO_4$ has tetragonal (space group $I4_1/c$) scheelite-type structure composed of $[WO_4]$ tetrahedra and $[CaO_8]$ polyhedra (Fig. 5.16). $CaWO_4$ is wide band gap isolator with the band gap $E_g = 5.2$ eV [89]. Its Brillouin zone is shown in Fig. 5.16. The $[WO_4]$ tetrahedra can be considered as rigid units with the strong tetrahedral W–O bonds equal to 1.787 Å and the two internal O–W–O angles equal to 107.28° and 113.94° [46]: they remain unchanged within a broad temperature range of 5–1773 K [115]. The presence of the two kinds of internal O–W–O angles reflect the distortion from a regular tetrahedron.

The local atomic structure of $CaWO_4$ was studied by the W L_3-edge EXAFS spectroscopy in [43, 79] within the range of the first coordination shell of tungsten. At the same time, the analysis of the outer shells and the role of the multiple-scattering (MS) effects in the EXAFS spectra were not addressed. In this work, the MD-EXAFS method is used to clarify the contribution of the outer coordination shells and the importance of the MS contributions and of thermal disorder in the W L_3-edge EXAFS spectra of $CaWO_4$.

In Fig. 5.17 x-ray powder diffraction pattern of the commercial $CaWO_4$ powder used in the EXAFS measurements is shown. It confirms the tetragonal (space group $I4_1/c$) $CaWO_4$ phase [115].

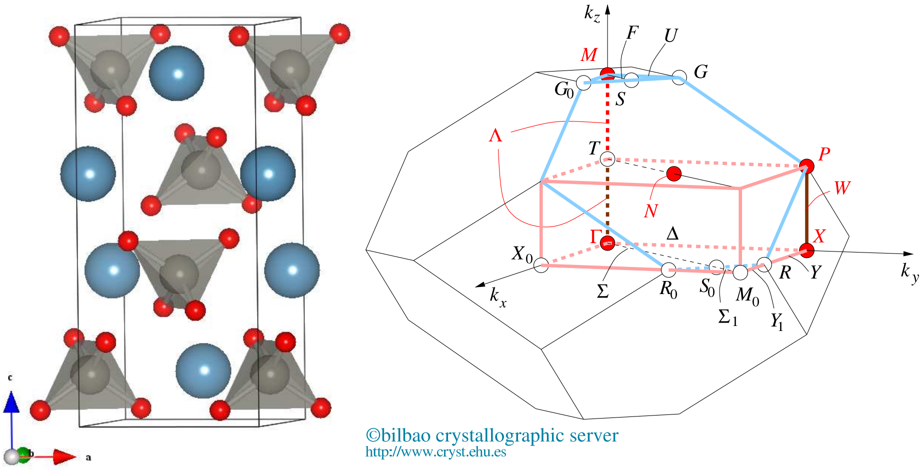
c
b
a
k_z
F
U
M
G_0
S
G
Λ
T
P
W
N
Δ
Γ
X
X_0
k_x
Σ
R_0
S_0
M_0
R
Y
k_y
Σ_1
Y_1

©bilbao crystallographic server
http://www.cryst.ehu.es

Figure 5.16: Crystal structure (left panel) and the first Brillouin zone (right panel) of $CaWO_4$. $[WO_4]$ tetrahedra and Ca atoms are shown in the left panel: red spheres – oxygen atoms, blue spheres – calcium atoms, gray spheres – tungsten atoms.

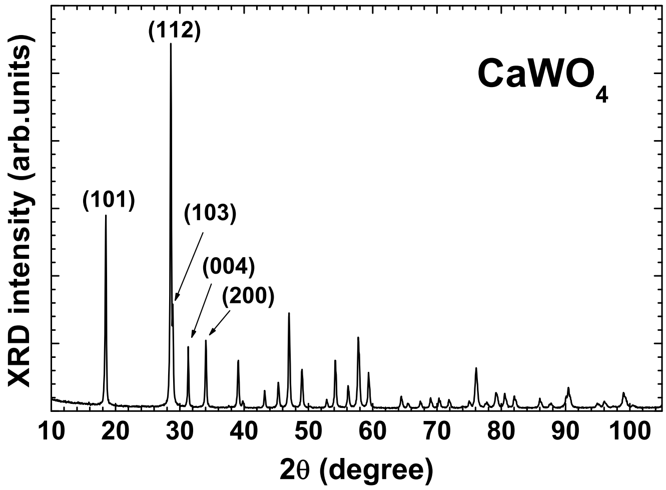

Figure 5.17: X-ray powder diffraction pattern of $CaWO_4$ powder. The *hkl* Miller indices are shown for the first five Bragg peaks.

Table 5.2: Experimental and calculated structural properties of $CaWO_4$.

	Senyshyn model	Cooper model	Shao model	LCAO [31]	Exp. (300 K) [50]
a (Å)	5.250	5.251	5.238	5.266	5.2429
c (Å)	11.37	11.37	11.37	11.41	11.3737
O_x	0.248	0.244	0.241	0.150	0.1507
O_y	0.152	0.144	0.149	0.009	0.0086
O_z	0.082	0.083	0.085	0.210	0.2106
R(W–O) (Å)	1.785	1.731	1.812	1.784	1.78

5.2.2.1 Ab initio LCAO modelling

The electronic structure and properties of tetragonal $CaWO_4$ were calculated using the CRYSTAL06 code [29]. To avoid core electrons of tungsten and calcium atoms, the effective core potentials (ECP) from [47] have been chosen: the small core ECP60 for W (Z=74) atom (60 electrons in the core) and the small core ECP10 for Ca (Z=20) atom (10 electrons in the core). Note that the Hay-Wadt ECP60 [47] has been used to describe the structural and electronic properties of bulk tungsten trioxide WO_3 and to explain the observed instability of cubic WO_3 [22], providing the good agreement between the calculated structural parameters for tetragonal WO_3 and available experimental data. The basis set, optimized in the calculations of the cubic WO_3 crystal [22], was adopted for W atom. The all electron basis set, optimized in earlier calculations of perovskites [103], was used for O atoms.

Experimental and calculated structural properties of $CaWO_4$ are compared in Table 5.2. Five lattice parameters (a, c, O_x, O_y, O_z) are required to describe the structure of tetragonal $CaWO_4$, and the agreement between theoretical and experimental values is better than 0.04 Å.

The electronic band structure and projected density of electronic states (PDOS) for $CaWO_4$ are reported in Fig. 5.18 for hybrid HF-DFT PBE0 Hamiltonian. The calculated band gap is 6.5 eV which is slightly larger than the experimental value of 5.2 eV [89]. For comparison, the band gap values of 4.09 eV [133] and 5.27 eV [98] were

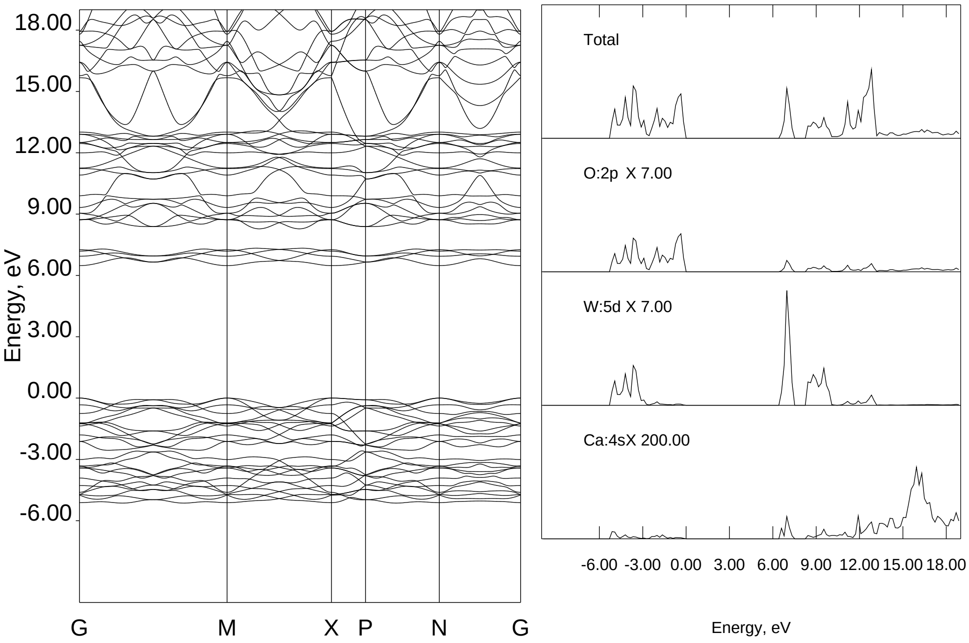

Figure 5.18: Calculated band structure (left panel) and the density of electronic states (DOS) for $CaWO_4$ (right panel).

found for $CaWO_4$ by the linear augmented-plane-wave (LAPW) and the LCAO with B3LYP Hamiltonian methods, respectively.

The energy dispersion curves in Fig. 5.18 are plotted along five different symmetry directions in the first Brillouin zone. The upper part of the valence subband (from -6 eV to 0 eV) is due to mostly O 2*p* states, whereas the lower part is composed mainly of the O 2*p* and W 5*d* states with some admixture of the Ca 4*s* states. The bottom of the conduction band is composed mostly of W 5*d* states. However, an admixture of O 2*p* and some of Ca 4*s* states is clearly observed along the conduction band. The atomic charges in $CaWO_4$ were obtained from the Mulliken population analysis: Z(Ca)=+1.75e, Z(W)=+2.89e, Z(O)=-1.16e.

The phonon calculations for $CaWO_4$ were performed by the direct (frozen phonon) method [100] as described in Section 3.3. The calculations were limited to the Brillouin zone center (Γ-point), for which a group theoretical analysis predicts 26 lattice modes [104]: $3A_g + 5A_u + 5B_g + 3B_u + 5E_g + 5E_u$ from which the 13 even (g) modes ($3A_g + 5B_g + 5E_g$) are Raman active, the 10 odd (u) modes ($5A_u + 5E_u$) are IR active and three odd modes ($3B_u$) are silent. The calculated frequencies were indexed

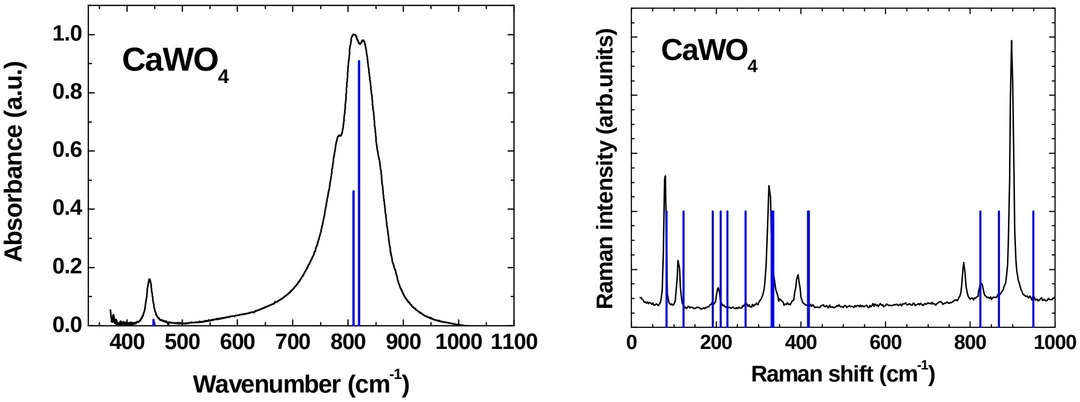

Figure 5.19: (left panel) Infra-red (IR) spectrum of $CaWO_4$ and calculated IR-active vibrational modes (blue vertical lines). The height of the lines indicates the calculated IR mode intensity. (right panel) Raman spectrum of $CaWO_4$ and calculated Raman-active vibrational modes (vertical lines).

as infrared and Raman active modes and are compared with the experimental signals in Fig. 5.19. Note that the intensity of infrared active modes was also calculated. Both infrared and Raman phonon bands are qualitatively well reproduced, but the quantitative agreement is better for infrared signals. In Raman spectra the theory tends to overestimate the phonon frequencies, especially, at high energies. However, the largest observed difference is below 50 cm^{-1}.

5.2.2.2 Force-field model

Three force-field (FF) models have been developed for $CaWO_4$ in the past to describe different properties of bulk crystal (Senyshyn model) [116], intrinsic defects (Shao model) [117] and crystal surfaces (Cooper model) [21]. The three models consist of the pairwise potentials, and the three body interaction is additionally introduced in the Senyshyn [116] and Cooper [21] models. Note that the three body potential is required to stabilize [WO_4] tetrahedra in the MD simulations. The shell model is also used for oxygen atoms in the Cooper model, but the Shao model contains the shell model for all atoms. Also in Senyshyn and Cooper models atomic charges were taken from the DFT calculations, whereas Shao et al. [117] used formal charges 2+ for Ca atom, 6+ for W atom and 2- for O atom.

The shell model describes polarizability effect, which we do not expect to produce a considerable effect in the molecular dynamics simulations. Therefore, the shell part was removed from the force-field, and the potential parameters were re-optimized for Shao and Cooper models. In the case of the Cooper model, the Ca–O and W–O parameters were re-optimized, and good agreement of structural and elastic properties was obtained. However, this was not the case for the Shao model, so it was excluded from the further analysis.

To conclude, the two FF models, that of Senyshyn (Table 5.3) and re-optimized Cooper (Table 5.3), were chosen for further MD-EXAFS simulations.

5.2.2.3 MD-EXAFS modelling

The selected force field models were further used in the MD simulations. The NVT MD simulations were performed using GULP3.1 code [40, 41] for a supercell 3x3x2, containing 216 atoms, at temperatures 300 K. A set of 4000 static atomic configurations was obtained during a simulation run of 20 ps with a time step interval of 0.5 fs. These configurations were further used to calculate the W L_3-edge EXAFS signals by the ab initio FEFF8 code [10]. The complex exchange-correlation Hedin-Lundqvist potential and default values of muffin-tin radii, as provided within the FEFF8 code [10], were used.

In Fig. 5.20 the radial distribution functions (RDFs) for tungsten atoms obtained from the MD simulations using the two FF models are shown. The RDFs obtained by both models are close with some difference in the first coordination shell of tungsten and minor differences in the outer shells at distances larger than 2.5 Å. In particular, the Cooper model gives narrower distribution of the first-shell W–O distances (the peak at ∼1.8 Å).

To identify which from the two models is best in the description of the EXAFS spectra, the calculated configuration averaged EXAFS signals are compared with the experimental one in Fig. 5.21. It is clearly seen that the Senyshyn FF model gives better agreement. The phase and amplitude matching is good at all k-values. In the case of the Cooper model, the phase and amplitude of the calculated EXAFS signal deviates clearly from the experimental one at high-k values. These results indicate that the Cooper model gives shorter W–O distances and slightly underestimates thermal disorder.

Table 5.3: Parameters of the Senyshyn [116] and Cooper [21] force-field models for $CaWO_4$. The Cooper model has re-optimized W–O and Ca–O Buckingham pair potentials.

	Senyshyn's FF model			Cooper's FF model		
			Coulomb potential			
Atom		Z, e			Z, e	
W		1.68			2.18	
O		-0.92			-1.045	
Ca		2.00			2.00	
			Buckingham potential, cutoff 14 Å			
Pair of atoms	A, eV	ρ, Å	C, eV Å^2	A, eV	ρ, Å	C, eV Å^2
Ca–O	2312	0.2812	0.0	1841.26	0.2925	0.0
O–O	2023	0.2674	13.83	16372	0.2130	3.47
W–O				114.36	0.4387	0.0
			Morse potential, cutoff 2 Å			
Pair of atoms	D_e, eV	a_m Å^{-2}	r_0, Å	D, eV	a_m Å^{-2}	r_0, Å
W–O	1.501	2.671	1.8928	6.96	1.82	1.78
			Three-body potential, cutoff 2 Å			
Pair of atoms	k, eV rad^{-2}	θ_0, deg		k, eV rad^{-2}	θ_0, deg	
O–W–O	2.6071	110.524		1.9670	109.5	

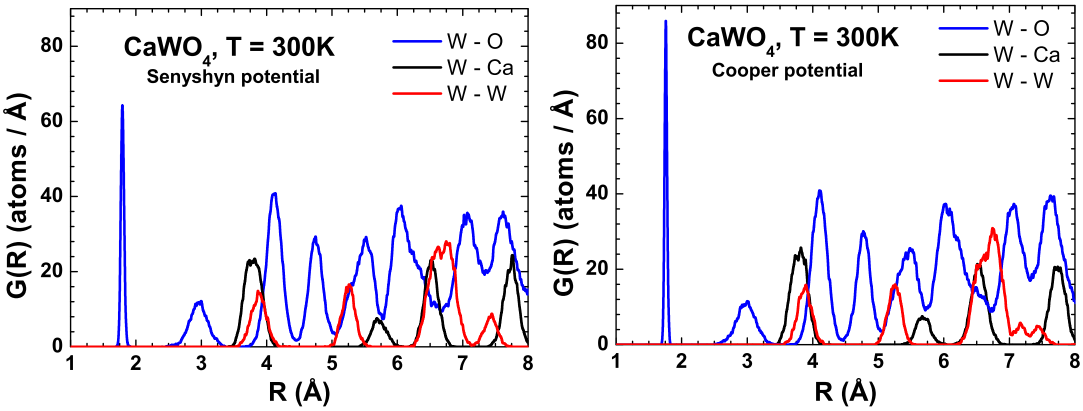

Figure 5.20: Radial distribution functions (RDFs) W–O, W–Ca and W–W for $CaWO_4$ obtained from the MD simulations using the Senyshyn (left panel) [116] and Cooper (right panel) [21] force-field models.

Further we will discuss only the results of the Senyshyn model. For this model the influence of the MS contributions is estimated in Fig. 5.21, where the configuration averaged EXAFS signals, calculated within the SS and MS approximations, are shown. Note that the MS EXAFS signal includes both SS and high-order scattering contributions. It is found that the MS contributions in $CaWO_4$ are relatively small and give EXAFS signal amplitude reduction of about 10% for the peak in FT at 3.5 Å. This fact can be attributed to the absence in $CaWO_4$ of the near linear atomic chains, which are normally responsible for the strong MS contributions as, for example, in ReO_3.

Because of rather good agreement between calculated and experimental spectra, the accurate analysis of the second and further coordination shells can be reliably performed. To identify the origin of peaks in FT, the separate EXAFS signals, corresponding to different groups of atoms, were calculated. To do that each peak in the RDF till 6 Å (Fig. 5.20) was approximated by the Gaussian function, which depends on three parameters – peak position, amplitude and width. Such decomposition is rather simple to do, because peaks corresponding to the group of atoms either do not overlap or overlap little. Using thus obtained parameters, the EXAFS signal was calculated using the conventional EXAFS formula (Eq. 2.11).

The calculated separate EXAFS signals are shown in Fig. 5.22(upper panel). The major contribution comes from the nearest oxygens located in the first coordination shell, while the other signals are noticeably smaller. In Fig. 5.22 the lower panel shows

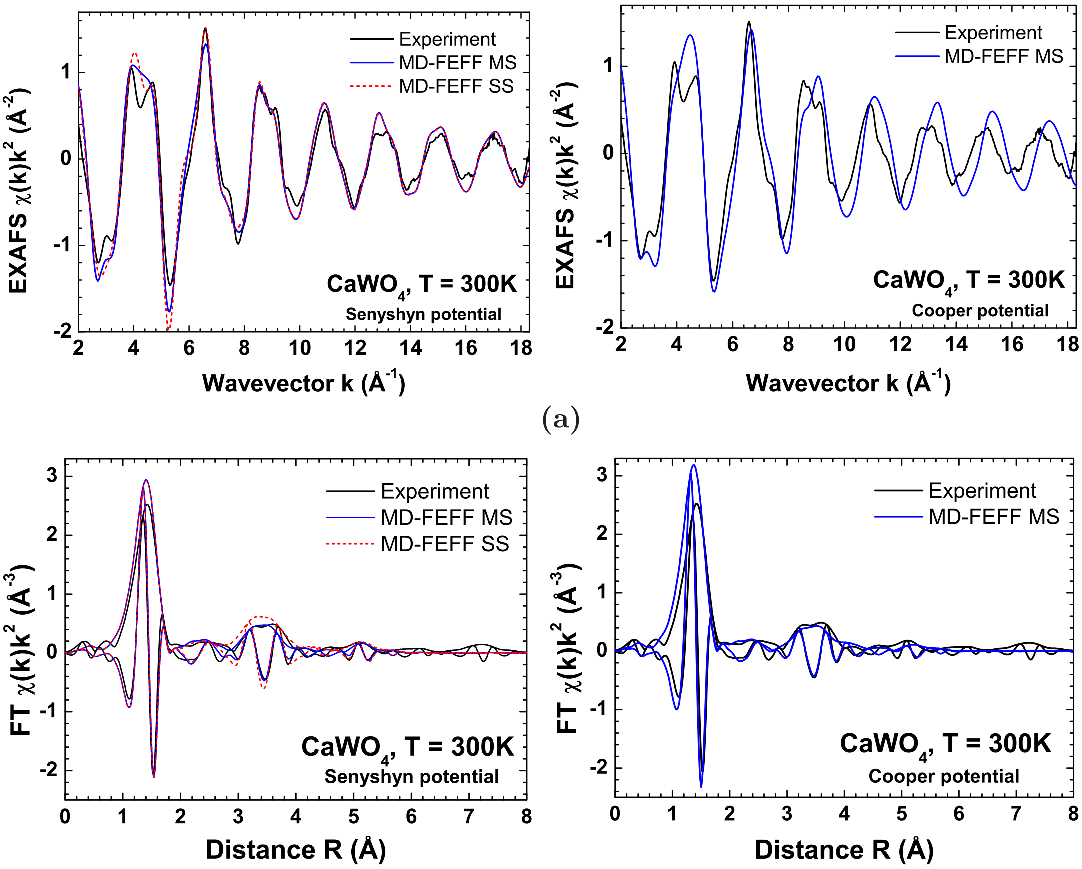

(a)

(b)

Figure 5.21: Results of EXAFS modelling using MD-EXAFS method for Senyshyn (left column) and re-optimized Cooper (right column) force-field potential models. (a) W L_3-edge EXAFS signal in $CaWO_4$, (b) FT of the W L_3-edge EXAFS signal in $CaWO_4$. The configuration averaged EXAFS signals containing only SS (MD-FEFF SS) or all MS (MD-FEFF MS) contributions are shown.

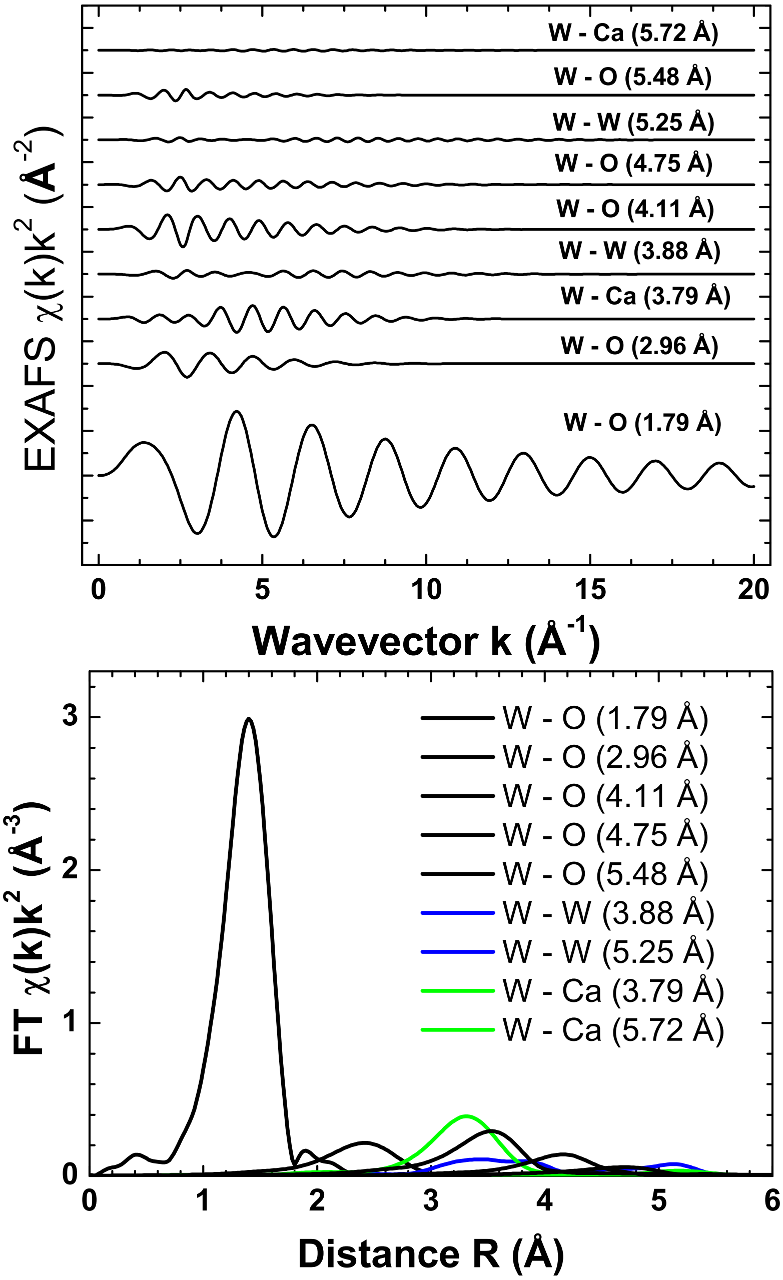

Figure 5.22: The W L_3-edge EXAFS $\chi(k)k^2$ components for $CaWO_4$ in the single-scattering approximation and their Fourier transforms (FTs) corresponding to the atomic groups at different distances from the absorbing tungsten atom.

the corresponding FTs. This helps to understand the origin of any particular peak. The peak at 2.4 Å is from oxygen group located at 2.96 Å. the broad peak at 3.5 Å consists have three contributions from Ca atoms at 3.79 Å, O atoms at 4.11 Å and W atoms at 3.88 Å. Further one more peak from O atoms located at 4.75 Å is visible. Influence from more distant atoms can be neglected.

5.2.2.4 Conclusions

Ab initio calculations of the structural and electronic properties of scheelite-type $CaWO_4$ crystal have been performed within the periodic LCAO method using hybrid Hartree-Fock–DFT theory. The obtained results are in good agreement with known experimental data, including vibrational properties probed by Raman and infra-red spectroscopies. The QM calculations were also used to obtain charges on atoms.

The two force-field models [21, 116] were used in the MD simulations performed at 300 K. The Cooper model [21] was re-optimized to provide the difference between experimental and calculated structural parameters of about ±0.01 Å. As a result of the MD simulations, both models gave similar RDF functions. However, the comparison of the configuration averaged EXAFS signals with the experimental W L_3-edge EXAFS spectrum allows us to conclude for benefit of the Senyshyn FF model. Therefore, it was finally used to study the influence of the MS effects on the EXAFS signal.

It was found that the MS contributions have minor influence on the W L_3-edge EXAFS signal in $CaWO_4$. The main part of the EXAFS signal comes from oxygen atoms in the first coordination shell. Besides, there is also noticeable contributions from the outer group of oxygen atoms located till 5 Å and from Ca atoms at 3.79 Å. The contribution from the heavy tungsten atoms, located at about 3.88 Å is surprisingly small due to the thermal disorder.

5.2.3 Application to $ZnWO_4$ crystal

Crystalline $ZnWO_4$ has monoclinic (space group $P2/c$) wolframite-type structure made by $[WO_6]$ and $[ZnO_6]$ octahedra joined by edges into infinite zigzag chains, consisting of octahedral units of the same type and running parallel to c-axis (Fig. 5.23). The first Brillouin zone of $ZnWO_4$ is shown in Fig. 5.23. There are two formula units per primitive cell, having the lattice parameters a=4.6902 Å, b=5.7169 Å, c=4.9268 Å and β=90.626° [122]. The presence of two non-equivalent oxygen atoms is responsible for

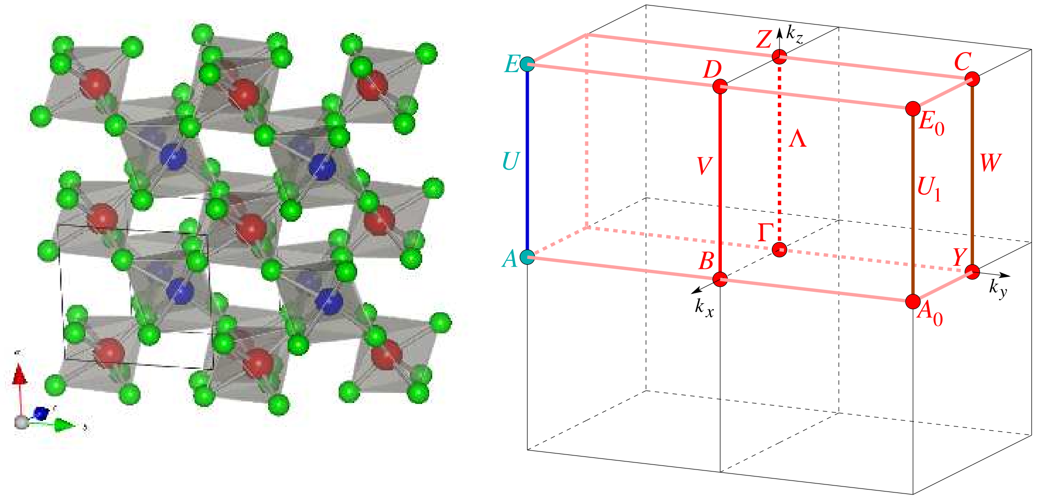

©bilbao crystallographic server
http://www.cryst.ehu.es

Figure 5.23: Crystal structure (left panel) and the first Brillouin zone (right panel) of $ZnWO_4$. $[WO_6]$ and $[ZnO_6]$ octahedra are shown in the left panel. Red spheres – zinc atoms, blue spheres – tungsten atoms, green spheres – oxygen atoms.

three pairs of Zn–O and W–O bonds, having different lengths. The $[WO_6]$ octahedra distortion has been directly observed by the W L_3-edge x-ray absorption spectroscopy in [113]. In this work both Zn K and W L_3 edges were measured and analyzed in $ZnWO_4$ by the MD-EXAFS approach.

5.2.3.1 Ab initio LCAO modelling

The electronic structure and properties of monoclinic $ZnWO_4$ were calculated using the CRYSTAL06 code [29]. To avoid core electrons of tungsten and zinc atoms, the effective core potentials (ECP) from [47, 48, 49, 55] have been chosen: the small core ECP60 for W (Z=74) atom (60 electrons in the core) and the small core ECP18 for Zn (Z=30) atom (18 electrons in the core). Note that the Hay-Wadt ECP60 [47] has been used to describe the structural and electronic properties of bulk tungsten trioxide WO_3 and to explain the observed instability of cubic WO_3 [22], providing the good agreement between the calculated structural parameters for tetragonal WO_3 and available experimental data. The use of ECP18 allows us to include Zn 3d-electrons in the valence shell, which is known to be important for the transition metal compounds. The basis set [55], corresponding to ECP18 pseudopotential, was chosen for Zn atom, and the diffuse Gaussian type orbitals with exponents less than 0.06 were excluded to avoid the basis set linear dependence. The basis set, optimized in the calculations of the cubic WO_3 crystal [22], was adopted for W atom. The all electron basis set, optimized in earlier calculations of perovskites [103], was used for O atoms.

In the CRYSTAL06 code, the accuracy in the evaluation of the Coulomb and exchange series is controlled by a set of tolerances, which were taken to be the default values (6, 6, 6, 6, 12). The Monkhorst-Pack scheme [90] for 8×8×8 k-point mesh in the Brillouin zone was applied. The total spin projection S_z=0 was fixed in the calculation of the closed shell ground state of insulating $ZnWO_4$ crystal. The SCF calculations were performed for hybrid HF-DFT PBE0 [6] Hamiltonian. The choice of the Hamiltonian was based on previous calculations [63].

The calculated structural parameters are compared with experimentally determined ones in Table 5.4.

The calculated energy dispersion curves and projected density of electronic states for hybrid HF-DFT PBE0 Hamiltonian are shown in Fig. 5.24. The dispersion curves are plotted along eight different symmetry directions in the first Brillouin zone. The narrow subband, observed at about -9 eV, corresponds to the Zn 3d states and is well separated from other bands. The upper part of the valence subband (-7.5-0 eV) is due to mostly O 2p states, mixed with W 5d states, whereas the lower part is composed of the O 2p, W 5d with some admixture of Zn 4s states. The highest state in the valence band is located at the B point, while the states at Y and A points are very close in the energy values. The bottom of the conduction band is composed mostly of W 5d states. However, an admixture of O 2p and some of Zn 4s states is clearly observed along the conduction band. The lowest energy state in the conduction band is located at Y point of the Brillouin zone.

To conclude, the minimum band gap for PBE0 Hamiltonian occurs at Y point of the Brillouin zone and corresponds to a direct transition. The calculated band gap value E_g=5.4 eV is in good agreement with the experimental values of 4.6 eV [67] and 4.9 eV [57]. The atomic charges were obtained from Mulliken population analysis and are equal to Z(Zn)=+1.54e, Z(W)=+2.76e, Z(O1)=-1.13e and Z(O2)=-1.02e. The atomic charge values suggest partially covalent W–O bonding.

In Fig. 5.25 the comparison between XPS spectra [57] and calculated projected density of states (PDOS) curves is shown. The binding energy of PDOS curves is given relative to the Fermi level placed at the top of the calculated valence band. The energy

Table 5.4: Experimental and calculated structural properties of $ZnWO_4$.

	Model1	Model2	Model3	LCAO PBE0 [31]	Exp. (300 K) [122]
a (Å)	4.701	4.669	4.692	4.684	4.6902
b (Å)	5.708	5.706	5.709	5.709	5.7169
c (Å)	4.937	4.973	4.946	4.930	4.9268
β ($\circ$)	90.60	90.60	90.60	90.70	90.626
Zn_y	0.681	0.669	0.673	0.677	0.6838
W_y	0.174	0.180	0.177	0.181	0.1820
$O1_x$	0.214	0.214	0.206	0.215	0.2171
$O1_y$	0.897	0.880	0.901	0.895	0.8953
$O1_z$	0.408	0.441	0.441	0.437	0.4373
$O2_x$	0.253	0.249	0.252	0.256	0.2557
$O2_y$	0.369	0.365	0.379	0.375	0.3751
$O2_z$	0.406	0.399	0.404	0.402	0.3999
R(W–O2) (Å)	1.785	1.731	1.812	1.790	1.784
R(W–O1) (Å)	2.020	1.871	1.872	1.903	1.908
R(W–O1) (Å)	2.042	2.198	2.072	2.123	2.134
R(Zn–O1) (Å)	1.988	2.039	2.080	2.052	2.027
R(Zn–O2) (Å)	2.067	2.101	2.124	2.071	2.087
R(Zn–O2) (Å)	2.266	2.225	2.187	2.205	2.232
	Elastic constants (GPa)				
	Model1	Model2	Model3		Experiment [102]
C_{11}	238	238	249		240.23
C_{22}	216	212	209		214.93
C_{33}	289	292	280		287.96
C_{44}	126	64	-19		69.65
C_{55}	139	102	75		70.01
C_{66}	88	62	42		24.93
C_{12}	141	79	91		108.94
C_{13}	171	106	124		102.21
C_{23}	106	116	136		112.99

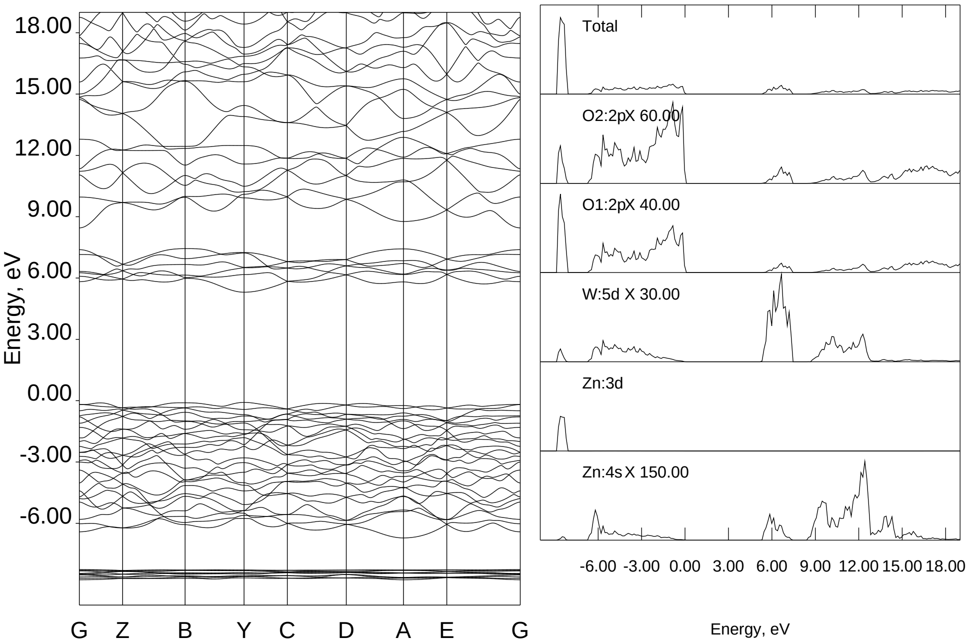

Figure 5.24: Calculated band structure (left panel) and projected density of electronic states (right panel) for $ZnWO_4$.

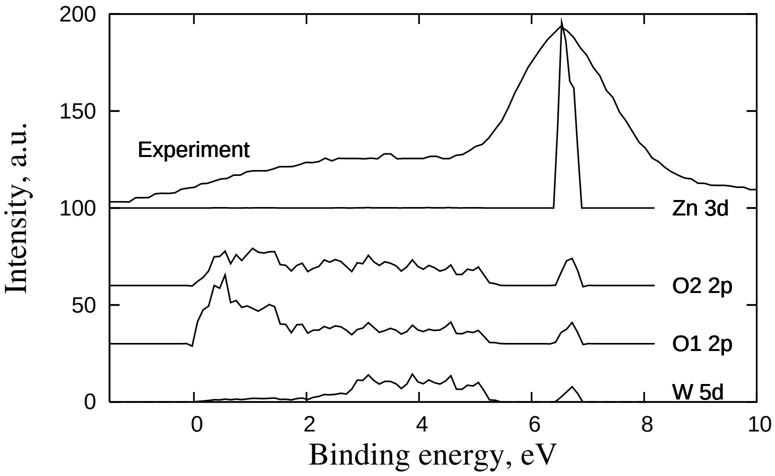

Figure 5.25: Comparison of XPS spectrum from [57] and projected DOS curves for wolframite-type $ZnWO_4$. Curves are vertically shifted for clarity.

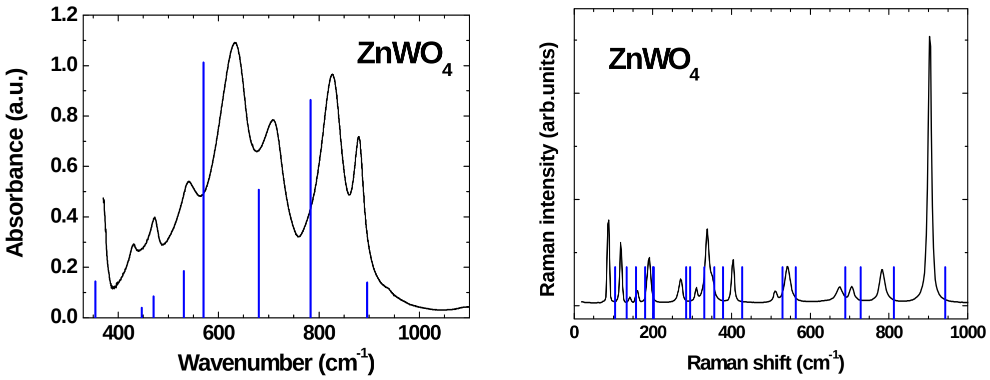

Figure 5.26: Experimental infrared (left panel) and Raman (right panel) spectra in polycrystalline $ZnWO_4$. The positions of the LCAO calculated bands are shown by vertical lines.

scale of the XPS spectrum has been modified for the best agreement of the main sharp peak in the experimental signal with the Zn 3d PDOS position. The low binding energy broad peak of the XPS spectrum is attributed to the O 2p states, with some admixture of the W 5d states. The overall agreement between calculated splitting of the O 2p states and Zn 3d states and the two peaks in the XPS spectrum is very good, being better than that found previously within the cluster DV-Xα method [57].

The phonon calculations for $ZnWO_4$ were also performed by the direct (frozen phonon) method [100] as described in Section 3.3. The calculated frequencies at the BZ center (Γ-point) were indexed as 18 infrared and 18 Raman active modes. They are compared with the experimental signals in Fig. 5.26. Note that the intensity of infrared active modes was also calculated. Both infrared and Raman phonon bands are qualitatively well reproduced, but the quantitative agreement is better for infrared signals. In Raman spectra the theory tends to overestimate the phonon frequencies, especially, at high energies. However, the largest observed difference is below 50 cm^{-1}.

5.2.3.2 Force-field model

The main challenge in modeling $ZnWO_4$ crystal is a description of the [WO_6] and [ZnO_6] octahedra distortion, which results in three different distances of W–O and Zn–O bonds. Therefore, three FF models of different complexity were developed giving reasonably good agreement for equilibrium structural parameters compared to that

Table 5.5: The parameters of the first (Model1) force-field model.

Coulomb potential

Atom	Z, e
Zn	2.0
W	3.505
O1	-1.37625
O2	-1.37625

Buckingham potential

Pair of atoms	A, eV	ρ, Å	C, eV Å^2	R_{min}^{cutoff}, Å	R_{min}^{cutoff}, Å
Zn–O1	910.04	0.2886	0.0	0.0	12.0
Zn–O2	823.20	0.3071	0.0	0.0	12.0
O–O	1458.47	0.3169	0.2429	0.0	12.0

Morse potential

Pair of atoms	D_e, eV	a_m, Å^{-2}	θ_0, deg	R_{min}^{cutoff}, Å	R_{min}^{cutoff}, Å
W–O1	3.856	2.0090	2.13	0.0	12.0
W–O2	2.142	2.9558	1.95	0.0	12.0

found experimentally and by quantum mechanical calculations (Table 5.4). The elastic constant values are also in agreement with the experimental ones.

In the first model, called as 'Model1' (Table 5.5), the charges for both oxygen atoms were equal. The pair potentials in the Buckingham form were chosen for Zn–O1, Zn–O2 and O–O atom pairs, while the Morse-type potentials were chosen for W–O1 and W–O2 atom pairs.

In the second model, called as 'Model2' (Table 5.6), the atomic charges were taken from LCAO calculations and different charges were set to non-equivalent oxygens. The pair potentials were chosen in the Buckingham form. Here two potentials defined at different intervals of distances were used for single atomic pair.

The third model, called as 'Model3' (Table 5.6) is based on Model2, but the O–O interactions are separated into three interactions O1–O1, O2–O2, O1–O2.

Table 5.6: The parameters of the second (Model2) and third (Model3) force-field models.

	Coulomb potential				
Atom	Z, e				
Zn	1.54				
W	2.76				
O1	-1.13				
O2	-1.02				
	Model2 Buckingham potential				
Pair of atoms	A, eV	ρ, Å	C, eV Å^2	R_{min}^{cutoff}, Å	R_{max}^{cutoff}, Å
W–O1	550.71	0.3129	0.0	0.0	3.0
W–O1	11816.46	0.0273	0.0	3.0	12.0
W–O2	158786.57	0.1430	0.0	0.0	3.0
W–O2	47399.88	0.2481	0.0	3.0	12.0
Zn–O1	199602.56	0.1515	0.0	0.0	3.0
Zn–O1	40688.13	0.0111	0.0	3.0	10.0
Zn–O2	22117.06	0.1847	0.0	0.0	3.0
Zn–O2	40688.13	0.0111	0.0	3.0	10.0
O–O	60313.99	0.2108	32.0	0.0	12.0
	Model3 Buckingham potential				
W–O1	379.11687	0.341817	0.0	0.0	3.0
W–O1	66937.283	0.259746	0.0	3.0	12.0
W–O2	162314.37	0.147926	0.0	0.0	3.0
W–O2	805385.16	0.171120	0.0	3.0	12.0
Zn–O1	1306138.8	0.134285	0.0	0.0	3.0
Zn–O1	438.24129	0.099791	0.0	3.0	10.0
Zn–O2	6625.9031	0.206840	0.0	0.0	3.0
Zn–O2	1654.2710	0.106498	0.0	3.0	10.0
O1–O1	38644262.0	0.122710	32.0	0.0	4.0
O2–O2	16566379.0	0.146430	32.0	0.0	4.0
O1–O2	1437.5166	0.314020	32.0	0.0	4.0

5.2.3.3 MD-EXAFS modelling

The three force-field models (Tables 5.5 and 5.6) were used in the MD simulations. The NVT MD simulations were performed using GULP3.1 code [40, 41] for a supercell 5×5×5, containing 1500 atoms, at temperatures 300 K. A set of 4000 static atomic configurations was obtained during a simulation run of 20 ps with a time step interval of 0.5 fs. These configurations were further used to calculate the W L_3-edge EXAFS signals by the ab initio FEFF8.2 code [10]. The complex exchange-correlation Hedin-Lundqvist potential and default values of muffin-tin radii, as provided within the FEFF8.2 code [10], were used. Finally, the configuration-averaged EXAFS signals were calculated using multiple-scattering (MS) (with paths up to the 8th order) approximation by averaging over all 4000 configurations and compared with the experimental Zn K and W L_3 edges EXAFS data.

In Fig. 5.27 the radial distribution functions (RDFs) for tungsten atoms obtained from the MD simulations using the three FF models are shown. The first model Model1 strongly differs from the two others. There is a mismatch of lengths distribution for W–O bond in the first coordination shell of tungsten. The diffraction measurements suggest the presence of three different W–O bond lengths, which can be divided into four nearest (∼1.78 Å and ∼1.90 Å) and two distant (∼2.13 Å) bonds. On the contrary, the Model1 shows opposite distribution with two nearest and four distant oxygen atoms.

Two other models correctly predict the distribution of oxygen atoms within the first coordination shell for both W and Zn atoms. The distribution of atoms in the outer coordination shells is broadened due to low symmetry of $ZnWO_4$ crystal. Therefore to check the MD simulation results, the configurational averaged EXAFS signals were calculated for the three models.

In Fig. 5.28 the comparison of calculated configurational averaged EXAFS signals with the experimental ones is shown for the two edges. As expected, for the Model1 the W L_3-edge EXAFS signal deviates significantly from the experimental one and its Fourier transform clearly shows the problem in the first coordination shell. The Zn K-edge EXAFS signal also differs strongly from the experimental one, however as it is seen from FT, the first coordination shell is correctly reproduced, while the outer shells differ. The two other models, Model2 and Model3, give better agreement with the experimental EXAFS spectrum at both edges, however the agreement is not so good as

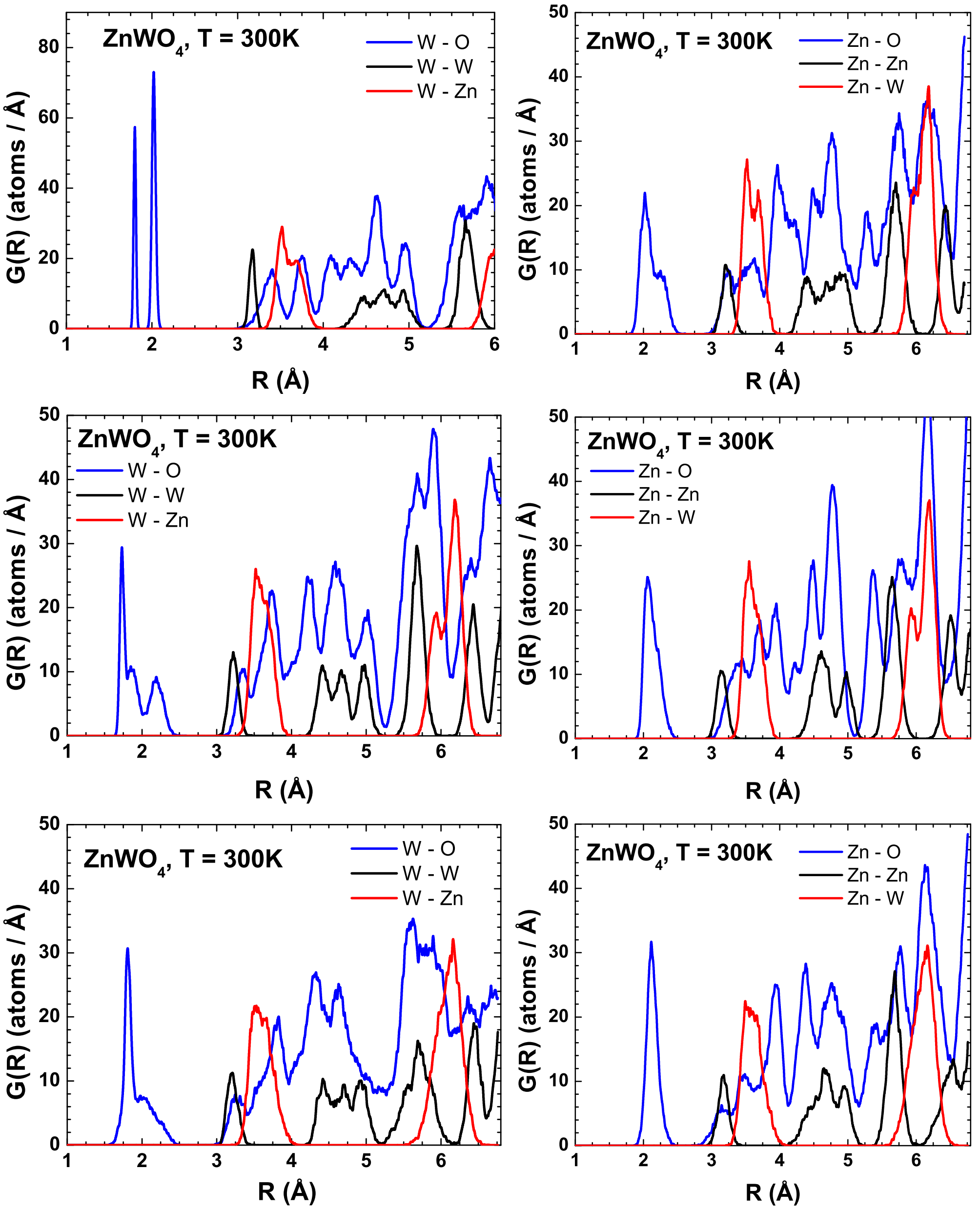

(a) (b)

Figure 5.27: Radial distribution functions (RDF) for W (a) and Zn (b) atoms obtained from the MD simulation results for Model1 – upper row, Model2 – middle row, Model3 – lower row.

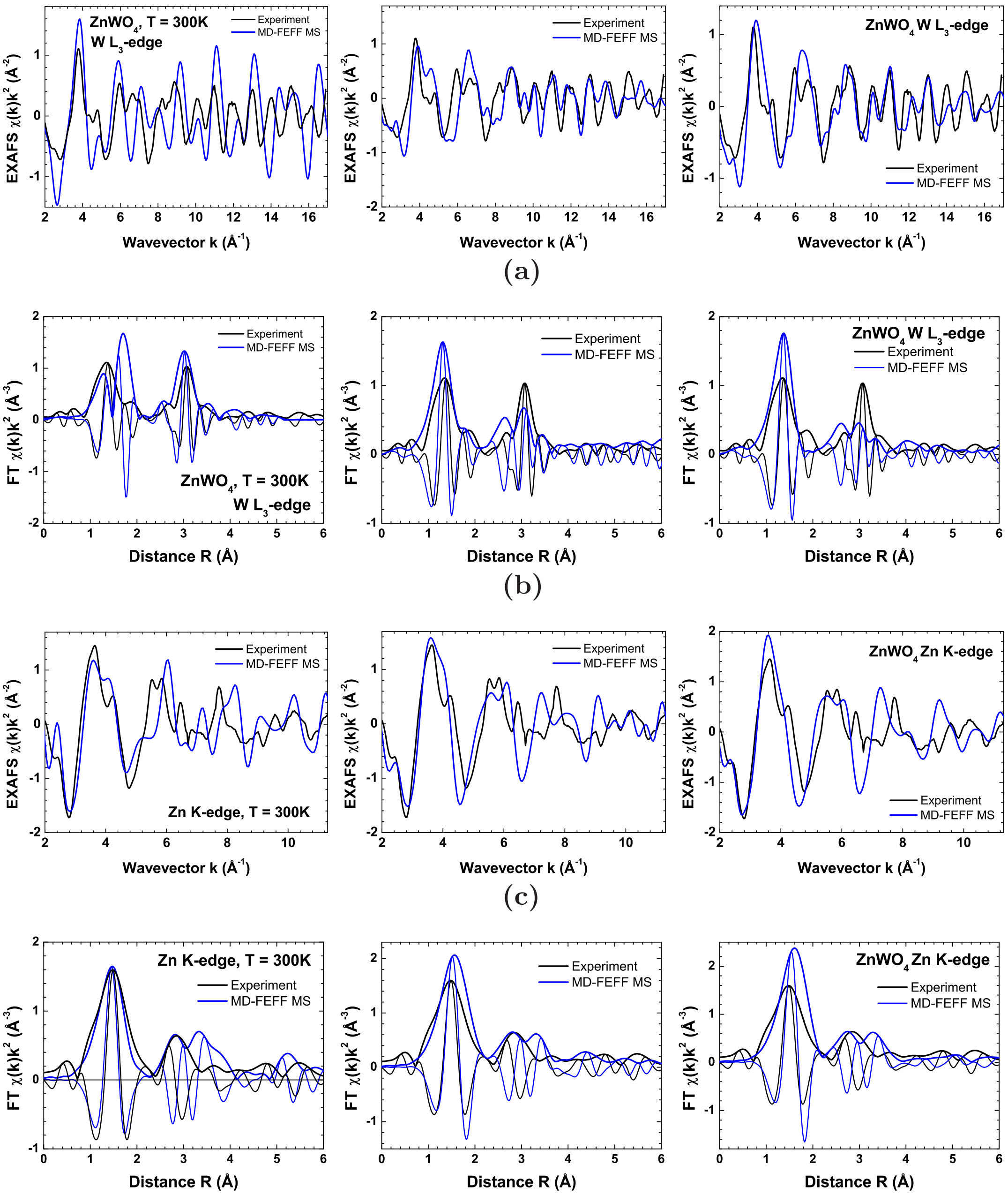

(a)

(b)

(c)

(d)

Figure 5.28: Results of EXAFS modelling using MD-EXAFS method for three models of different complexity (Model1 - left column, Model2 - middle column, Model3 - right column). (a) W L_3-edge EXAFS signal in $ZnWO_4$, (b) FT of the W L_3-edge EXAFS signal in $ZnWO_4$, (c) Zn K-edge EXAFS signal in $ZnWO_4$, (d) FT of the Zn K-edge EXAFS signal in $ZnWO_4$.

in the case of ReO_3 and $CaWO_4$. Therefore, one can conclude that the three developed models do not accurately describe the structure dynamics in $ZnWO_4$. The reason of that is the nature of $[WO_6]$ octahedra distortion, which is caused by the second order Jahn-Teller effect. The formal valence state of tungsten ions in $ZnWO_4$ is 6+, thus resulting in the $5d^0$ electronic configuration. Since the W–O bonding is highly covalent, some amount of electronic charge is back-transferred from the oxygen neighbours to the tungsten $5d$ states causing the removal of degeneracy by symmetry lowering. Such situation cannot be described accurately by simple pair potentials. However, the quantum mechanical approach gives a solution to this problem. In fact, the possibility to model such charge transfer and resulting octahedra distortions has been confirmed by our quantum mechanical LCAO calculations for static $ZnWO_4$ structure.

5.2.3.4 Conclusions

Ab initio calculations of the structural and electronic properties of wolframite-type $ZnWO_4$ crystal have been performed within the periodic LCAO method using hybrid Hartree-Fock–DFT theory. The obtained results are in good agreement with known experimental data. Tungsten-oxygen chemical bonding is found to be highly covalent, whereas zinc-oxygen bonds have more ionic behavior. Calculated density of states is in good agreement with the experimental XPS spectrum from [57]. The main contribution to the valence band is due to the Zn $3d$ states at high binding energies and the O $2p$ and W $5d$ characters at low and medium binding energies.

The calculated phonon frequencies have been compared with the results of infrared and Raman spectroscopies. Rather good accuracy of ab initio phonon frequencies calculations makes them suitable for the prediction of the crystal vibrational properties especially in situations when the experimental approach is difficult or impossible due to selection rules.

Based on the crystal structure of $ZnWO_4$ and known properties, the three force-field (FF) models were constructed and potential parameters were optimized to give good agreement with structural properties, elastic constants and vibrational frequencies. The three FF models give reasonably good matching to the experimental properties. Next the MD simulations were performed for the three FF models, and the configuration averaged EXAFS signals were calculated. However, none of the calculated EXAFS signals gives good matching to the experimental signal. The problem is that the developed

FF models, based on simple pair potentials, cannot accurately describe the distorted structure of $ZnWO_4$, being due to the electronic Jahn-Teller effect. Therefore, more sophisticated simulation methods should be used, like reverse Monte-Carlo or ab initio molecular dynamics.

6

Conclusions

In this thesis the MD-EXAFS method for the EXAFS spectra modelling has been further developed based on the quantum mechanics-classical molecular dynamics (QMMD) approach coupled with ab initio EXAFS spectra calculations. The method expands possibilities in the interpretation of EXAFS spectra by accurate accounting of the thermal disorder within the multiple scattering effects. This allows one to obtain structural information contained beyond the first coordination shell on the many-atom distribution functions. In particular, the angles between chemical bonds and amplitudes of thermal vibrations including correlation effects can be determined.

The capability of the MD-EXAFS method has been demonstrated on an example of EXAFS spectra analysis for three polycrystalline compounds ReO_3, $CaWO_4$ and $ZnWO_4$, having different local coordinations. Besides, an example of the local structure determination in $ZnWO_4$ nanoparticles, based on the conventional EXAFS data analysis, is presented.

Besides the MD simulations, the quantum mechanical LCAO calculations have been also performed for ReO_3, $CaWO_4$ and $ZnWO_4$ crystals. The self consistent procedure was used to find electronic structure and atomic charges. Then optimization of structural parameters was done and further different properties such as bulk modulus, phonon frequencies and phonon dispersion curves were calculated. Thus obtained physical properties were used during the force-field model optimization to increase the number of observables additionally to the experimentally available data.

In the case of $ZnWO_4$ nanoparticles the EXAFS spectra at the Zn K-edge and W L_3-edge were measured and used in the analysis, allowing one to obtain information on the local atomic structure around both absorbing atoms. It was found that strong relaxation of [ZnO_6] and [WO_6] octahedra occurs in nanoparticles comparing to the crystalline $ZnWO_4$. While the interatomic W–O and Zn–O bond lengths show broad distribution already in the crystal, even shorter and longer bond lengths were found in nanoparticles. The possible explanation of this effect is structure relaxation and different distortion of the octahedra within single nanoparticle due to strong influence of the surface. The Raman spectra measurements allowed us to conclude that in nanoparticles short double W–O bonds are formed. This conclusion is based on the Raman frequency dependance from the bond length and correlates well with the appearance of short W–O distances in nanoparticles according to the EXAFS results.

ReO_3, $CaWO_4$ and $ZnWO_4$ have different local coordination around 5*d*-element (W, Re): regular octahedra in ReO_3, regular tetrahedra in $CaWO_4$ and strongly distorted octahedra in $ZnWO_4$. Such difference in the local environment provides a good test of capabilities for the MD-EXAFS method. The structures with regular octahedra (ReO_3) and tetrahedra ($CaWO_4$) can be easily described by a force-field model based on the pair interatomic potentials. However, an additional three body potential is required for tetrahedral case to stabilize tetrahedral coordination during MD simulations. In the case of distorted octahedra ($ZnWO_4$) three force-field models of different complexity were developed which gave reasonable matching between calculated and experimental physical properties. Force-field models for all compounds were further used in molecular dynamics simulations.

The molecular dynamics allows one to introduce thermal atomic motion effects, and the temperature value is one of the simulation parameters. Because of the classical MD method used in the present work, the accurately accessible temperature region is limited to the high temperatures. In the present work, the lowest simulation temperature was set to 300 K for all compounds. In the case of ReO_3 the simulations were performed also at 423 K and 573 K.

As a result of MD simulations, sets of atomic configurations were obtained for each temperature and used to calculate the radial distribution functions, bond angle distributions and atomic movement trajectory determination. To check reliability of the MD simulations, the configuration-averaged EXAFS spectra were calculated and directly compared with the experimental ones.

The configuration-averaged EXAFS spectra for both compounds, ReO_3 and $CaWO_4$, build from regular octahedra and tetrahedra units, respectively, show good agrement with the experimental EXAFS spectra. Also the temperature dependence of the EXAFS spectra for ReO_3 is well reproduced within the single force-field model. Therefore, we conclude that the force-field models describe rather accurately the thermal motion of atoms, including the correlation effects.

However, all developed force-field models for $ZnWO_4$, having distorted [WO_6] and [ZnO_6] octahedra, did not provide good matching with the experimental EXAFS spectra. The reason of that is the nature of [WO_6] octahedra distortion, which is caused by the second order Jahn-Teller effect: tungsten ions in $ZnWO_4$ have 6+ valence state and $5d^0$ electronic configuration, however some amount of electronic charge is back-transferred from the oxygen neighbours to the $5d$ states causing the removal of degeneracy by symmetry lowering. Such situation cannot be described accurately by simple pair potentials. However, the possible solution to this problem can be the use of the quantum molecular dynamics simulations. Such calculations nowadays are very time consuming and are possible mostly for small molecules. For simulation of the EXAFS spectra from crystals, hundreds or thousands atoms are usually required depending on the system, therefore the use of the quantum MD simulations is not practical today. However, the possibility to model such octahedra distortions has been confirmed by our quantum mechanical LCAO calculations for static $ZnWO_4$ structure.

The good agreement between the experimental and simulated EXAFS spectra for ReO_3 and $CaWO_4$ allowed us to make deeper analysis of their structure and atomic motion.

In ReO_3 the atomic motion trajectories show strong anisotropy of oxygen atoms vibrations, which are large perpendicular to the Re–O–Re bonds, thus resulting in a deviation of the Re–O–Re mean angle value from 180° to around 176° at 300 K and 174° at 573 K. The multiple-scattering effect contribution to the EXAFS spectra for the second and further coordination shells was analysed in details. It was found that the MS effects are responsible for about 50% drop of the Re L_3-edge EXAFS signal amplitude in the second coordination shell and about 30% in the third coordination shell.

In $CaWO_4$ the multiple scattering effects are relatively small comparing to ReO_3. The W L_3-edge EXAFS spectrum was decomposed into components from different groups of atoms. The main contribution comes from the nearest oxygens, while more distant atoms produce a signal being five and more times less in amplitude. The peaks in the Fourier transform of the EXAFS spectrum at 2.5 Å and 4.2 Å are due to oxygen atoms. The peak at 3.5 Å is composed of three contributions from O, Ca and W atoms.

In the future, the MD-EXAFS method can be applyied to the materials with symmetrical local structure with the goal to extract additional information on the local dynamical structure from EXAFS spectra. Further improvements of the MD-EXAFS method are possible at the step of the potential parameters optimization by including additional observables as, for example, mean square relative displacements obtained from EXAFS conventional analysis. Moreover, the whole EXAFS spectrum may be used as an observable in the optimization procedure in the future. Another way to improve performance of the MD-EXAFS method is to use ab-initio MD instead of the classical one. This will allow one to deal with the materials having strong local distortions, like $ZnWO_4$, as well as to extend applicability of the method to the low-temperatures region, where quantum effects dominate.

Thesis

1. The combined use of classical molecular dynamics and x-ray absorption spectra calculations from the first principles allow one to make accurate interpretation of the EXAFS spectra for crystalline compounds (ReO_3 and $CaWO_4$) taking into account the many-atoms distribution functions. This approach allows one to access the mean square displacements (EXAFS Debye-Waller factor) of the atom pairs and the bonding angles distributions in outer coordination shells.

2. The vibrations of the oxygen atoms in ReO_3 structure are anisotropic, having the vibration amplitude along the Re–O–Re bonds direction smaller than that perpendicular to the Re–O–Re bonds. It is shown the perpendicular oxygen vibrations lead to that the mean Re–O–Re angle value is less than 180° and shows weak temperature dependence.

3. The contribution from the single-scattering effects is dominating in the W L_3-edge EXAFS spectra of $CaWO_4$. It is shown that oxygen atom group at 2.96 Å and calcium and oxygen groups at 3.79 Å and 4.11 Å, respectively, give the main contribution into the EXAFS signal beyond the first coordination shell.

4. The local atomic structure of $ZnWO_4$ nanoparticles around W and Zn atoms is noticeably deformed comparing to the microcrystalline powder. It is shown that the deformation of the $[WO_6]$ octahedra is related to the formation of the short ($\sim$1.74 Å) double W=O bonds.

References

[1] **http://solartii.com**. xv, 36

[2] **http://www.dep.fmph.uniba.sk**. xv, 34

[3] **http://www.hasylab.de**. xvi, 39

[4] **http://www.theochem.uni-stuttgart.de/pseudopotentials/index.en.html**. 26

[5] F. F. Abraham. **Computational statistical mechanics methodology, applications and supercomputing**. *Adv. Phys.*, **35**(1):1–111, 1986. 27

[6] C. Adamo and V. Barone. **Toward reliable density functional methods without adjustable parameters: The PBE0 model**. *J. Chem. Phys.*, **110**(13):6158–6170, 1999. 75

[7] N. D. Afify and G. Mountjoy. **Molecular-dynamics modeling of Eu^{3+}-ion clustering in SiO_2 glass**. *Phys. Rev. B*, **79**:024202, 2009. 2

[8] N. L. Allan, G. D. Barrera, J. A. Purton, C. E. Sims, and M. B. Taylor. **Ionic solids at elevated temperatures and or high pressures: lattice dynamics, molecular dynamics, Monte Carlo and ab initio studies**. *Phys. Chem. Chem. Phys.*, **2**:1099–1111, 2000. 1

[9] A. L. Ankudinov, C. E. Bouldin, J. J. Rehr, J. Sims, and H. Hung. **Parallel calculation of electron multiple scattering using Lanczos algorithms**. *Phys. Rev. B*, **65**:104107, 2002. 10, 13, 15

[10] A. L. Ankudinov, B. Ravel, J. J. Rehr, and S. D. Conradson. **Real-space multiple-scattering calculation and interpretation of x-ray-absorption near-edge structure**. *Phys. Rev. B*, **58**:7565–7576, 1998. 32, 59, 68, 81

[11] A. Anspoks and A. Kuzmin. **Interpretation of the Ni K-edge EXAFS in nanocrystalline nickel oxide using molecular dynamics simulations**. *J. Non-Cryst. Solids*, **357**(14):2604–2610, 2011. 14

[12] J. D. Axe, Y. Fujii, B. Batlogg, M. Greenblatt, and S. Di Gregorio. **Neutron scattering study of the pressure-induced phase transformation in ReO$_3$**. *Phys. Rev. B*, **31**:663–667, 1985. 54

[13] T. T. Basiev, A. A. Sobol, Yu. K. Voronko, and P. G. Zverev. **Spontaneous Raman spectroscopy of tungstate and molybdate crystals for Raman lasers**. *Opt. Mater.*, **15**(3):205–216, 2000. 43

[14] G. Bunker. **Application of the ratio method of EXAFS analysis to disordered systems**. *Nucl. Instrum. Meth.*, **207**(3):437–444, 1983. 13

[15] D. Cabaret, M. Le Grand, A. Ramos, A. M. Flank, S. Rossano, L. Galoisy, G. Calas, and D. Ghaleb. **Medium range structure of borosilicate glasses from Si K-edge XANES: a combined approach based on multiple scattering and molecular dynamics calculations**. *J. Non-Cryst. Solids*, **289**:1–8, 2001. 14

[16] T. Chatterji, T.C. Hansen, M. Brunelli, and P.F. Henry. **Negative thermal expansion of ReO$_3$ in the extended temperature range**. *Appl. Phys. Lett.*, **94**(24), 2009. 54

[17] T. Chatterji, P. F. Henry, R. Mittal, and S. L. Chaplot. **Negative thermal expansion of ReO$_3$: Neutron diffraction experiments and dynamical lattice calculations**. *Phys. Rev. B*, **78**(13):134105, 2008. 53, 54, 55, 59, 60

[18] M. Chergui. **Picosecond and femtosecond X-ray absorption spectroscopy of molecular systems**. *Acta Crystallogr. A*, **66**(2):229–239, 2010. 2

[19] S. Chernov, L. Grigorjeva, D. Millers, and A. Watterich. **Luminescence spectra and decay kinetics in ZnWO$_4$ and CdWO$_4$ crystals**. *Phys. stat. sol. (b)*, **241**(8):1945–1948, 2004. 44, 47, 48

[20] A. Di Cicco, M. Minicucci, E. Principi, A. Witkowska, J. Rybicki, and R. Laskowski. **Testing interaction models by using x-ray absorption spectroscopy: solid Pb**. *J. Phys.: Condens. Matter*, **14**(12):3365, 2002. 14

[21] T. G. Cooper and N. H. de Leeuw. **A combined ab initio and atomistic simulation study of the surface and interfacial structures and energies of hydrated scheelite: introducing a CaWO$_4$ potential model**. *Surf. Sci.*, **531**(2):159–176, 2003. xviii, xxi, 67, 69, 70, 73

[22] F. Cora, A. Patel, N. M. Harrison, R. Dovesi, and C. R. A. Catlow. **An ab Initio Hartree-Fock Study of the Cubic and Tetragonal Phases of Bulk Tungsten Trioxide**. *J. Am. Chem. Soc.*, **118**(48):12174–12182, 1996. 65, 74, 75

[23] F. Cora, M. G. Stachiotti, C. R. A. Catlow, and C. O. Rodriguez. **Transition Metal Oxide Chemistry: Electronic Structure Study of WO_3, ReO_3, and $NaWO_3$**. *J. Phys. Chem. B*, **101**(20):3945–3952, 1997. 57

[24] F. d'Acapito, S. Mobilio, P. Gastaldo, D. Barbier, L. F. Santos, O. Martins, and R. M. Almeida. **Local order around Er^{3+} ions in SiO_2–TiO_2–Al_2O_3 glassy films studied by EXAFS**. *J. Non-Cryst. Solids*, **293-295**(0):118–124, 2001. 2

[25] G. Dalba, P. Fornasini, A. Kuzmin, J. Purans, and F. Rocca. **X-ray absorption spectroscopy study of ReO_3 lattice dynamics**. *J. Phys.: Condens. Matter*, **7**(6):1199, 1995. 53

[26] F. A. Danevich, S. Henry, H. Kraus, R. McGowan, V. B. Mikhailik, O. G. Shkulkova, and J. Telfer. **Scintillation properties of pure and Ca-doped $ZnWO_4$ crystals**. *Phys. stat. sol. (a)*, **205**(2):335–339, 2008. 47

[27] M. F. Daniel, B. Desbat, J. C. Lassegues, B. Gerand, and M. Figlarz. **Infrared and Raman study of WO_3 tungsten trioxides and WO_3, xH_2O tungsten trioxide tydrates**. *J. Solid State Chem.*, **67**(2):235–247, 1987. 43

[28] M. Dapiaggi and A.N. Fitch. **Negative (and very low) thermal expansion in ReO_3 from 5 to 300 K**. *J. Appl. Crystallogr.*, **42**(2):253–258, 2009. 54

[29] R. Dovesi, V. R. Saunders, R. Roetti, R. Orlando, C. M. Zicovich-Wilson, F. Pascale, B. Civalleri, K. Doll, N. M. Harrison, I. J. Bush, P. DArco, and M. Llunell. **CRYSTAL06 User's Manual**. *University of Torino*, 2006. 25, 26, 55, 65, 74

[30] R. A. Evarestov. *Quantum Chemistry of Solids, The LCAO First Principles Treatment of Crystals*. Springer, 2007. 25, 26

[31] R. A. Evarestov, A. Kalinko, A. Kuzmin, M. Losev, and J. Purans. **FIRST-PRINCIPLES LCAO CALCULATIONS ON 5D TRANSITION METAL OXIDES: ELECTRONIC AND PHONON PROPERTIES**. *Integr. Ferroelectr.*, **108**(1):1–10, 2009. 65, 76

[32] G. Ferlat, A. San Miguel, J. F. Jal, J. C. Soetens, Ph. A. Bopp, I. Daniel, S. Guillot, J. L. Hazemann, and R. Argoud. **Hydration of the bromine ion in a supercritical 1:1 aqueous electrolyte**. *Phys. Rev. B*, **63**:134202, 2001. 2

[33] A. Filipponi. **EXAFS for liquids**. *J. Phys.: Condens. Matter*, **13**(7):R23, 2001. 2, 12

[34] A. Filipponi and A. Di Cicco. **X-ray-absorption spectroscopy and n -body distribution functions in condensed matter. II. Data analysis and applications**. *Phys. Rev. B*, **52**:15135–15149, 1995. 3, 15

[35] A. Filipponi, A. Di Cicco, and C. R. Natoli. **X-ray-absorption spectroscopy and n-body distribution functions in condensed matter. I. Theory**. *Phys. Rev. B*, **52**:15122–15134, 1995. 3, 10, 15

[36] P. Fornasini. **Study of lattice dynamics via extended x-ray absorption fine structure**. *J. Phys.: Condens. Matter*, **13**(34):7859, 2001. 30

[37] P. Fornasini, F. Monti, and A. Sanson. **On the cumulant analysis of EXAFS in crystalline solids**. *J. Synchrotron Radiat.*, **8**(6):1214–1220, 2001. 11, 13

[38] V. Fritzsche. **Application of curved-wavefront approximations to multiple-scattering effects in EXAFS of ReO_3**. *J. Phys.: Condens. Matter*, **1**(41):7715, 1989. 53

[39] B. Fultz, T. Kelley, J. D. Lee, M. Aivazis, O. Delaire, and D. Abernathy. *Experimental Inelastic Neutron Scattering*. Springer-Verlag, 2004. 21

[40] J. D. Gale. **Empirical potential derivation for ionic materials**. *Philos. Mag. B*, **73**(1):3–19, 1996. 59, 68, 81

[41] J. D. Gale and A. L. Rohl. **The General Utility Lattice Program (GULP)**. *Mol. Simulat.*, **29**(5):291–341, 2003. 23, 28, 59, 68, 81

[42] G. Gouadec and P. Colomban. **Raman Spectroscopy of nanomaterials: How spectra relate to disorder, particle size and mechanical properties**. *Prog. Cryst. Growth Ch.*, **53**(1):1–56, 2007. 41, 58

[43] L. Gracia, V. M. Longo, L. S. Cavalcante, A. Beltran, W. Avansi, M. S. Li, V. R. Mastelaro, J. A. Varela, E. Longo, and J. Andres. **Presence of excited electronic state in $CaWO_4$ crystals provoked by a tetrahedral distortion: An experimental and theoretical investigation**. *J. Appl. Phys.*, **110**(4):043501, 2011. 63

[44] J. D. Grunwaldt, C. Keresszegi, T. Mallat, and A. Baiker. **In situ EXAFS study of Pd/Al_2O_3 during aerobic oxidation of cinnamyl alcohol in an organic solvent**. *J. Catal.*, **213**(2):291–295, 2003. 2

[45] T. Guo. **More power to X-rays: New developments in X-ray spectroscopy**. *Laser Photonics Rev.*, **3**(6):591–622, 2009. 2

[46] E. Gurmen, E. Daniels, and J. S. King. **Crystal Structure Refinement of $SrMoO_4$, $SrWO_4$, $CaMoO_4$, and $BaWO_4$ by Neutron Diffraction**. *J. Chem. Phys.*, **55**(3):1093–1097, 1971. 63

[47] P. J. Hay and W. R. Wadt. **Ab initio effective core potentials for molecular calculations. Potentials for K to Au including the outermost core orbitals**. *J. Chem. Phys.*, **82**(1):299–310, 1985. 65, 74

[48] P. J. Hay and W. R. Wadt. **Ab initio effective core potentials for molecular calculations. Potentials for main group elements Na to Bi**. *J. Chem. Phys.*, **82**(1):284–298, 1985. 74

[49] P. J. Hay and W. R. Wadt. **Ab initio effective core potentials for molecular calculations. Potentials for the transition metal atoms Sc to Hg**. *J. Chem. Phys.*, **82**(1):270–283, 1985. 74

[50] R. M. Hazen, L. W. Finger, and J. W. E. Mariathasan. **High-pressure crystal chemistry of scheelite-type tungstates and molybdates**. *J. Phys. Chem. Solids*, **46**(2):253–263, 1985. 65

[51] H. Y. He. **Preparation and luminescence property of Sm-doped $ZnWO_4$ powders and films with wet chemical methods**. *Phys. stat. sol. (b)*, **246**(1):177–182, 2009. 47

[52] P. Hohenberg and W. Kohn. **Inhomogeneous Electron Gas**. *Phys. Rev.*, **136**:B864–B871, 1964. 24

[53] B. Houser and R. Ingalls. **X-ray-absorption fine structure determination of pressure-induced bond-angle changes in ReO_3**. *Phys. Rev. B*, **61**(10):6515–6520, 2000. 53, 60

[54] G. Huang and Y. Zhu. **Synthesis and photocatalytic performance of $ZnWO_4$ catalyst**. *Mater. Sci. Eng. B*, **139**:201–208, 2007. 33

[55] M. M. Hurley, L. F. Pacios, P. A. Christiansen, R. B. Ross, and W. C. Ermler. **Ab initio relativistic effective potentials with spin-orbit operators. II. K through Kr**. *J. Chem. Phys.*, **84**(12):6840–6853, 1986. 74

[56] M. Ishii, T. Tanaka, T. Akahane, and N. Tsuda. **Infrared Transmission Spectra of Metallic ReO_3**. *J. Phys. Soc. Jpn.*, **41**:908–912, 1976. 54

[57] M. Itoh, N. Fujita, and Y. Inabe. **X-Ray Photoelectron Spectroscopy and Electronic Structures of Scheelite- and Wolframite-Type Tungstate Crystals**. *J. Phys. Soc. Jpn.*, **75**(8), 2006. xix, 75, 77, 78, 84

[58] M. Itoh, T. Katagiri, T. Aoki, and M. Fujita. **Photo-stimulated luminescence and photo-induced infrared absorption in $ZnWO_4$**. *Radiat. Meas.*, **42**:545–548, 2007. 44, 47

[59] F. Jalilehvand, D. Spangberg, P. Lindqvist-Reis, K. Hermansson, I. Persson, and M. Sandstrm. **Hydration of the Calcium Ion. An EXAFS, Large-Angle X-ray Scattering, and Molecular Dynamics Simulation Study**. *J. Am. Chem. Soc.*, **123**(3):431–441, 2001. 14

[60] R. Jia, Q. Wu, G. Zhang, and Y. Ding. **Preparation, structural and optical properties of ZnWO$_4$ and CdWO$_4$ nanofilms**. *J. Mater. Sci.*, **42**:4887–4891, 2007. 47

[61] A. Kalinko, A. Kotlov, A. Kuzmin, V. Pankratov, A. Popov, and L. Shirmane. **Electronic excitations in ZnWO$_4$ and Zn$_x$Ni$_{1-x}$WO$_4$ (x = 0.1 0.9) using VUV synchrotron radiation**. *Cent. Eur. J. Phys.*, **9**:432–437, 2011. 47

[62] A. Kalinko and A. Kuzmin. **Raman and photoluminescence spectroscopy of zinc tungstate powders**. *J. Lumin.*, **129**(10):1144–1147, 2009. 33, 41, 47

[63] A. Kalinko, A. Kuzmin, and R. A. Evarestov. **Ab initio study of the electronic and atomic structure of the wolframite-type ZnWO$_4$**. *Solid State Commun.*, **149**:425–428, 2009. 55, 75

[64] P. Kidkhunthod and A. C. Barnes. **A structural study of praseodymium gallate glasses by combined neutron diffraction, molecular dynamics and EXAFS techniques**. *J. Phys.: Conf. Series*, **190**(1):012076, 2009. 14

[65] W. Kohn. **Nobel Lecture: Electronic structure of matter wave functions and density functionals**. *Rev. Mod. Phys.*, **71**:1253–1266, 1999. 24

[66] W. Kohn and L. J. Sham. **Self-Consistent Equations Including Exchange and Correlation Effects**. *Phys. Rev.*, **140**:A1133–A1138, 1965. 24

[67] V. N. Kolobanov, I. A. Kamenskikh, V. V. Mikhailin, I. N. Shpinkov, D. A. Spassky, B. I. Zadneprovsky, L. I. Potkin, and G. Zimmerer. **Optical and luminescent properties of anisotropic tungstate crystals**. *Nucl. Instrum. Meth. A*, **486**:496–503, 2002. 44, 47, 75

[68] H. Kraus, V. B. Mikhailik, L. Vasylechko, D. Day, K. B. Hutton, J. Telfer, and Yu. Prots. **Effect of Ca doping on the structure and scintillation properties of ZnWO$_4$**. *Phys. stat. sol. (a)*, **204**(3):730–736, 2007. 41, 47, 49, 52

[69] K. Kunc and R. M. Martin. **Ab Initio Force Constants of GaAs: A New Approach to Calculation of Phonons and Dielectric Properties**. *Phys. Rev. Lett.*, **48**(6):406–409, 1982. 26

[70] A. Kuzmin. **EDA: EXAFS data analysis software package**. *Physica B: Condens. Matter*, **208-209**:175–176, 1995. 48

[71] A. Kuzmin, G. Dalba, P. Fornasini, F. Rocca, and O. Sipr. **X-ray absorption spectroscopy of strongly disordered glasses: Local structure around Ag ions in g-Ag$_2$O·nB$_2$O$_3$**. *Phys. Rev. B*, **73**:174110, 2006. 2

[72] A. Kuzmin, V. Efimov, E. Efimova, V. Sikolenko, S. Pascarelli, and I.O. Troyanchuk. **Interpretation of the Co K-edge EXAFS in $LaCoO_3$ using molecular dynamics simulations**. *Solid State Ionics*, **188**(1):21–24, 2011. 14

[73] A. Kuzmin and R. A. Evarestov. **Quantum mechanics-classical molecular dynamics approach to EXAFS**. *J. Phys.: Conf. Series*, **190**(1):012024, 2009. 14, 20

[74] A. Kuzmin and R. A. Evarestov. **Quantum mechanicsmolecular dynamics approach to the interpretation of x-ray absorption spectra**. *J. Phys.: Condens. Matter*, **21**(5):055401, 2009. 14, 20, 22

[75] A. Kuzmin, R. Kalendarev, A. Kursitis, and J. Purans. **Confocal spectromicroscopy of micro and nano-structured materials**. *Latvian J. Phys. Technol. Sci.*, **2**:66, 2006. 5, 36, 60

[76] A. Kuzmin, R. Kalendarev, J. Purans, J. P Itie, F. Baudelet, A. Congeduti, and P. Munsch. **EXAFS study of pressure-induced phase transition in $SrWO_4$**. *Phys. Scripta*, **2005**:556, 2005. 2

[77] A. Kuzmin and P. Parent. **Focusing and superfocusing effects in X-ray absorption fine structure at the iron K edge in FeF_3**. *J. Phys.: Condens. Matter*, **6**(23):4395, 1994. 19

[78] A. Kuzmin and J. Purans. **Dehydration of the molybdenum trioxide hydrates MoO_3 nH_2O: in situ x-ray absorption spectroscopy study at the Mo K edge**. *J. Phys.: Condens. Matter*, **12**(9):1959, 2000. 11, 49

[79] A. Kuzmin and J. Purans. **Local atomic and electronic structure of tungsten ions in AWO_4 crystals of scheelite and wolframite types**. *Radiat. Meas.*, **33**(5):583–586, 2001. 63

[80] A. Kuzmin, J. Purans, M. Benfatto, and C. R. Natoli. **X-ray-absorption study of rhenium L_3 and L_1 edges in ReO_3: Multiple-scattering approach**. *Phys. Rev. B*, **47**(5):2480–2486, 1993. 53, 62

[81] A. Kuzmin, J. Purans, E. Cazzanelli, C. Vinegoni, and G. Mariotto. **X-ray diffraction, extended x-ray absorption fine structure and Raman spectroscopy studies of WO_3 powders and (1 - x)$WO_3 - y$xReO_2 mixtures**. *J. Appl. Phys.*, **84**(10):5515–5524, 1998. 44

[82] A. Kuzmin, J. Purans, G. Dalba, P. Fornasini, and F. Rocca. **A high-temperature x-ray absorption spectroscopy study of ReO_3**. *J. Phys.: Condens. Matter*, **8**(46):9083, 1996. 53

[83] R. Laskowski, J. Rybicki, M. Chybicki, and A. Di Cicco. **Pair Potential for Solid Rhodium from Extrapolated Ab-Initio Data**. *Phys. stat. sol. (b)*, **217**(2):737–746, 2000. 14

[84] Y. Liu, H. Wang, G. Chen, Y. D. Zhou, B. Y. Gu, and B. Q. Hu. **Analysis of Raman spectra of $ZnWO_4$ single crystals**. *J. Appl. Phys.*, **64**(9):4651–4653, 1988. 43

[85] Z. Lou, J. Hao, and M. Cocivera. **Luminescence of $ZnWO_4$ and $CdWO_4$ thin films prepared by spray pyrolysis**. *J. Lumin.*, **99**(4):349–354, 2002. 44, 47

[86] H. Matsuura, S. Watanabe, H. Akatsuka, Y. Okamoto, and A. K. Adya. **XAFS analyses of molten metal fluorides**. *J. Fluorine Chem.*, **130**(1):53–60, 2009. 14

[87] P. J. Merkling, A. Munoz-Paez, J. M. Martinez, R. R. Pappalardo, and E. Sanchez Marcos. **Molecular-dynamics-based investigation of scattering path contributions to the EXAFS spectrum: The Cr^{3+} aqueous solution case**. *Phys. Rev. B*, **64**:012201, 2001. 14

[88] B. Mierzwa. **EXAFS studies of bimetallic palladiumcobalt nanoclusters using Molecular Dynamics simulations**. *J. Alloy Compd.*, **401**:127–134, 2005. 14

[89] V. B. Mikhailik, H. Kraus, D. Wahl, M. Itoh, M. Koike, and I. K. Bailiff. **One- and two-photon excited luminescence and band-gap assignment in $CaWO_4$**. *Phys. Rev. B*, **69**(20):205110, 2004. 47, 63, 65

[90] H. J. Monkhorst and J. D. Pack. **Special points for Brillouin-zone integrations**. *Phys. Rev. B*, **13**(12):5188–5192, 1976. 75

[91] S.M. Montemayor and A. F. Fuentes. **Electrochemical characteristics of lithium insertion in several 3D metal tungstates (MWO_4, M=Mn, Co, Ni and Cu) prepared by aqueous reactions**. *Ceram. Int.*, **30**(3):393–400, 2004. 47

[92] G. Mountjoy. **Molecular dynamics, diffraction and EXAFS of rare earth phosphate glasses compared with predictions based on bond valence**. *J. Non-Cryst. Solids*, **353**:2029–2034, 2007. 14

[93] R. S. Mulliken. **Electronic Population Analysis on LCAO–MO Molecular Wave Functions. I**. *J. Chem. Phys.*, **23**(10):1833–1840, 1955. 26

[94] F. D. Murnaghan. **The Compressibility of Media under Extreme Pressures**. *Proc. Natl. Acad. Sci. USA*, **30**(9):244–247, 1944. 26

[95] V. Nagirnyi, E. Feldbach, L. Jonsson, M. Kirm, A. Kotlov, A. Lushchik, V. A. Nefedov, and B. I. Zadneprovski. **Energy transfer in $ZnWO_4$ and $CdWO_4$ scintillators**. *Nucl. Instrum. Meth. A*, **486**:395–398, 2002. 44, 47

[96] M. A. Newton, A. J. Dent, and J. Evans. **Bringing time resolution to EXAFS: recent developments and application to chemical systems**. *Chem. Soc. Rev.*, **31**:83–95, 2002. 2

[97] Y. Okamoto. **XAFS simulation of highly disordered materials**. *Nucl. Instrum. Meth. A*, **526**(3):572–583, 2004. 14

[98] E. Orhan, M. Anicete-Santos, M. A.M.A Maurera, F. M. Pontes, A. G. Souza, J. Andres, A. Beltran, J. A. Varela, P. S Pizani, C. A. Taft, and E. Longo. **Towards an insight on the photoluminescence of disordered $CaWO_4$ from a joint experimental and theoretical analysis**. *J. Solid State Chem.*, **178**(4):1284–1291, 2005. 65

[99] A. E. Ovechkin, V. D. Ryzhikov, G. Tamulaitis, and A. Zukauskas. **Luminescence of $ZnWO_4$ and $CdWO_4$ Crystals**. *Phys. stat. sol. (a)*, **103**(1):285–290, 1987. 44, 47

[100] K. Parlinski, Z. Q. Li, and Y. Kawazoe. **First-Principles Determination of the Soft Mode in Cubic ZrO_2**. *Phys. Rev. Lett.*, **78**:4063–4066, 1997. 26, 27, 55, 66, 78

[101] P. F. Peterson, Th. Proffen, I. K. Jeong, S. J. L. Billinge, K. S. Choi, M. G. Kanatzidis, and P. G. Radaelli. **Local atomic strain in $ZnSe_{1-x}Te_x$ from high real-space resolution neutron pair distribution function measurements**. *Phys. Rev. B*, **63**:165211, 2001. 2

[102] Yu. V. Pisarevskii, I. M. Silvestrova, R. Voszka, . Peter, I. Foldvri, and J. Janszky. **Elastic and acoustic properties of $ZnWO_4$ single crystal**. *Phys. stat. sol. (a)*, **107**(1):161–164, 1988. 76

[103] S. Piskunov, E. Heifets, R. I. Eglitis, and G. Borstel. **Bulk properties and electronic structure of $SrTiO_3$, $BaTiO_3$, $PbTiO_3$ perovskites: an ab initio HF/DFT study**. *Comp. Mater. Sci.*, **29**(2):165–178, 2004. 65, 75

[104] S. P. S. Porto and J. F. Scott. **Raman Spectra of $CaWO_4$, $SrWO_4$, $CaMoO_4$, and $SrMoO_4$**. *Phys. Rev.*, **157**:716–719, 1967. 66

[105] J. Purans, G. Dalba, P. Fornasini, A. Kuzmin, S. De Panfilis, and F. Rocca. **EXAFS and XRD Studies with Subpicometer Accuracy: The Case of ReO_3**. *AIP Conference Proceedings*, **882**(1):422–424, 2007. 37, 53, 60

[106] J. Purans, A. Kuzmin, E. Cazzanelli, and G. Mariotto. **Disorder-induced Raman scattering in rhenium trioxide (ReO_3)**. *J. Phys.: Condens. Matter*, **19**(22):226206, 2007. xviii, 58

[107] J. Purans, J. Timoshenko, A. Kuzmin, G. Dalba, P. Fornasini, R. Grisenti, N. D. Afify, F. Rocca, S. De Panfilis, I. Ozhogin, and S. I. Tiutiunnikov. **Femtometer accuracy EXAFS measurements: Isotopic effect in the first, second and third coordination shells of germanium**. *J. Phys.: Conf. Series*, **190**(1):012063, 2009. 3

[108] J. J. Rehr and R. C. Albers. **Theoretical approaches to x-ray absorption fine structure**. *Rev. Mod. Phys.*, **72**(3):621–654, 2000. 2, 3, 9, 32, 49

[109] H. M. Rietveld. **A profile refinement method for nuclear and magnetic structures**. *J. Appl. Crystallogr.*, **2**(2):65–71, 1969. 1

[110] O. M. Roscioni, N. Zonias, S. W. T. Price, An. E. Russell, T. Comaschi, and C. K. Skylaris. **Computational prediction of L_3 EXAFS spectra of gold nanoparticles from classical molecular dynamics simulations**. *Phys. Rev. B*, **83**(11):115409, 2011. 14

[111] S. Rossano, A. Ramos, J.-M. Delaye, S. Creux, A. Filipponi, Ch. Brouder, and G. Calas. **EXAFS and Molecular Dynamics combined study of CaO–FeO–$2SiO_2$ glass. New insight into site significance in silicate glasses**. *Europhys. Lett.*, **49**(5):597, 2000. 14

[112] A. Sanson. **Local dynamical properties of crystalline germanium and their effects in extended x-ray absorption fine structure**. *Phys. Rev. B*, **81**:012304, 2010. 14

[113] P. F. Schofield, J. M. Charnock, G. Cressey, and C. M. B. Henderson. **An EXAFS study of cation site distortions through the P2/c-P1 phase transition in the synthetic cuproscheelite-sanmartinite solid solution**. *Mineral Mag*, **58**(2):185–199, 1994. 74

[114] P. F. Schofield, K. S. Knight, and G. Cressey. **Neutron powder diffraction study of the scintillator material $ZnWO_4$**. *J. Mater. Sci.*, **31**(11):2873–2877, 1996. 41, 49, 52

[115] A. Senyshyn, M. Hoelzel, T. Hansen, L. Vasylechko, V. Mikhailik, H. Kraus, and H. Ehrenberg. **Thermal structural properties of calcium tungstate**. *J. Appl. Crystallogr.*, **44**:319–326, 2011. 63

[116] A. Senyshyn, H. Kraus, V. B. Mikhailik, and V. Yakovyna. **Lattice dynamics and thermal properties of $CaWO_4$**. *Phys. Rev. B*, **70**(21):214306, 2004. xviii, xxi, 67, 69, 70, 73

[117] Z. Shao, Q. Zhang, T. Liu, and J. Chen. **Computer study of intrinsic defects in $CaWO_4$**. *Nucl. Instrum. Meth. B*, **266**(5):797–801, 2008. 67

[118] R. Spezia, M. Duvail, P. Vitorge, T. Cartailler, J. Tortajada, G. Chillemi, P. DAngelo, and M. P. Gaigeot. **A Coupled Car-Parrinello Molecular Dynamics and EXAFS Data Analysis Investigation of Aqueous Co^{2+}**. *J. Phys. Chem. A*, **110**(48):13081–13088, 2006. 14

[119] R. Spezia, M. Duvail, P. Vitorge, and P. D'Angelo. **Molecular dynamics to rationalize EXAFS experiments: A dynamical model explaining hydration behaviour across the lanthanoid(III) series**. *J. Phys.: Conf. Series*, **190**(1):012056, 2009. 14

[120] J. Timoshenko, A. Kuzmin, and J. Purans. **Molecular dynamics simulations of EXAFS in germanium**. *Cent. Eur. J. Phys.*, **9**:710–715, 2011. 14

[121] A. Togo, F. Oba, and I. Tanaka. **First-principles calculations of the ferroelastic transition between rutile-type and $CaCl_2$ -type SiO_2 at high pressures**. *Phys. Rev. B*, **78**(13):134106, 2008. 55

[122] D. M. Trots, A. Senyshyn, L. Vasylechko, R. Niewa, T. Vad, V. B. Mikhailik, and H. Kraus. **Crystal structure of $ZnWO_4$ scintillator material in the range of 3–1423 K**. *J. Phys.: Condens. Matter*, **21**(32):325402, 2009. 41, 49, 52, 73, 76

[123] N. Tsuda, Y. Sumino, I. Ohno, and T. Akahane. **Elastic Constants of ReO_3**. *J. Phys. Soc. Jpn.*, **41**(4):1153–1158, 1976. 54, 57, 59

[124] M. Vaccari and P. Fornasini. **Einstein and Debye models for EXAFS parallel and perpendicular mean-square relative displacements**. *J. Synchrotron Radiat.*, **13**(4):321–325, 2006. 30

[125] R. V. Vedrinskii, L. A. Bugaev, and I. G. Levin. **Single and Multiple Electron Scattering Description in X-Ray Absorption Spectrum Theory and the Problem of Solid Structure Investigation**. *Phys. stat. sol. (b)*, **150**(1):307–314, 1988. 53

[126] Yu. K. Voronko and A. A. Sobol. **Influence of cations on the vibrational spectra and structure of $[WO_4]$ complexes in molten tungstates**. *Inorg. Mater.*, **41**(4):420–428, 2005. 43

[127] H. Wang, F. D. Medina, Y. D. Zhou, and Q. N. Zhang. **Temperature dependence of the polarized Raman spectra of $ZnWO_4$ single crystals**. *Phys. Rev. B*, **45**(18):10356, 1992. 43

[128] Z. L. Wang, H. L. Li, and J. H. Hao. **Blue-Green, Red, and White Light Emission of $ZnWO_4$-based Phosphors for Low-Voltage Cathodoluminescence Applications**. *J. Electrochem. Soc.*, **155**(6):J152–J156, 2008. 47

[129] A. Witkowska, J. Rybicki, and A. Di Cicco. **Structure of partially reduced bismuthsilicate glasses: EXAFS and MD study**. *J. Alloy Compd.*, **401**:135–144, 2005. 14

[130] A. Witkowska, J. Rybicki, and A. Di Cicco. **Structure of partially reduced xPbO (1–x)SiO$_2$ glasses: combined EXAFS and MD study**. *J. Non-Cryst. Solids*, **351**(5):380–393, 2005. 14

[131] A. Witkowska, J. Rybicki, S. De Panfilis, and A. Di Cicco. **The structure of liquid lead: EXAFS and MD studies**. *J. Non-Cryst. Solids*, **352**:4351–4355, 2006. 14

[132] K. Yagi, S. Umezawa, H. Terauchi, and H. Kasatani. **EXAFS study of phase transitions in KIO$_3$**. *J. Synchrotron Radiat.*, **8**(2):803–805, 2001. 2

[133] Y. Zhang, N. A. W. Holzwarth, and R. T. Williams. **Electronic band structures of the scheelite materials CaMoO$_4$, CaWO$_4$, PbMoO$_4$, and PbWO$_4$**. *Phys. Rev. B*, **57**:12738–12750, 1998. 65

Author's publication list

1. A. Kalinko, A. Kuzmin, R.A. Evarestov, **Ab initio study of the electronic and atomic structure of the wolframite-type ZnWO$_4$**, Solid State Commun. 149 (2009) 425-428.
2. A. Kalinko, A. Kuzmin, **Raman and photoluminescence spectroscopy of zinc tungstate powders**, J. Lumin. 129 (2009) 1144-1147.
3. R. A. Evarestov, A. Kalinko, A. Kuzmin, M. Losev, J. Purans, **First-principles LCAO calculations on 5d transition metal oxides: electronic and phonon properties**, Integr. Ferroelectrics 108 (2009) 1-10.
4. A. Kalinko, R. A. Evarestov, A. Kuzmin, J. Purans, **Interpretation of EXAFS in ReO$_3$ using molecular dynamics simulations,** J. Phys.: Conf. Ser. 190 (2009) 012080.
5. A. Kalinko, A. Kuzmin, **Static and dynamic structure of ZnWO$_4$ nanoparticles**, J. Non-Cryst. Solids 357 (2011) 2595-2599.
6. A. Kalinko, A. Kotlov, A. Kuzmin, V. Pankratov, A.I. Popov, L. Shirmane, **Electronic excitations in ZnWO$_4$ and Zn$_x$Ni$_{1-x}$WO$_4$ (x=0.1-0.9) using VUV synchrotron radiation**, Cent. Eur. J. Phys. 9 (2011) 432-437.
7. A. Kuzmin, A. Kalinko, R.A. Evarestov, **First-principles LCAO study of phonons in NiWO$_4$**, Cent. Eur. J. Phys. 9 (2011) 502-509.

Participation in conferences

1. A. Kalinko, A. Kuzmin, **Raman and photoluminescence spectroscopy of zinc tungstate powders**, International Baltic Sea Region Conference 'Functional Materials and Nanotechnologies' (FM&NT), 2008, Riga, Latvia
2. A. Kalinko, A. Kuzmin, R.A. Evarestov **Ab initio study of the electronic and atomic structure of the wolframite-type $ZnWO_4$**, International Baltic Sea Region Conference 'Functional Materials and Nanotechnologies' (FM&NT), 2008, Riga, Latvia
3. A. Kalinko, A. Kuzmin, R.A. Evarestov **Electronic structure calculations of $ZnWO_4$: periodic and nanocluster models**, 6th International Conference on Advanced Optical Materials and Devices (AOMD-6), 2008, Riga, Latvia
4. A. Kalinko, A. Kuzmin, **Molecular dynamics simulations of ReO_3** ISSP 25th Scientific Conference, 2009, Riga, Latvia
5. A. Kalinko, R.A. Evarestov, A. Kuzmin, M. Losev, J. Purans, **Structural, Electronic and Phonon Properties of Metallic ReO_3**, International Baltic Sea Region Conference 'Functional Materials and Nanotechnologies' (FM&NT), 2009, Riga, Latvia
6. A. Kalinko, A. Kuzmin, R.A. Evarestov **First Principles LCAO Calculations of Tungstates $MeWO_4$ (Me = Ca, Mg, Zn)**, International Baltic Sea Region Conference 'Functional Materials and Nanotechnologies' (FM&NT), 2009, Riga, Latvia

7. A. Kalinko, R.A. Evarestov, A. Kuzmin, J. Purans, **Interpretation of EXAFS From ReO_3 Using Molecular Dynamics Simulations**, 14th International Conference on X-ray Absorption Fine Structure (XAFS14), 2009, Camerino, Italy
8. A. Kalinko, A. Kuzmin, **Determining crystal structure and atomic positions using EXAFS** ISSP 26th Scientific Conference, 2010, Riga, Latvia
9. A. Kalinko, J. Timoshenko, A. Kuzmin, **EXAFS study of $ZnWO_4$ on the W L_3 and Zn K edges**, International Baltic Sea Region Conference 'Functional Materials and Nanotechnologies' (FM&NT), 2010, Riga, Latvia
10. A. Kalinko, A. Kuzmin, **Static and Dynamic Structure of $ZnWO_4$ Nanoparticles**, 11th International Conference on the Structure of Non-Crystalline Materials (NCM11), 2010, Paris, France
11. A. Kalinko, A. Kuzmin, **Crystal Structure Determination Using EXAFS Total Scattering Phase**, International Baltic Sea Region Conference 'Functional Materials and Nanotechnologies' (FM&NT), 2011, Riga, Latvia

Participation in schools with posters

1. A. Kalinko, A. Kuzmin, R.A. Evarestov, **Electronic and Atomic Structure Study of ZnWO$_4$**, Nordic and European Summer School "VUV and X-ray Research for the Future using FEL's and Ultra Brilliant Sources", May 26 - June 2, 2008, Odengarden and MAX-lab, Sweden

2. A. Kalinko, A. Kuzmin, R.A. Evarestov, **Molecular Dynamics Approach to Calculation of EXAFS Spectra**, CCP5 Methods in Molecular Simulation Summer School, July 06-15, 2008, Shefield, UK

3. A. Kalinko, A. Kuzmin, **Zinc Tungstate Powders Investigation by Spectroscopic Methods**, 7th PSI Summer School on Condensed Matter Research, August 15-23, 2008, Zuoz, Switzerland

4. A. Kalinko, A. Kuzmin, **Interpretation of x-ray absorption spectra using molecular dynamics simulations**, Higher European Research Course for Users of Large Experimental Systems (HERCULES 2011), February 27 - March 31, 2011, Grenoble and Paris, France